UNIVERSITY OF CALIFORNIA,
IRVINE

SERS from the point of view of the Molecule & the Antenna

DISSERTATION

submitted in partial satisfaction of the requirements
for the degree of

Doctor of Philosophy

in Chemical and Material Physics

by

Mayukh Banik

Thesis Committee:
Professor V. Ara Apkarian, Chair
Associate Professor Eric Potma
Assistant Professor Matt Law

2014

DEDICATION

To

my parents, who missed me so much when I was busy working.

I want movement and not a calm course of existence. I want excitement and danger and the chance to sacrifice myself for my love. I feel in myself a superabundance of energy which finds no outlet in the quiet life.
- Leo Tolstoy

Best is the worst enemy of good, so think twice if you want to be a perfectionist.
- Nemo the Nomad

TABLE OF CONTENTS

List of Figures

Figure 2.4: AFM images of the dumbbell before and after recording the SERS sequence. The resolution is sufficient to identify the isolated dumbbell and its principle axis for the purpose of aligning the polarization of the incident field. As the junction fuses during the measured sequence, the effective inter-sphere distance becomes negative.....50

Figure 2.5: A) Image plot of a sequence of 36 SERS spectra recorded consecutively, during the fusion of the dumbbell. The white squares highlight: i) The 50-fold fluctuation in overall intensity of the normal SERS line-spectrum, ascribed to tuning across the BDP resonance by the closing junction, ii) The development of band-spectra and a dramatic increase in integrated intensity, assigned to the transition to the conductivity limit where current passing though the molecule leads to Stark shifting and broadening. c) The CO spectral region, which shows evolution that parallels but trails that of DBDT. B) Selected spectra from the image plot: #5 – SERS line-spectrum of DBDT and CO; #8 – onset of band-spectrum at the DBDT site while the normal SERS of CO is observed; #15 and #17 – the dominance of band-spectra at both sites, #27 – re-emergence of lines at the DBDT site, while CO remains in the CTP regime, #36 – the normal SERS line-spectrum of DBDT, the molecule is now outside the conductivity range of the spheres and appears unscathed by the fusion process. C) Decomposition of the CO spectrum into the normal SERS line at 2115 cm^{-1} and the broad CTPR band with evolving band center. D) The sequential spectral shift of the CO charge transfer resonance (bottom abscissa), and the associated Stark field (top abscissa). The shift reaches a limiting value of ~100 cm^{-1}, which corresponds to 1 V/Å. E) The intensity of the normal CO SERS line (blue) and the CTPR band

List of Tables

ACKNOWLEDGMENTS

I would like to express the deepest appreciation to my committee chair and thesis advisor, Professor V. A. Apkarian, who is the most logical and insightful person I came across during my educational venture. I have always felt that it is not the height of achievement that I long for, rather, enjoying every moment of the journey is what keeps me going. And as a mentor, friendly guidance provided by Professor Apkarian totally made every bit of my grad school experience worth living. I feel proud that I got a chance to work with him. I sincerely admire the chest of knowledge and wisdom he unlocked in front of me which helped me develop as a mature individual, both academically and personally.

I would like to thank my committee members, Professor Eric Potma and Professor Matt Law for helping me out periodically with scientific discussions over the past years.

In addition, I would like to thank all my colleagues and co-workers whom I have been shared the science with.

ABSTRACT OF THE THESIS

SERS from the point of view of the Molecule & the Antenna

By

Mayukh Banik

Doctor of Philosophy

in Chemical and Material Physics

University of California, Irvine, 2014

Professor V. Ara Apkarian, Chair

Surface Enhanced Raman Spectra (SERS) recorded on plasmonic substrate is often accompanied with broad background, origin of which is extensively deliberated. Moreover, fluctuation in the spectra is regarded as a signature of single molecule response. The plasmonic junctions typically evolve and so does the local near field, which the molecule experiences. The molecular signature indicates presence of complicated near field, as well as the background is characterized via electronic Raman of the metal. The understanding of the entire spectra is based on the molecular response, metal response and their coupling. Polarized SERS measurements on single Au or Ag nanodimer equipped with some reporter molecule shows that the emission constituting the continuum is polarized. In a metal, bulk states can only result in scattering which is unpolarized, however, the surface states of the metal can be responsible for Raman. We assign the continuua to Raman of plasmons. The polarization decomposition of the intimately related molecular and plasmonic SERS allows mechanistic assignments of the scattering process and the nature of accessible plasmons in the prototypical dumbbell antenna.

Introduction

Surface enhanced Raman scattering (SERS) briefly refers to the phenomenon resulting in million-fold stronger Raman signal from molecules when they are adsorbed on rough metal surfaces. It was in 1974, exactly 40 years ago, when Fleichmann *et al.*[1] reported unusually bright Raman scattering from pyridine adsorbed on electrochemically roughened silver electrodes. They suggested that the enhancement may be due to the increased surface area of the roughened electrode, thereby allowing more molecules to adsorb in the probed area. It was not until 1977 when Jeanmaire and Van Duyne[2] and Albrecht and Creighton[3] independently recognized that simply increasing the number of scatterers in the interaction volume cannot account for the observed large intensities. Jeanmaire and Van Duyne explained the observation based on electric field enhancement mechanism, namely surface enhanced Raman scattering (SERS), whereas Albrecht and Creighton suggested resonance Raman scattering from molecular electronic states, which is more commonly known as chemical mechanism of Raman enhancement.

Although any metal is potent to generate surface enhancement,[4] SERS is primarily observed for molecules adsorbed on coinage metals (Ag, Au, Cu) or alkali metal (Li, Na, K) for visible excitation.[5] The enhancement of Raman signal in SERS generally involves two mechanisms: chemical enhancement and electromagnetic (EM) enhancement. Chemical enhancement depends on chemical specificity of the molecules which associates changes to the adsorbate electronic state due to chemisorption geometry.[6] The electromagnetic enhancement mechanism on the other hand is associated with the excitation of localized surface plasmons and the strength of their electromagnetic fields near the surface. These fields can be significantly larger than the incident fields. Together, chemical and EM enhancement may lead to an overall average enhancement of ~10^5-10^{12}. Although the first measurements were performed on Ag

electrodes, huge variations of roughened surface and colloidal surface has been used as SERS substrates. In such structures, there exist local regions with strongly enhanced electromagnetic fields, which are known as hot-spots. The hot-spot can be a sharp corner or a molecular asperity or more commonly a metallic junction on ~nm lengthscale. For EM enhancement factor η, local electric electric field is $E_{loc} = \eta E_{in}$, and SERS signal $I_{SERS} \sim I_{loc}^{4} \sim \eta^{4} I_{0}$. This led to the concept that larger enhancement in SERS is possible if the probing area is selectively chosen to be a hot spot created by the excitation. Clear proof of the existence of hot-spots came along from the single molecule SERS measurements, when Nie and Emory[7] and Kneipp *et al.*[8] claimed intrinsic Raman enhancement of the order of 10^{14}. Although an upper limit of 10^{10} is established[9] for SERS, huge enhancement of electric field in SERS made single molecule detection achievable.

Fluctuation in SERS is indicative of single (few) molecule limit. This is predominantly due to the evolution of the plasmonic nano-junction. A prerequisite to achieve single molecule sensitivity is a junction of size ~ 1 nm. Atomic scale asperity is a characteristic feature at this length scale, and cannot be ignored. Additionally, under irradiation intensities of 1 mW/μ^2, we recognize evolution and fusion of Ag junctions through simultaneous SERS/AFM measurements. The first set of measurements in this regard was carried out on chemically engineered, bare silver dumbbells. Very similar same observations were also made on silica encapsulated gold nansosphere dimers. In the latter case, we verify through TEM that the plasmonic junction evolves and fuses, without a noticeable change to the overall shape of the plasmonic object. The evolution is in Å scale, at which fusion occurs. Even though the evolution events are stochastic, they possess unique spectroscopic signatures in the form of fluctuations in signal from reporter molecules present in that junction.

Non-resonant (NR)-SERS can be used to uniquely establish local field and field gradients. We identify the fluctuating SERS as gradient driven Raman (GDR) where IR lines appear in Raman spectrum.[10] More importantly we recognize the presence of significant field gradients that generate magnetic and quadrupolar Raman. The formulation is brought to closure using electric magnetic dipolar (G') and electric quadrupolar (A) tensors along with molecular polarizability (α) tensor as obtained from Raman optical activity (ROA) calculations. In addition to normal Raman spectra (NRS) of the molecule, we see clear signature of surface-enhanced dipole-quadrupole Raman (SEQRS) and surface-enhanced dipole-magnetic Raman (SEMRS) in the fluctuating spectra.

The tensor nature of SERS in the single molecule limit has broader implications, beyond mere assignment of fluctuating spectra. It is possible to identify the local fields and quantify the corresponding enhancement. Local fields and field gradients govern the near field excitation of molecules, and they can be dramatically different than than the freely propagating applied EM waves in the far field. Once the multipolar spectra of the molecule is assigned, we can deduce the molecular orientation with respect to the local electric field, and this can be regarded as the equivalent of the molecular Global Positioning System. The most complete description of the scattering tensors arises from polarization resolved Raman measurements, which we describe in Chapter xx..

Sub-nm gap size in a plasmonic junction sustains charge transfer plasmons, and these can be seen in molecular spectra as charge transfer resonances (CTPR). The effect occurs when current tunnels across the junction, and the molecule acts as a bridge. In the limit of field plasmons being shorted by molecules, dramatic enhancement in the integrated scattering intensity occurs along with spectral broadening due to inelastic electron scattering.

SERS is generally accompanied with a broad background, which we identify as electronic Raman scattering (ERS) of the metallic nanostructure. We show that the anti-Stokes ERS allows the determination of the temperature of the hotspot. In effect, we identify a nano-thermometer, which measures local temperature. Using this thermometer, we show that Au/Ag nanospheres reach their melting point at irradiation intensities of $1mW/\mu m^2$. Noting that atomic mobility in the bulk of solids occurs near 1/3 melting point, and surface atom mobility is significantly lower, the intensity dependent measurements of temperature rationalize the observation of surface reconstruction and junction gap fusion during SERS measurements.

Au nanosphere dimer of diameter ~100 nm is dominated by radiative damping of plasmons, as such the ERS of the metal dominates the background. The spectrum can be quantitatively understood through as electron-hole scattering among k-states perpendicular to the surface. In contrast with all prior measuremenst of SERS which rely on the molecular reporter, we now have a method to interrogate the Raman excitation of the metallic structure. Through polarization sensitive measurements, we directly relate the (third-order) polarization of the antenna and the molecule. We show that the dipolar plasmons carry the molecular signal, and the quadrupolar Raman of the nano-antenna does not couple to the molecular SERS. The near field response of the antenna has chiral response, which implies very different EM excitation of the molecule than that possible with far field transverse EM waves. We show that the handedness of the chiral response does not have a trivial relation with the structure of the antenna. The generation of chiral fields on seemingly achiral structures is a subject of great interest, with many possible applications in light management and in ultrasensitive detection of molecular chirality.

Having identified ERS of the metal and SERS of the molecule, we can clearly identify the cross terms; namely, metal to molecule Raman scattering, what may be regarded as the

CTPR of plasmon-molecule coupled system. The signature of this is nonlinear intensity dependent response and dispersive lineshapes that dramatically broaden with irradiation intensity.

In effect, this thesis quantitatively addresses details of SERS that up to present were the subject of speculation.

REFERENCES:

(1) Fleischmann, M.; Hendra, P. J.; McQuillan, A, J. Raman Spectra of Pyridine Adsorbed at a Silver Electrode. *Chem. Phys. Lett.* **1974**, *26*, 163–166.

(2) Jeanmaire, D. L.; Duyne, R. P. Van. Surface Enhanced Raman Spectroelectrochemistry. *J. Electroanal. Chem.* **1977**, *84*, 1–20.

(3) Albrecht, M. G.; Creighton, J. A. Anomalously Intense Raman Spectra of Pyridine at a Silver Electrode. *J. Am. Chem. Soc.* **1977**, *99*, 5215–5217.

(4) Moskovits, M. Surface-Enhanced Spectroscopy. *Rev. Mod. Phys.* **1985**, *49*, 2224–2826.

(5) Garrell, R. L. Surface-Enhanced Raman Spectroscopy. *Anal. Chem.* **1989**, *61*, 401A – 411A.

(6) Weaver, M. J. .; Shouzhong, Z.; Yeung H. Chan, H. The New Interfacial Ubiquity of SERS. *Anal. Chem.* **2000**, *72*, 38A – 47A.

(7) Nie, S.; Emory, S. R. Probing Single Molecules and Single Nanoparticles by Surface-Enhanced Raman Scattering. *Science (80-.).* **1997**, *275*, 1102–1106.

(8) Kneipp, K.; Wang, Y.; Kneipp, H.; Perelman, L.; Itzkan, I.; Dasari, R.; Feld, M. Single Molecule Detection Using Surface-Enhanced Raman Scattering (SERS). *Phys. Rev. Lett.* **1997**, *78*, 1667–1670.

(9) Etchegoin, P. G.; Lacharmoise, P. D.; Le Ru, E. C. Influence of Photostability on Single-Molecule Surface Enhanced Raman Scattering Enhancement Factors. *Anal.* **2009**, *81*, 682–688.

(10) Whitmore, D.; El-khoury, P. Z.; Fabris, L.; Chu, P.; Bazan, G. C.; Potma, E. O.; Apkarian, V. A. High Sensitivity Surface-Enhanced Raman Scattering in Solution Using Engineered Silver Nanosphere Dimers. *J. Phys. Chem. C* **2011**, *115*, 15900–15907.

CHAPTER 1:

Surface-enhanced Raman scattering of a single nano-dumbbell: dibenzyl-dithio-linked silver nanospheres

1.1 Abstract

We describe combined AFM/Raman measurements on single nano-dumbbells, consisting of silver nano-spheres linked with dibenzyl-4,4'-dithiol (DBDT). The measured surface enhanced Raman scattering (SERS) enhancement factor EF_{exp} = 3x10^7 at 532 nm corresponds to the observed signal strength of a single DBDT molecule, the Raman cross-section of which is determined as $d\sigma/d\Omega$ = 6 x10^{-28} cm^2/sr. We show that the product of the local field enhancement $EF_P = (E_i/E_0)^2(E_s/E_0)^2$ = 3x10^6 and the chemical contribution due to reduced detuning $EF_C = (\Delta_0/\Delta)^2$ = 12 account for the observed effect. The chemical contribution is assessed by exploring model structures Ag_n-S-DB-S-Ag_m (n,m = 0,3,7,20). The π-π* transition at 287 nm, which determines the polarizability of the bare molecule, acquires a DBDT-to-silver charge transfer character upon binding to silver. The CT near 400 nm reduces the detuning but remains non-resonant at 532 nm. We observe a soft polarization dependence, suggesting optical activity, which in part is ascribed to coupling between plasmon and conjugated electrons of DBDT. Modest enhancement factors are sufficient to detect single molecules through non-resonant SERS.

1.2 Introduction

By taking advantage of the large plasmonically enhanced local fields at junctions of metallic nano-structures, Raman scattering with single molecule sensitivity can be attained. Since the early demonstrations,[1–3] there has been significant development of the field as highlighted in a recent review.[4] Such developments have been made possible through enhancement of the feeble Raman effect, through mechanisms collectively identified as surface enhanced Raman scattering (SERS). Since its discovery,[5,6] SERS has developed as a field of wide-impact and applications.[7,8] Nevertheless, understanding the underlying coupled dynamics between molecular excitations and collective plasmons remains a challenge. Beside its inherent interest, exploration of single molecules through SERS (SMSERS) can be expected to lead to a deeper understanding of the governing principles in SERS. Multiple approaches have been pursued to reach and prove single molecule sensitivity.[1,9–11] The common approach is to first create plasmonic structures, and to then coax molecules into inter-particle gaps – "hot spots" where fields are largest.[4,12–15] This strategy generates a distribution of nano-junctions, and associated with them, a heterogeneous field terrain over which molecules are sprinkled with uncertain orientation. Given the nonlinearity of the SERS response, spatial and orientational averaging of observables leads to uncertainty. We take a different approach. To investigate molecules at a single well-defined structure, we rely on thiolation chemistry to link two nanospheres with the target molecule.[16–18] By design, the linker is positioned at the hot spot with inter-sphere gap defined by the length of the molecule. The approach yields the required sensitivity to interrogate single molecules under ambient conditions, as recently illustrated using distyril benzene linked silver nano-spheres in aqueous solution.[19] There, the concept was to equip molecules with antennae to address them individually. Here, through combined atomic

force microscopy (AFM) and Raman micro-spectroscopy, we investigate single dibenzyl-dithio-linked silver dumbbells, dry-mounted and isolated on a microscope slide. The 1.2 nm sulfur-to-sulfur length of the π-conjugated dibenzyl-dithiol (DBDT) defines the inter-sphere gap, a consistency check of which is provided through TEM images. The immobilized dumbbells, with defined structural and spatial alignment, allow analysis of the operative photophysics. The most mundane of the considerations is the magnitude and mechanism of the enhancement that enables observations at the single molecule level, to which we limit the first of this series of reports.

Enhancement factors as large as $EF = 10^{11}$-10^{14} are reported in SMSERS studies.[1,20,21] Such large values can arise from multiplicative contributions of physical and chemical factors, $EF = EF_P EF_C$, the latter implying significant modification of the electronic structure of the target molecule. If indeed this were necessary, then the utility of SMSERS would be somewhat limited. We demonstrate that this is not the case. Rather modest enhancement factors, accessible via locally enhanced fields are sufficient to reach single molecule sensitivity. This can be shown with some generality. Note, the Raman scattering intensity of a molecule embedded in a medium is given in terms of its gas phase, angle-integrated cross section σ_{nm} (cm^2):[22]

$$I = L(\omega) I_0 \sigma_{nm} \qquad 1.1$$

in which I is the scattering rate (s^{-1}) integrated over the Raman line profile of the transition between vibrational levels m,n of the ground electronic state; I_0 is the incident light intensity (photons cm^{-2} s^{-1}), and $L(\omega)$ is the local field correction. $L(\omega) = 1$ in rarified media, while in an isotropic dielectric such as that of a liquid, the correction is well approximated by the Clausius Massotti relation:

$$L(\omega) = (E_i/E_0)^2 (E_s/E_0)^2 = [(n_i^2 + 2)/3]^2 [(n_s^2 + 2)/3]^2 \qquad 1.2$$

where $n_{i,s}$ are the indices of refraction at the incident and scattered frequencies. In the standard

approximation the SERS intensity is:

$$I_{SERS} = (EF) I_0 \sigma_{nm} = (EF_P EF_C) I_0 \sigma_{nm} \quad 1.3$$

where $EF_P \equiv L(\omega)$ is the local field correction, same as in eqn. 1.3 but now arising from the plasmonic nano-structure;[23–26] while $EF_C \equiv \sigma'_{nm} / \sigma_{nm}$ recognizes that the molecular cross section may be modified upon binding to the SERS substrate.[27] The incident intensity in eqn. 1.3 cannot be arbitrarily increased. We show that consistent with prior analyses,[28] intensities that significantly exceed 1 mW/μm^2 (I_0 = 2.5×10^{23} photons cm^{-2} s^{-1}) perturb the nano-junction through light-induced forces. Within this limitation, to observe a single molecule at a count rate of 10^3 s^{-1} and a detection efficiency of 10^{-2}, the requirement is for the product: $EF\sigma_{nm}$ = 4×10^{-19} cm^2. For a non-resonant scatterer such as benzene ($\sigma = 4\pi d\sigma/d\Omega$ = 9×10^{-29} cm^2 at 514 nm)[29] an enhancement factor of EF = 4×10^9 is required. With an astute choice of wavelengths, in principle, such enhancements can be attained at hot spots of nanosphere dimers, which have been extensively analyzed previously through numerical [22,30–32] and analytical [28,33–35] classical electrodynamics and quantum [36–38] treatments. The Raman cross section of DBDT is two orders of magnitude larger than that of benzene, therefore detectable with a modest EF of ~10^7, as in the closely related distyrilbenzene system.[19] For a resonant Raman scatterer, such as the extensively used rhodamine dyes for which σ = 4×10^{-22} cm^2,[39] an EF of 10^3 is sufficient to detect a single molecules. Clearly, resonant Raman (RR) of single molecules is detectable by modest enhancements, and competes with fluorescence. Both processes are determined by spontaneous radiation: RR, prior to dephasing; and fluorescence, post dephasing. As such, the branching ratio between RR and fluorescence channels, k_r/γ,[40] is determined by the competition between the dephasing rate of the initially prepared state, γ, and the enhanced rate of spontaneous radiation $k_r = (E_s/E_0)^2/\tau_r$, the local field effect that can be cast alternatively in terms of the modified vacuum

or reradiation.[31] Reduction of the ns radiation time of a dye molecule by 10^3, puts it in the range of dephasing times (ps), where RR competes with fluorescence. It would therefore be difficult to reconcile much larger enhancement factors with RR scatterers.[2] Giant enhancements would be expected only if an otherwise non-resonant response were to shift into resonance as a result of molecule-substrate coupling.

Our experimental findings are consistent with the above analysis. We show that a single non-resonant DBDT molecule that bridges a nanosphere dimer is observable. Since the molecule is chemically attached to silver, we explore the potential role of chemical contributions through electronic structure calculations on model systems: Ag_n-S-DB-S-Ag_m (n,m = 1,3,7,20).[27,41–43] We conclude that the contribution of chemical effects to the overall EF is minor ($EF_C \sim 10$). The surprising finding is a mild polarization dependence of the Raman response of the dumbbell, which we cannot explain by explicit analysis of the local fields of idealized nanospheres. We will ascribe this shortcoming to the limitation of analyses that treat the nano-structure as an effective medium, ignoring coupling between plasmon and molecule.

1.3 Experimental Methods

1.3.1 Sample Preparation

The synthetic strategy and method has been previously reported in some detail.[18] Briefly, a colloidal suspension of 35±5 nm citrate capped silver nano-spheres is prepared with a narrow size distribution. The citrate is then exchanged with bis(p-sulfonatophenyl) phenylphosphine (BSPP), which serves as a protective capping agent. A 1mM DBDT solution is added to the suspension, allowed to sit for ~3 hrs, followed by centrifugation. The resulting solution consists of ~50% nano-sphere dimers, as evidenced by TEM images, see fig. 1.1. Inspection of

suspensions stored over extended periods of time (several months) reveals a gradual increase in the monomer fraction. The low yield of aggregates is an indication that few DBDT linkers are attached to the surface of a given nanosphere. Although, a variety of inter-sphere gap morphologies are observed in TEM images, ranging from sharp protrusions to elongated inter-sphere planar channels, the inter-sphere gap of inspected dimers is ~1 nm, consistent with the length of the linker. While electron microscopy does not resolve the number or location of linker molecules, it does establish the success of the synthetic strategy to prepare DBDT-linked silver nano-spheres (dumbbells).

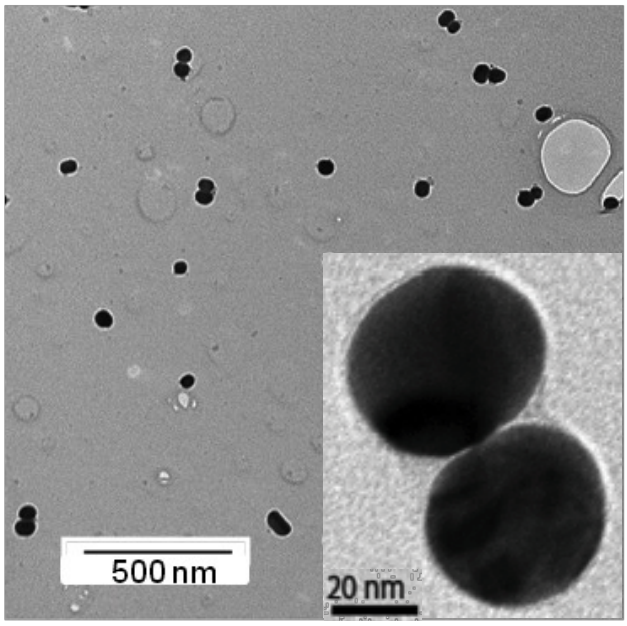

Figure 1.1: TEM image of a freshly prepared sample and close-up of a dumbbell.

1.3.2 Combined AFM/Raman Measurements

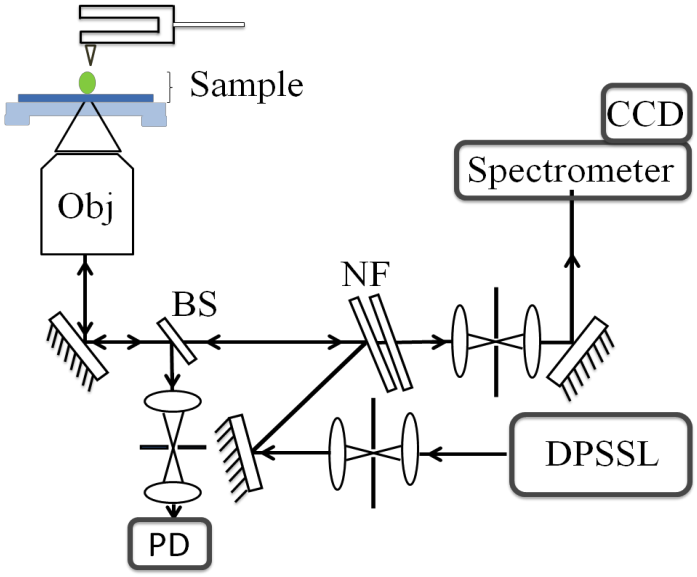

Figure 1.2: Schematic of the AFM/Raman setup. The tip and sample are on independent scanning stages. The tip is aligned with the laser using backscattered light, which is spatially filtered and monitored using a photodiode. Imaging is accomplished by scanning the sample. The spectra are recorded in the backscattered geometry, using a spatial filter to establish confocality. Obj: objective, BS: beam splitter, PD: photodiode, NF: notch filters, DPSSL: diode-pumped solid-state laser.

Joint AFM/Raman measurements are carried out under ambient conditions, on dry mounted particles prepared by spin-coating or drop casting a ~5 pM solution on a 150 micron-thick microscope slide. A dilute solution of polyvinyl alcohol (PVA) is added to the aqueous suspension prior to coating, and the slides are either pre-heated or heat cycled on a hot plate after preparation. The polymer film provides the mechanical stability required for AFM imaging, and serves as the essential heat sink for thermal stability under tightly focused laser irradiation. A schematic of the combined scan-probe (NT-MDT) / micro-Raman instrument is shown in fig. 1.2. The scanning base/head is assembled on an inverted optical microscope frame (Olympus, IX71). The AFM tip is aligned with the laser by monitoring back-scattered light. The sample is scanned for imaging purposes. Either a tuning fork AFM (TFAFM) or a cantilever is used, both

yielding comparable spatial resolution. The TFAFM tips were prepared by electrochemical etching a 100 μm-thick tungsten wire, followed by ion-beam milling to produce tips with cone radii as small as 20 nm. The excitation source is a continuous wave, single mode laser (CrystaLaser) operating at λ = 532 nm. The laser is focused on the sample using a 1.25 NA oil immersion lens. Backscattered Raman light is collected using a pair of notch filters (Semrock, $1:10^6$ extinction). The spatially filtered scattered light is then spectrally dispersed in a 0.25-m monochromator and recorded on a CCD array (Andor, V401-BV). The effective instrument resolution is 10 cm^{-1}.

1.4 Computational Methods

Calculations were performed using the methodologies implemented in Gaussian 09.[44] We truncate the multi-electron problem by approximating silver nanoballs with six different models, (i) single silver atoms, (ii) three silver atoms, and (iii) seven silver atoms, on either one or both sides of DBDT. Unconstrained geometry optimization was performed using the B3LYP[45] functional. All reported calculations employ the def2-TZVP basis set[46] with matching pseudopotentials for silver (> 1000 basis functions). The optimized structures are verified to not have imaginary vibrational frequencies. Vertical transition energies calculated for all considered structures are at the B3LYP/def2-TZVP minima. Three additional functionals were tested: (i) the PBE0 functional,[47] (ii) the CAM-B3LYP functional,[48] and (iii) the M06-HF functional.[49] The B3LYP functional employs three empirical parameters to combine exact exchange, gradient-corrected exchange, and local-spin density exchange, whereas the PBE0 functional uses perturbation theory to define a ratio of 25% HF exchange and 75% exchange from the functional. The CAM-B3LYP functional is a hybrid exchange-correlation function featuring a long-range

correction to B3LYP using the Coulomb attenuating method. The M06-HF functional has full Hartree-Fock exchange, which eliminates self-exchange interactions at long range. To bridge between the current and previous works, we also computed the Raman spectrum of DBDT bound to tetrahedral Ag_{20}.[50] The B3LYP/def2-TZVP frequency dependent polarizability derivatives were computed using the ROA module in Gaussian 09, in which these tensor elements are computed as a sum over all electronic states, *n*:[51,52]

$$\alpha_{\alpha\beta} = 2\sum_{n\neq 0} \omega_{n0} \frac{Re[\langle 0|\mu_\alpha|n\rangle\langle n|\mu_\beta|0\rangle]}{\omega_{n0}^2 - \omega_i^2} \quad 1.4$$

where $\alpha,\beta = x,y,z$, and ω_i is the frequency of the incident light. The polarizability derivatives with respect to normal modes are computed at the optimized ground state geometry:[52]

$$\langle \nu_0|\alpha_{\alpha\beta}|\nu_{1p}\rangle\langle \nu_{1p}|\alpha_{\alpha\beta}|\nu_0\rangle = \frac{1}{2\omega_p}\left(\frac{\partial\alpha_{\alpha\beta}}{\partial Q_p}\right)\Big|_{re}\left(\frac{\partial\alpha_{\alpha\beta}}{\partial Q_p}\right)\Big|_{re} \quad 1.5$$

where ν_0 and ν_{1p} are the ground and first excited vibrational state of the p^{th} normal mode. The differential Raman scattering cross sections are defined in terms of scattering intensities, S_i:

$$\frac{d\sigma}{d\Omega} = \frac{(2\pi)^4}{45}\frac{h\omega_s^4}{8\pi^2 c\omega_p}\left(1 - e^{-\frac{hc\omega_p}{k_B T}}\right)^{-1} S_i \quad 1.6$$

where $S_i = (45\alpha'^2_p + 7\gamma'^2_p)$ and α'_p and γ'_p are the spherical part and anisotropy of the polarizability derivative of the *p*-th normal mode. Note, this definition is appropriate for orientationally averaged scatterers, detected at 90° relative to excitation. For molecules oriented in space, individual tensor elements (see eqn. 1. 5) are used, and the factor of 45 is dropped in eqn. 1.6.

1.5 Results and Discussion

The AFM image of a dumbbell and its Raman spectrum are shown in figs. 1.3 and 1.4, respectively. While the vertical spatial resolution of the AFM is reliable, the lateral resolution is determined by tip-convolution. The clearly resolved dumbbell structure (fig. 1.3a) is canted relative to the surface plane due, in part, to the asymmetry of the nanospheres. The ellipsoid (fig. 1.3b) appears as a fused dumbbell, which does not show any Raman activity. The AFM is used to establish that the nano-structure is a dumbbell of consistent dimensions, to define its spatial orientation, and to ensure that it is isolated in the field of view of the spectrometer. Under typical irradiation intensities of ~1 mW/μm^2, we do not detect Raman activity on isolated single nano-spheres. At intensities of ~50 mW/μm^2, which leads to melting and fusion of dumbbells, we have observed faint spectra on some single nano-spheres. Consistent with our prior report [19], an upper limit on the relative intensity of Raman scattering on single sphere versus dimer is ~ 10^{-3}. In few cases, *e.g.,* structure (b) in fig. 1.3, we have located what appear as dumbbells that do not exhibit Raman activity. This can be ascribed to either loss of the linker during the preparation of the slide, or light induced fusion of dumbbells that are not well-anchored by the PVA film. Otherwise, Raman intensities of different dumbbells are comparable (~10^3 photons/s). While the synthetic route affords coating of nano-spheres with many DBDT molecules, the absence of detectable Raman on single spheres establishes that the observed spectra arise from molecules located at the hot spot of dumbbells. The spectrum does not show spectroscopic signatures of interacting linkers, such as splittings observed in clusters[19]. All indications are that the observed spectra are those of single molecules. The enhancement factors we obtain are consistent with this assumption.

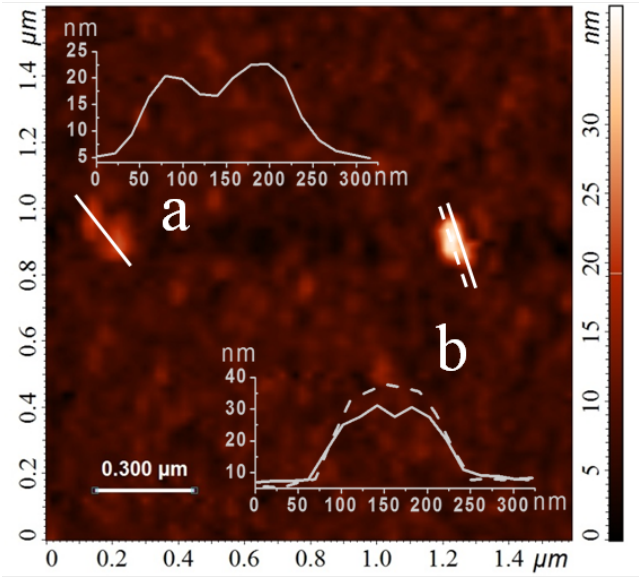

Figure 1.3: AFM image showing (a) an isolated dumbbell, on which the spectra in Fig. 1.4 were recorded, (b) a fused dumbbell, which does not exhibit Raman activity. The associated line profiles are highlighted in the inset. The heights correctly measure the diameter of the nanospheres, while the lateral profiles are determined by the tip convolution.

We give two independent determinations of the SERS enhancement factor. The first relies on the observed signal strength and the measured cross section of DBDT, the second relies on the relative measure of the number equivalent of DBDT molecules that yield the same signal. We establish that the Raman cross section of the aromatic C=C stretch of DBDT, at 1580 cm^{-1}, is two orders of magnitude larger than the symmetric stretch of benzene. Experimentally, we find σ(DBDT)/σ(benzene) = 200, by measuring spectra of liquid benzene and DBDT/ethanol solutions contained in a thin cell (30 micron) under identical conditions. The measurement agrees with our DFT calculations, which yield a ratio of 100 ($d\sigma/d\Omega = 6\times10^{-28}$ for bare DBDT). For a single molecule immobilized in the field of view of the objective, to detect the count rate of 1.2×10^{3} photons s^{-1} seen in fig. 1.4, the required *EF* can be determined:

$$I = EFI_0\eta\frac{\partial\sigma}{\partial\Omega}d\Omega \sim 10^3\ s^{-1} \qquad (7)$$

based on the excitation intensity $I_0 = 2.5\times10^{23}$ photons cm^{-2} s^{-1} (1 mW/μm^2), detection efficiency $\eta = 0.1$, and a collection solid angle of $d\Omega = \int \sin(\vartheta)\, d\vartheta d\varphi = \pi$ (oil immersion lens with NA = $nsin(\vartheta)$ = 1.25, n = 1.47). We obtain $EF = 2(\pm1)\times10^7$. The largest error in this determination is the CCD conversion of photons to counts. Separately, we quantify the *EF* by recording the spectra of DBDT dissolved in ethanol using the same apparatus. A 5mM DBDT solution, sandwiched between two cover slips, yields a signal comparable to that observed from a single dumbbell. To obtain the essential scattering volume of the liquid, we assume the Rayleigh waist of the objective (0.4 μm) and we measure the depth profile by recording the Raman signal of a silicon wafer by translating it along the *z*-axis of the objective. The obtained volume, 2.5±0.5 pL, yields an experimental enhancement factor of $EF = V\, M\, N_A = 7.5\times10^6$ relative to the molecule in solution. Taking the liquid local field correction, eqn. 1. 4, into account, $[(n^2+2)/3]^4 = 4$, we obtain $EF_{exp} = 3(\pm1)\times10^7$. The two different determinations are well within the errors of the methods.

As long as the excitation intensity is maintained near ~1 mW/μm^2, within our spectral resolution, the observed Raman lines do not show spectral fluctuations. This is illustrated in fig. 1.4 with the set of consecutively recorded spectra at an exposure time of 10 s per spectrum. The subtraction of one of the spectra from the rest shows a slow fluctuation in overall intensity, but no spectral shift. That the excitation intensity cannot be increased arbitrarily is illustrated by the non-monotonic intensity dependence of the Raman lines shown in fig. 1.4b. The sudden drop in spectral intensity is indicative of light-induced change in the orientation of the molecular axis relative to the dumbbell. Both spectral and intensity variations can be induced optically, leading to both reversible and irreversible Raman trajectories. Here, we simply note that the observed intensity threshold for such light-induced manipulation is

consistent with prior estimates of field strengths required to move molecules and to collapse the dumbbell (26, 27) We limit the present report to unperturbed dumbbells.

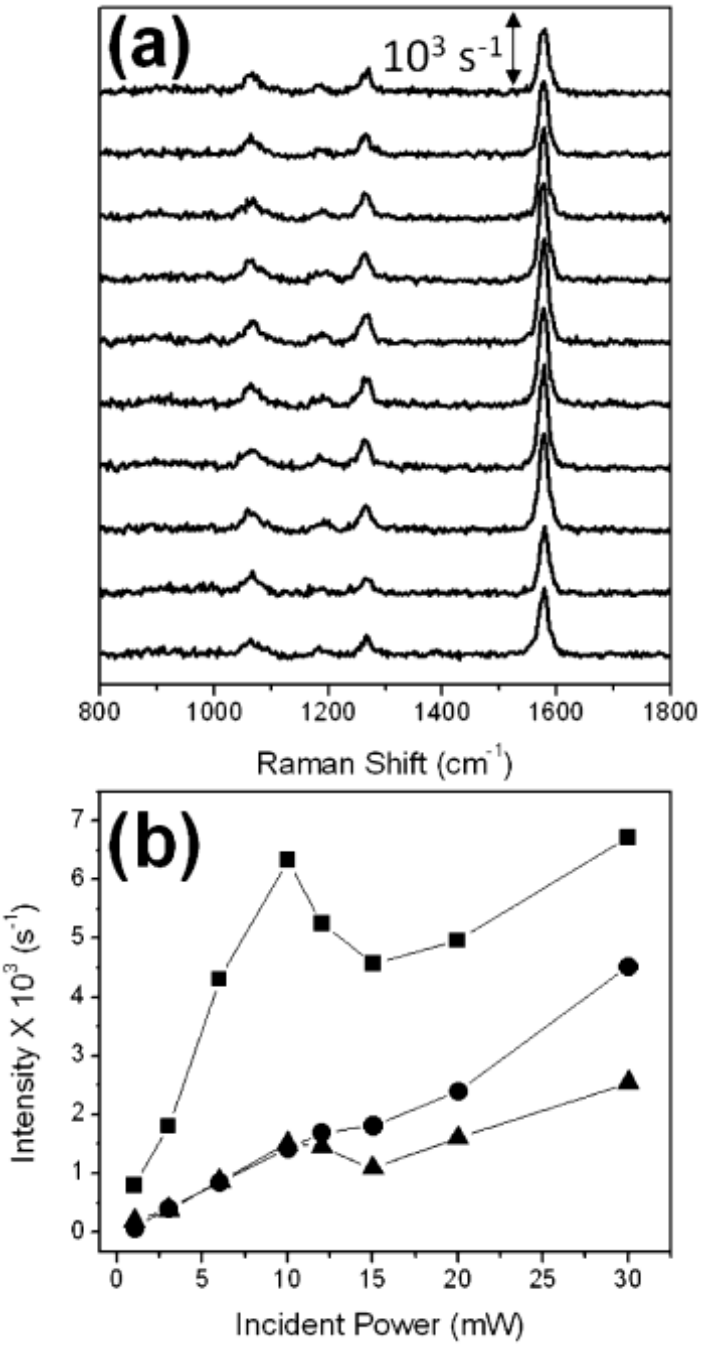

Figure 1.4: (a) Raman spectra recorded consecutively on a dumbbell (10 s exposure per spectrum). The spectra are vertically displaced for clarity. (b) Power dependent intensity of the 1579 (■), 1492 (▲), and 1271(●) cm^{-1} fundamentals. The ordinates are the calibrated count of photons/s.

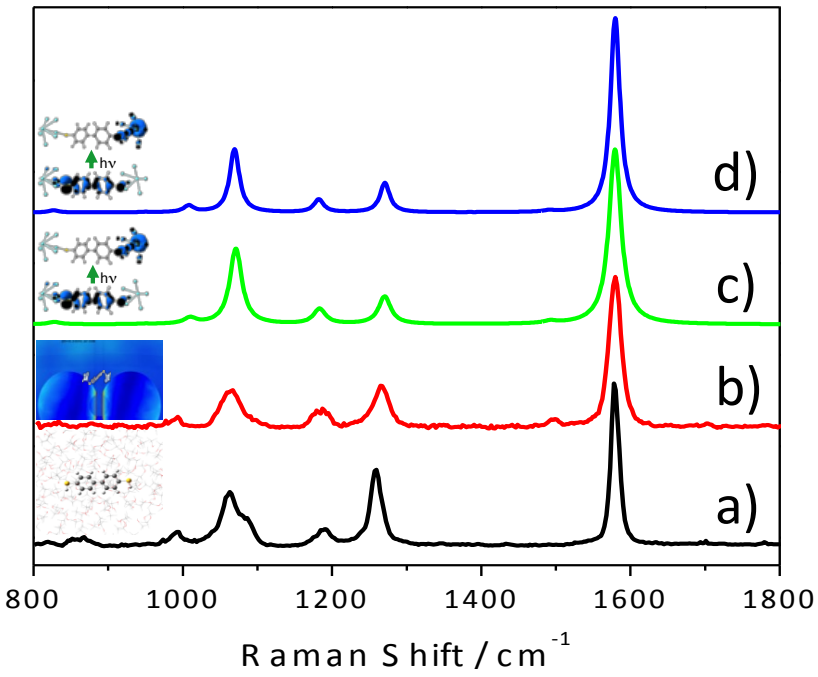

Figure 1.5: Raman spectra: (a) a 5 mM DBDT/ethanol solution, (b) SERS on a single dumbbell, (c) orientationally averaged spectrum of Ag_7-DBDT-Ag_7 computed at B3LYP/def2-TZVP level, (d) computed spectrum for excitation and detecton polarization aligned along the long axis of the molecule. Shown next to the individual spectra is a schematic representation of: (a) solvated DBDT, (b) dumbbell, (c,d) the electron and hole density of the DBDT-to-silver CT transition.

The Raman spectrum of DBDT on a single dumbbell is nearly indistinguishable from that of the solvated molecule, and is reproduced by the computed spectrum shown in fig. 1.5. The B3LYP/def2-TZVP spectrum corresponds to the Ag_7-S-BP-S-Ag_7 model, scaled by a factor of 0.976 to align the aromatic C=C stretch with its experimental counterpart at 1580 cm^{-1}, and the lines are broadened by 10 cm^{-1} (FWHM) to match the instrument resolution. The agreement between the experimental and computed spectra gives confidence to the assignments collected in table 1.1. There are small differences in the calculated spectra of the considered silver structures (see supporting material). We find the calculated spectral shift of a given mode to vary by ~ 2

cm^{-1} in the considered structures, well within our experimental resolution of 10 cm^{-1}. These variations can be associated with the chemical effect in various binding structures, as noted in a prior analysis.[41] The effects are minor, undetectable in our system, and the binding to the nanosphere seems to be captured by the Ag_7-S-BP-S-Ag_7 model. The similarity between the dumbbell and liquid phase spectrum of fig. 1.5a,b is also remarkable, since it is not obvious that the spectrum of a molecule fixed in spatial orientation should mimic that of the orientationally averaged liquid phase spectrum. This occurs in the aromatic DBDT molecule because the polarizability determined by the π–π* transition at 285 nm is strongly anisotropic: for all Raman active modes $\alpha'_{xx} >> \alpha'_{\alpha\beta}$ where *x*- defines the long axis of the molecule. The same holds for the molecule upon binding to silver, even though now the DBDT-to-silver charge transfer transition (fig. 1.5 inset) determines the polarizability. The orientationally averaged spectra are dominated by the *x*-polarized component. Assuming an enhanced local field along the dumbbell axis, the appearance of the spectrum in fig. 1.5 is essentially unchanged for ± 50° angles between molecule and dumbbell.

Table 1.1: The experimental and B3LYP/def2-TZVP vibrational frequencies, relative intensities, and spectral assignments. See text for more details.

Mode	Calculated			Experimental			Assignment
	Frequency / cm^{-1}	Relative Intensities		Frequency / cm^{-1}	Relative Intensities		
	($Ag_{(7)}$-$Ag_{(7)}$)	DBDT	$Ag_{(7)}$-$Ag_{(7)}$	(SERS)	Solution	SERS	
1	1579	1	**1**	1580	1	**1**	*aromatic C=C stretch coupled to C-C stretch*
2	1492	0.03	**0.01**	1493	-	**0.05**	*HC=CH rock*
3	1271	0.30	**0.15**	1267	0.44	**0.28**	*C-C ctretch*
4	1183	0.05	**0.08**	1185	0.06	**0.13**	*HC=CH dihedral bend*
5	1071	0.11	**0.35**	1065	0.30	**0.24**	*C-S stretch*
6	1010	0.01	**0.02**	994	0.04	**0.07**	*in-plane aromatic ring deformation*

Given the fact that polarizability along the long axis of the molecule dominates and the same holds for the polarization of the dumbbell, a dramatic contrast between excitation parallel versus perpendicular to the intersphere axis would be expected. This is not the case, as shown in fig. 1.6. We observe a soft polarization dependence with a contrast ratio between maximum and minimum intensity of 5-20 observed on different dumbbells. A survey of polarization dependent studies of SERS on similar structures shows a great variety of reported results. They range from relatively soft dependences of 5:1[53] or 10:1[54] to a relatively large (almost infinite[55]) contrast. Two experimental considerations can be suspected to reduce the contrast ratio: tilting of the

dumbbell relative to the slide plane, and the longitudinal component of the polarization that is generated by high NA objectives. Assuming an input field $E^0 = E_T^0 + E_L^0$ projected along the dumbbell axes, $E_\parallel^0 + E_\perp^0$, and a tilt angle α of the dumbbell relative to the plane, the observed poarization dependence can be fitted to $(\beta_\parallel E_\parallel^0)^4 + (\beta_\perp E_\perp^0)^4$. Indeed, small tilt angles and longitudinal components can greatly effect the angular dependence of the scattered radiation. However, these considerations are not fundamental. The surprise is that the observed polarization dependence is not possible unless the enhancements $E_\parallel/E_\parallel^0$ and $E_\perp/E_\perp^0$, are comparble: $\beta_\parallel/\beta_\perp$ range between 1.5 and 2. This finding cannot be explained for idealized nanospheres when only linear polarization is assumed, as we show by a careful consideraion of the local field components.

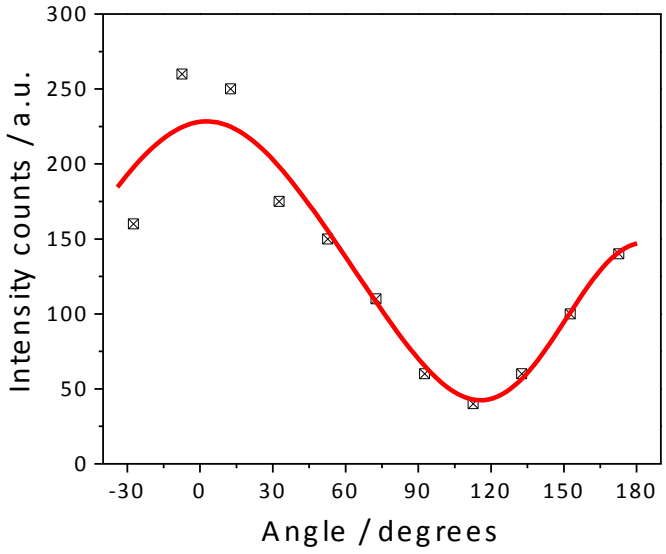

Figure 1.6: Polarization dependence of SERS on the single dumbbell, represented by the intensity of the aromatic C=C mode at 1580 cm^{-1}. The fit is to the form $(\beta_\parallel E_\parallel^0)^4 + (\beta_\perp E_\perp^0)^4$, assuming logitudinal and transvers polarization components of the incident field delivered by the microscope objective of 0.56 and 0.83. Assuming no optical activity, the observed soft contrast between the extrema (and in particular, the non-zero value reached when the field is orthogonal to the dumbbell axis) would suggest that $\beta_\parallel/\beta_\perp \sim 2$.

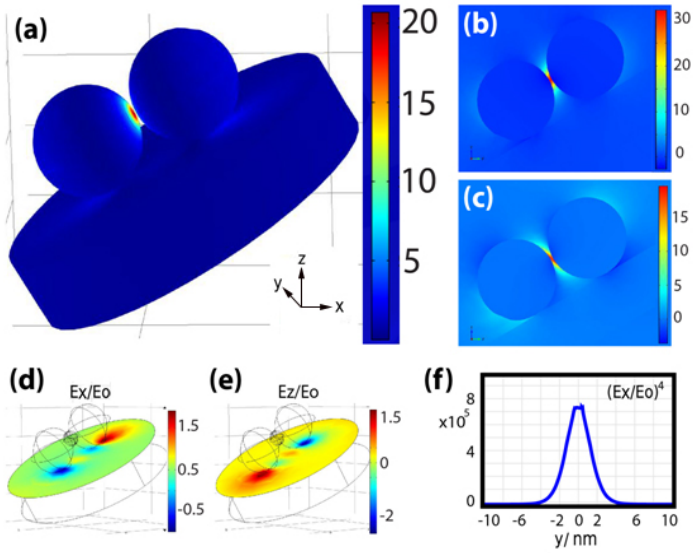

Figure 1.7: Local fields for an incident electric field $E_0 = (.65\,\hat{x} + .35\hat{z})\,e^{-ik_z z}$, with norm $|E_0| = 1$, of a silver nano-sphere dimer mounted on a glass slide: (a) Norm of the electric field on the surface of the structure. The maximum enhancement on the surface is $|E|$ =20.65; while the maximum field is attained between the nanoballs shown in (b) E_x and (c) E_z, where the maximum values reach 32.2 and 19.6, respectively. The fields on the surface of the slide are shown in (d) E_x and (e) E_z; the E_y component is negligible. The field component $E_x$along the y-axis, which is perpendicular to the connecting line between spheres, is shown in (f).

We compute the local fields of an ideal dumbbell using finite-difference time-domain (FDTD) methods,[56] with the experimentally determined dielectric response of silver as input.[57] Dumbbells have been extensively considered previously,[24,28,31–37,58] and we have cross-checked the general agreement of our calculations against several prior related studies.[59] The enhanced local fields of a dumbbell consisting of two perfect Ag spheres of 30 nm diameter, separated by a 1 nm gap and placed on a glass substrate is shown in fig. 1.7. The assumed incident field is meant to represent the polarization delivered by large NA objectives, which with the combination of the slide, can produce as much as 35% field polarized along the direction of

propagation, $\hat{z}$.[60] We note that in addition to the hot spot proper, local fields at the contact between Ag and glass are also enhanced, as previously pointed out. [25, 26] At the contacts, we find $|E|/E_o$= 2.9, E_x/E_o=1.9, E_z/E_o= 2.4, which are negligible in comparison to the hot spot between the spheres where $E_x/E_{x,o}$ = 32.2, and reaches 42 for the planar structure and incident polarization along the long axis. We have considered fused spheres as well. In the crevice of such sructures, the fields reach enhancements as high as $|E|/E_o$ = 120. The spectral dependence of the enhancement $|E/E_0|^4$ for intact and fused dumbbell are shown in fig. 1.7. The spectral response is broad, with a gentle decay over the relevant Raman window (532 nm - 580 nm). For the largest Raman shift, for long axis of the dumbbell aligned along the polarization of the incident laser field: $E_p = (E_{532}/E_0)^2 (E_{580}/E_0)^2$ values of $3\text{x}10^6$ and 7×10^8 are attained for the intact and fused dimer, respectively. The range admits the detection of single DBDT molecules, with the enhancement accessible in the intact structure being an order of magnitude smaller than the experimentally determined value. To attain the full enhancement, the long axis of the molecule must lie along the line separating the nanospheres – the observations are only consistent with molecules that bridge the two nanospheres. Although the Raman spectrum does not contain any signature of interacting linkers, to be complete, we estimate the number of scatterers that can be geometrically packed in the hot spot. The profile of EF_P in the plane separating the spheres is shown in fig. 1.7f. The enhancement drops to 50% of its maximum value at r = 1.5 nm. Based on the surface coverage of benzenethiol self-assembled monolayers on silver, 3.3×10^{14} cm^{-2},[62] a radius r' = 3 Å can be associated with the footprint of DBDT, to estimate $(r/r')^2$ = 25 as the maximum number of scatteres that may be packed into the hot spot. Unlikely as this may be, it defines an upper limit. Note, that for polarization along the short axis, the fields in the Raman window are actually reduced: $|E/E_0|^4 \sim 10^{-3}$. A polarization contrast ratio

of ~10^{10} would be expected, in stark contrast with the experiment. The experiment cannot be reconciled within a model limited to linear polarization – polarization rotation is suggested. A similar conclusion may account for the polarization dependent studies reported on R6G.[15]

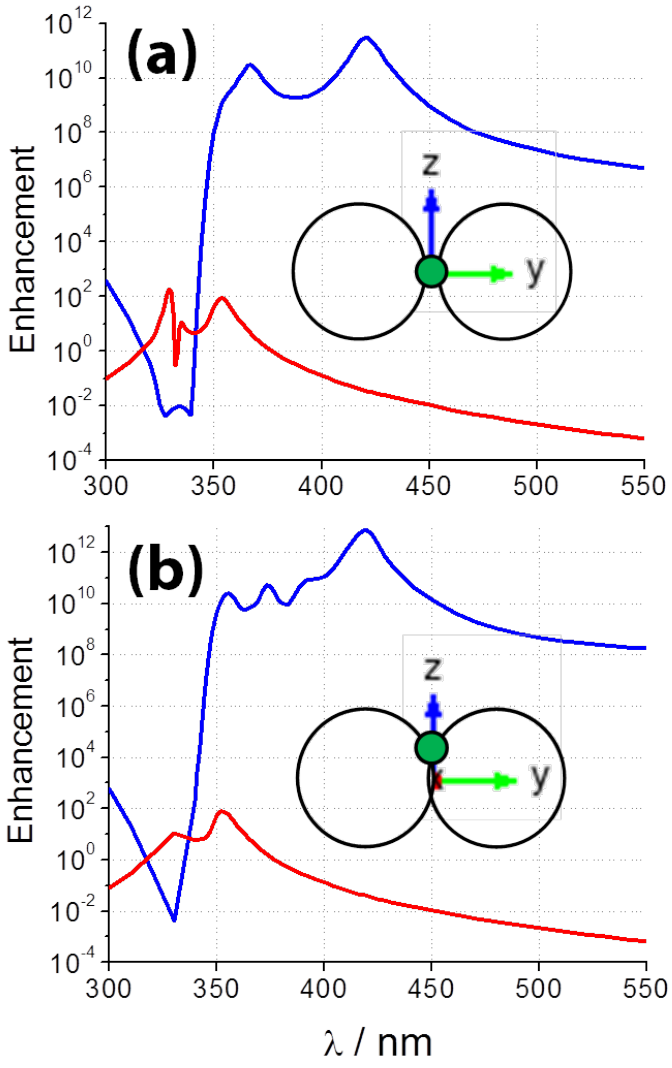

Figure 1.8: Spectral dependence of the local field enhancement, $|E|^4$, for input field $|E_0|$ =1, at two incident polarizations: (blue) $\boldsymbol{E_0 = \hat{x}\, e^{-ik_z z}}$, (red) $\boldsymbol{E_0 = \hat{y}\, e^{-ik_z z}}$. The long axis of the dumbbell is along $\hat{x}$. The hot spots, where the spectra are computed are indicated in green: (a) 1nm gap, spectrum at {0,0,0}, (b) fused nanospheres, spectrum at {0,0,3.9} nm, 2 Å above the crevice. Note, for x-polarized field at 532 nm, the enhancement in (a) is 3^4 = 81 times larger than that in (b).

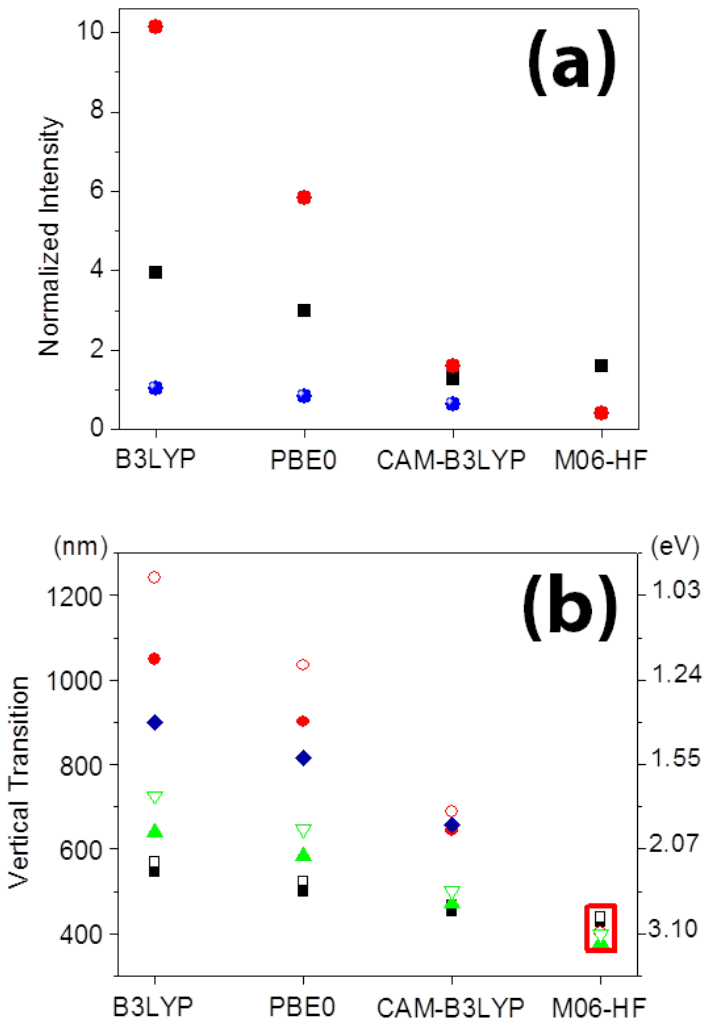

Figure 1.9: (a) Calculated static Raman intensities for the bright 1580 cm^{-1} vibrational normal mode using four density functionals. Shown are the normalized computed intensities for DBDT (●), Ag-S-BP-SH (■), and Ag_3-S-BP-SH (●). (b) Vertical transition energy calculations performed using four density functionals for the seven different model systems outlined in the main text. Shown are the computed transition energies for Ag-S-BP-SH (■), Ag-S-BP-S-Ag (□), Ag_3-S-BP-SH (●), Ag_3-S-BP-S-Ag_3 (○), Ag_7-S-BP-SH (▲), Ag_7-S-BP-S-Ag_7 (▽), Ag_{20}-S-BP-SH (♦).

We explore the chemical contribution to enhancement upon binding of DBDT to silver atoms. The initial hypothesis was that a systematic increase in the number of silver atoms might show a clear trend. This is not the case. Static scattering intensities calculated at the B3LYP/def2-TZVP level of theory is smallest for Ag(1), followed by Ag(7), and largest for

Ag(3). Vertical transition energies calculated with TD- DFT (TD B3LYP) show that the effect is entirely controlled by the energy of the DBDT-to-Ag CT transition. The CT state, which carries the oscillator strength (0.1-0.5) in both singly and doubly substituted structures, dominates the sum over states in eqn. 1. 4. This is recognized by noting that the computed scattering intensities scale as $S \propto E_{CT}^{-2}$, dictated by the energy denominator in eqn. 1.4. It is recognized that TD-DFT gives quantitatively and qualitatively incorrect descriptions of CT transitions between spatially separated regions.[51] The problem is likely to become more severe with increasingly larger clusters. Although no systematic trend is observed when the size of the cluster is increased within the same method, a systematic blue shift is observed for a given structure in going from B3LYP to M06-HF functional (fig. 1.9). The calculated energies of the CT transition converge at the TD M06-HF/def2-TZVP level to ~3.1 eV (~400 nm) as also illustrated in fig. 1.9.[63] Consistent with this finding, we observe fluorescence upon 405 nm excitation of dumbbells and DBDT coated silver wires. Although not in direct resonance at 532 nm, the CT state is nearly resonant with the dumbbell plasmon, see fig 1.9. Moreover, the CT wavefunction has significant amplitude on the terminal Ag atoms (see inset in fig 5). As such, it provides a bridge between the oscillating electron densities on individual spheres. Either as current oscillating through the molecule, or as a CT in which the electron-hole wavefunction extends beyond the confines of the molecule, a significant enhancement in the transition dipole can be expected. Incidentally, since the benzene rings of DBDT are staggered, dichroism and therefore rotational activity is to be expected. This, we suspect as key to understanding the polarization dependence. It would thus appear that the separation of the dumbbell into molecule and effective medium is a poor assumption. Nevertheless, ignoring such coupling, we can account for the overall *EF*. Since in both bare and silver-bound molecule a single state dominates the sum over states of the

polarizability:

$$\langle\alpha\rangle_{\alpha\beta} = -\frac{\langle 0|\mu_\alpha|CT\rangle\langle CT|\mu_\beta|0\rangle}{\Delta + i\hbar\gamma},\ where\ \Delta = \hbar\omega_i - E_{CT} \qquad 1.8$$

The principal chemical effect can be associated with the reduction in the detuning, Δ, which contributes to the scattering intensities, $S_i \propto |\alpha|^2$, a factor of $EF_C = (\Delta_0/\Delta)^2 = 12$. The orders of magnitude of the experimentally determined $EF = 10^7$ can be parsed as $EF_P = 10^6$ and $EF_C = 10$.

1.6 Conclusions

We report SERS spectra obtained from single dumbbells of seemingly single molecules. The primary evidence of SMSERS in the present is the agreement of the experimentally determined enhancement factor with the absolute signal strength expected from a single molecule. With the determined cross section of the bare molecule, $6\text{x}10^{-28}$ cm^2/sr, the observed signal strength corresponds to that of a single molecule subject to the measured enhancement of $2\text{X}\ 10^7$. Clearly, such a determination carries hello I am Manukh uncertainty. Our analysis puts an upper limit of 25 for the number of molecules that can be packed in the hot spot of the dumbbell, and this does not change the essential conclusions that we make here. We show that physical enhancement factors are in effect sufficient to see a single non-resonant scatterer, although an additional factor of $\text{EF}_\text{C} = (\Delta_0/\Delta)^2 = 10$ is effective in the measurements at 532 nm. That the chemical effect is relatively small is manifested by the unaltered spectrum of DBDT on the dumbbell. In both the molecular π–π^* transition and the DBDT-to-silver CT state, the polarizability ellipsoid has the same anisotropy, dominated by the long axis of the molecule – hence the observed similarity in spectra and their independence of orientational averaging. Notwithstanding the successful accounting of the enhancement factors, the analysis assumes separation of the dumbbell into molecule and plasmonic medium, with an admixture of quantum and classical treatments of the

constituting parts. The electron/hole density (fig. 1.5) associated with the CT state suggests that at least electronic degrees of freedom of the molecule should be intimately coupled with the collective charge density oscillations of the nanostructure. This might be key to resolving the observed soft polarization dependence, the resolution of which requires a complete treatment of fields and tensor elements of the polarizability, which we take up in the following chapter.

1.7 References

(1) Kneipp, K.; Wang, Y.; Kneipp, H.; Perelman, L.; Itzkan, I.; Dasari, R.; Feld, M. Single Molecule Detection Using Surface-Enhanced Raman Scattering (SERS). *Phys. Rev. Lett.* **1997**, *78*, 1667–1670.

(2) Nie, S.; Emory, S. R. Probing Single Molecules and Single Nanoparticles by Surface-Enhanced Raman Scattering. *Science (80-.).* **1997**, *275*, 1102–1106.

(3) Michaels, A. M.; Brus, L. E. Ag Nanocrystal Junctions as the Site for Surface-Enhanced Raman Scattering of Single Rhodamine 6G Molecules. *J. Phys. Chem. B* **2000**, *104*, 11965–11971.

(4) Moskovits, M. Surface-Enhanced Raman Spectroscopy: A Brief Retrospective. *J.of Raman Spectrosc.* **2005**, *36*, 485–496.

(5) Jeanmaire, D. L.; Duyne, R. P. Van. Surface Enhanced Raman Spectroelectrochemistry. *J. Electroanal. Chem.* **1977**, *84*, 1–20.

(6) Albrecht, M. G.; Creighton, J. A. Anomalously Intense Raman Spectra of Pyridine at a Silver Electrode. *J. Am. Chem. Soc.* **1977**, *99*, 5215–5217.

(7) *Surface-Enhanced Raman Scattering: Physics and Applications*; Kneipp, K.; Moskovits, M.; Kneipp, H., Eds.; Springer: Heidelberg, 2010; p. 482.

(8) Kim, H.; Kosuda, K. M.; Van Duyne, R. P.; Stair, P. C. Resonance Raman and Surface- and Tip-Enhanced Raman Spectroscopy Methods to Study Solid Catalysts and Heterogeneous Catalytic Reactions. *Chem. Soc. Rev.* **2010**, *39*, 4820–4844.

(9) Le Ru, E. C.; Meyer, M.; Etchegoin, P. G. Proof of Single-Molecule Sensitivity in Surface Enhanced Raman Scattering (SERS) by Means of a Two-Analyte Technique. *J. Phys. Chem. B* **2006**, *110*, 1944–1948.

(10) Dieringer, J. A.; Lettan, R. B.; Scheidt, K. a; Van Duyne, R. P. A Frequency Domain Existence Proof of Single-Molecule Surface-Enhanced Raman Spectroscopy. *J. Am. Chem. Soc.* **2007**, *129*, 16249–16256.

(11) Kleinman, S. L.; Ringe, E.; Valley, N.; Wustholz, K. L.; Phillips, E.; Scheidt, K. a; Schatz, G. C.; Van Duyne, R. P. Single-Molecule Surface-Enhanced Raman Spectroscopy of Crystal Violet Isotopologues: Theory and Experiment. *J. Am. Chem. Soc.* **2011**, *133*, 4115–4122.

(12) Jiang, J.; Bosnick, K.; Maillard, M.; Brus, L. E. Single Molecule Raman Spectroscopy at the Junctions of Large Ag Nanocrystals. *J. Phys. Chem. B* **2003**, *107*, 9964–9972.

(13) Futamata, M.; Maruyama, Y.; Ishikawa, M. Critical Importance of the Junction in Touching Ag Particles for Single Molecule Sensitivity in SERS. *J. Mol. Struct.* **2005**, *735-736*, 75–84.

(14) Le Ru, E. C.; Etchegoin, P. G.; Meyer, M. Enhancement Factor Distribution around a Single Surface-Enhanced Raman Scattering Hot Spot and Its Relation to Single Molecule Detection. *J. Chem. Phys.* **2006**, *125*, 204701.

(15) Le Ru, E.; Etchegoin, P. G. Single-Molecule Surface-Enhanced Raman Spectroscopy. *Annu. Rev. Phys. Chem* **2012**, 1–23.

(16) Braun, G.; Pavel, I.; Morrill, A. R.; Seferos, D. S.; Bazan, G. C.; Reich, N. O.; Moskovits, M. Chemically Patterned Microspheres for Controlled Nanoparticle Assembly in the Construction of SERS Hot Spots. *J. Am. Chem. Soc.* **2007**, *129*, 7760–7761.

(17) Braun, G. B.; Lee, S. J.; Laurence, T.; Fera, N.; Fabris, L.; Bazan, G. C.; Moskovits, M.; Reich, N. O. Generalized Approach to SERS-Active Nanomaterials via Controlled Nanoparticle Linking , Polymer Encapsulation , and Small-Molecule Infusion. *J. Phys. Chem. C* **2009**, 13622–13629.

(18) Guarrotxena, N.; Ren, Y.; Mikhailovsky, A. Raman Response of Dithiolated Nanoparticle Linkers. *Langmuir* **2011**, *27*, 347–351.

(19) Whitmore, D.; El-khoury, P. Z.; Fabris, L.; Chu, P.; Bazan, G. C.; Potma, E. O.; Apkarian, V. A. High Sensitivity Surface-Enhanced Raman Scattering in Solution Using Engineered Silver Nanosphere Dimers. *J. Phys. Chem. C* **2011**, *115*, 15900–15907.

(20) Blackie, E. J.; Le Ru, E. C.; Etchegoin, P. G. Single-Molecule Surface-Enhanced Raman Spectroscopy of Nonresonant Molecules. *J. Am. Chem. Soc.* **2009**, *131*, 14466–14472.

(21) Sonntag, M. D.; Klingsporn, J. M.; Garibay, L. K.; Roberts, J. M.; Dieringer, J. A.; Seideman, T.; Scheidt, K. A.; Jensen, L.; Schatz, G. C.; Van Duyne, R. P. Single-Molecule Tip-Enhanced Raman Spectroscopy. *J. Phys. Chem. C* **2012**, *116*, 478–483.

(22) Asher, S. A. UV Resonance Raman Studies of Molecular Structure and Dynamics: Applications in Physical and Biophysical Chemistry. *Annu. Rev. Phys. Chem.* **1988**, *39*, 537–588.

(23) Gersten, J.; Nitzan, A. Electromagnetic Theory of Enhanced Raman Scattering by Molecules Adsorbed on Rough Surfaces. *J. Chem. Phys.* **1980**, *73*, 3023.

(24) Kerker, M.; Siiman, O.; Bumm, L. A. Surface Enhanced Raman Scattering (SERS) of Citrate Ion Adsorbed on Colloidal Silver. *Appl. Opt.* **1980**, *19*, 3253.

(25) García-Vidal, F.; Pendry, J. B. Collective Theory for Surface Enhanced Raman Scattering. *Phys. Rev. Lett.* **1996**, *77*, 1163–1166.

(26) Schatz, G. C.; Young, M. A.; Van Duyne, R. P. Electromagnetic Mechanism of SERS. In *Surface-Enhanced Raman Scattering: Physics and Applications*; Kneipp, K.; Moskovits, M.; Kneipp, H., Eds.; Springer: Heidelberg, 2010; pp. 19–46.

(27) Morton, S. M.; Jensen, L. Understanding the Molecule-Surface Chemical Coupling in SERS. *J. Am. Chem. Soc.* **2009**, *131*, 4090–4098.

(28) Hallock, A.; Redmond, P. L.; Brus, L. E. Optical Forces between Metallic Particles. *Proc. Natl. Acad. Sci.* **2005**, *102*, 1280–1284.

(29) Fernandez-Sanchez, J. M.; Montero, S. Gas Phase Raman Scattering Cross Sections of Benzene and Perdeuterated Benzene. *J. Chem. Phys.* **1989**, *90*, 2909–2914.

(30) Xu, H.; Aizpurua, J.; Kall, M.; Apell, P. Electromagnetic Contributions to Single-Molecule Sensitivity in Surface-Enhanced Raman Scattering. *Phys. Rev. E* **2000**, *62*, 4318–4324.

(31) Blanco, L.; García-Vidal, F. Spontaneous Light Emission in Complex Nanostructures. *Phys. Rev. B* **2004**, *69*, 1–12.

(32) Litz, J. P.; Camden, J. P.; Masiello, D. J. Spatial, Spectral and Coherence Maping of Single-Molecule Sers Active Hot Spots via the Discrete-Dipole Approximation. *J. Phys. Chem. Lett.* **2011**, *2*, 1695–1700.

(33) Chu, P.; Mills, D. Electromagnetic Response of Nanosphere Pairs: Collective Plasmon Resonances, Enhanced Fields, and Laser-Induced Forces. *Phys. Rev. B* **2008**, *77*, 1–10.

(34) Chu, P.; Mills, D. Laser-Induced Forces in Metallic Nanosystems: The Role of Plasmon Resonances. *Phys. Rev. Lett.* **2007**, *99*, 1–4.

(35) Kelly, K. L.; Coronado, E.; Zhao, L. L.; Schatz, G. C. The Optical Properties of Metal Nanoparticles: The Influence of Size, Shape, and Dielectric Environment. *J. Phys. Chem. B* **2003**, *107*, 668–677.

(36) Xu, H.; Kall, M. Surface-Plasmon-Enhanced Optical Forces in Silver Nanoaggregates. *Phys. Rev. Lett.* **2002**, *89*, 1–4.

(37) Zuloaga, J.; Prodan, E.; Nordlander, P. Quantum Description of the Plasmon Resonances of a Nanoparticle Dimer. *Nano Lett.* **2009**, *9*, 887–891.

(38) Song, P.; Nordlander, P.; Gao, S. Quantum Mechanical Study of the Coupling of Plasmon Excitations to Atomic-Scale Electron Transport. *J. Chem. Phys.* **2011**, *134*, 074701.

(39) Shim, S.; Stuart, C. M.; Mathies, R. a. Resonance Raman Cross-Sections and Vibronic Analysis of Rhodamine 6G from Broadband Stimulated Raman Spectroscopy. *ChemPhysChem* **2008**, *9*, 697–699.

(40) *Taking Non-Radiative (radiation Damping) Channels into Account through the Rate Knr, the Branching between RR and Fluorescence Is Determined by IRR/IF = (kr+knr)/ Although Non-Radiative Channels Reduce the Overall Rate of Emission, They Favor the RR Branc*.

(41) Parkhill, J. A.; Rappoport, D.; Aspuru-Guzik, A. Modeling Coherent Anti-Stokes Raman Scattering with Time-Dependent Density Functional Theory: Vacuum and Surface Enhancement. *J. Phys. Chem. Lett.* **2011**, *2*, 1849–1854.

(42) Lang, X.-F.; Yin, P.-G.; You, T.-T.; Jiang, L.; Guo, L. A DFT Investigation of Surface-Enhanced Raman Scattering of Adenine and 2'-Deoxyadenosine 5'-Monophosphate on Ag20 Nanoclusters. *ChemPhysChem* **2011**, *12*, 2468–2475.

(43) Silverstein, D. W.; Jensen, L. Assessment of the Accuracy of Long-Range Corrected Functionals for Describing the Electronic and Optical Properties of Silver Clusters. *J. Chem. Phys.* **2010**, *132*, 194302.

(44) Frisch, M. J. et. al. *GAUSSIAN 09,Revision A.01*; Gaussian Inc.: Wallingford, CT, 2009.

(45) Becke, A. D. Density-Functional Thermochemistry. III. The Role of Exact Exchange. *J. Chem. Phys.* **1993**, *98*, 5648–5652.

(46) Schafer, A.; Huber, C.; Ahlrichs, R. Fully Optimized Contracted Gaussian Basis Sets of Triple Zeta Valence Quality for Atoms Li to Kr. *J. Chem. Phys.* **1994**, *100*, 5829–5835.

(47) Perdew, J. P.; Ernzerhof, M.; Burke, K. Rationale for Mixing Exact Exchange with Density Functional Approximations. *J. Chem. Phys.* **1996**, *105*, 9982–9985.

(48) Yanai, T.; Tew, D. P.; Handy, N. C. A New Hybrid Exchange-Correlation Functional Using the Coulomb-Attenuating Method (CAM-B3LYP). *Chem. Phys. Lett.* **2004**, *393*, 51–57.

(49) Zhao, Y.; Truhlar, D. G. Density Functional for Spectroscopy: No Long-Range Self-Interaction Error, Good Performance for Rydberg and Charge-Transfer States, and Better Performance on Average than B3LYP for Ground States. *J. Phys. Chem. A* **2006**, *110*, 13126–13130.

(50) Zhao, L.; Jensen, L.; Schatz, G. C. Pyridine-Ag 20 Cluster : A Model System for Studying Surface-Enhanced Raman Scattering. *J. Am. Chem. Soc.* **2006**, *128*, 2911–2919.

(51) Jensen, F. *Introduction to Computational Chemistry*; 2nd ed.; Wiley: Chichester, England, 2007.

(52) Ruud, K.; Helgaker, T.; Bour, P. Gauge-Origin Independent Density-Functional Theory Calculations of Vibrational Raman Optical Activity. *J. Phys. Chem. A* **2002**, *106*, 7448–7455.

(53) Kitahama, Y.; Tanaka, Y.; Itoh, T.; Ozaki, Y. Wavelength-Dependent Surface-Enhanced Resonance Raman Scattering by Excitation of a Transverse Localized Surface Plasmon. *J. Chem. Phys. C* **2009**, *113*, 11877–11883.

(54) Shegai, T.; Li, Z.; Dadosh, T.; Zhang, Z.; Xu, H.; Haran, G. Managing Light Polarization via Plasmon-Molecule Interactions within an Asymmetric Metal Nanoparticle Trimer. *Proc. Natl. Acad. Sci.* **2008**, *105*, 16448–16453.

(55) Li, W.; Camargo, P. H. C.; Lu, X.; Xia, Y. Dimers of Silver Nanospheres: Facile Synthesis and Their Use as Hot Spots for Surface-Enhanced Raman Scattering. *Nano Lett.* **2009**, *9*, 485–490.

(56) All the Simulations Reported in This Document Are Carried out Using COMSOL 4.2.

(57) Johnson, P. B.; Christy, R. W. Optical Constants of the Noble Material. *Phys. Rev. B* **1972**, *1318*.

(58) Zabala, N.; Perez-Gonzalez, O.; Nordlander, P.; Aizpurua, J. Coupling of Nanoparticle Plasmons with Molecular Linkers. *Proc. SPIE* **2011**, *8096*, 80961L – 80961L – 7.

(59) Hao, E.; Schatz, G. C. Electromagnetic Fields around Silver Nanoparticles and Dimers. *J. Chem. Phys.* **2004**, *120*, 357–366.

(60) Novotny, L.; Hecht, B. *Principles of Nano-Optics*; 1st ed.; Cambridge University Press: New York, 2011.

(61) Letnes, P.; Simonsen, I.; Mills, D. Substrate Influence on the Plasmonic Response of Clusters of Spherical Nanoparticles. *Phys. Rev. B* **2011**, *83*, 1–11.

(62) Gui, J. Y.; Stern, D. A.; Frank, D. G.; Lu, F.; Zapien, D. C.; Hubbard, A. T. Adsorption and Surface Structural Chemistry of Thiophenol, Benzyl Mercaptan, and Alkyl Mercaptans. Comparative Studies at Ag (111) and Pt (111) Electrodes by Means of Auger Spectroscopy,

Electron Energy Loss Spectroscopy, Low-Energy Electron Diffraction, . *Langmuir* **1991**, *7*, 955–963.

(63) Saikin, S. K.; Olivares-Amaya, R.; Rappoport, D.; Stopa, M.; Aspuru-Guzik, A. On the Chemical Bonding Effects in the Raman Response: Benzenethiol Adsorbed on Silver Clusters. *Phys. Chem. Chem. Phys.* **2009**, *11*, 9401–9411.

CHAPTER 2:

Surface enhanced Raman trajectories on a nano-dumbbell: Transition from field to charge transfer plasmons as the spheres fuse

2.1 Abstract

By taking advantage of the tensor nature of surface enhanced Raman scattering (SERS), we track trajectories of the linker molecule and a CO molecule chemisorbed at the hot spot of a nano-dumbbell consisting of dibenzyl-dithio-linked silver nanospheres. The linear Stark shift of CO serves as an absolute gauge of the local field while the polyatomic spectra characterize the vector components of the local field. We identify surface enhanced Raman optical activity due to a transient asperity in the nano-junction in an otherwise uneventful SERS trajectory. During fusion of the spheres we observe sequential evolution of the enhanced spectra from dipole-coupled Raman, to quadrupole- and magnetic dipole-coupled Raman, followed by a transition from line-spectra to band-spectra, and the full reversal of the sequence. Gauging by the spectrum of CO, the sequence can be understood to track the evolution of the junction plasmon resonance from dipolar to quadrupolar to charge-transfer as a function of inter-sphere separation, which evolves at a speed of ~1Å/min. The cross-over to the conduction limit is marked by the transition of line-spectra to Stark-broadened and shifted band-spectra. As the junction closes on CO, the local field reaches 1 V/Å, limited to a current of 1 electron per vibrational cycle passing through the molecule, with associated Raman enhancement factor *via* the charge transfer plasmon resonance of 10^{12}. The local field identifies that a sharp protrusion is responsible for room-temperature chemisorption of CO on silver. The asymmetric photo-tunneling junction, Ag-CO-

Ag, driven by the frequency tunable charge transfer plasmon of the dumbbell antenna, combines the design elements of an ideal rectifying photo-collector.

2.2 Introduction

Raman spectroscopy of single molecules is accessible at junctions of metallic nanostructures, where local fields are dramatically enhanced by the plasmonic response.[1] Since Raman scattering is a tensor quantity and local fields of nano-junctions are inhomogeneous on molecular length scales, given knowledge of the local field, spectra should be sufficient to track the location and orientation of molecules in 3D space. Alternatively, given knowledge of the molecular polarizability tensor, spectra should be sufficient to determine the local vector field. We implement this proposition through measurements on the prototypical junction formed between two metallic nano-spheres.[2–5] A chemically engineered nano-dumbbell consisting of dibenzyl-dithio-linked silver spheres (~ 30 nm diameter) serves as our experimental platform, with all evidence indicating that we are tracking single molecules.[6,7] Two illustrative spectral sequences will be presented: An uneventful sequence, which highlights optical activity of the junction and the spectral sensitivity to orientation that can be attained. A more eventful trajectory is recorded during the fusion of the nano-spheres. The sequence identifies line-spectra due to surface enhanced dipole-quadrupole Raman (SEQRS), surface enhanced dipole-magnetic dipole Raman (SEMRS),[8] and band-spectra when the junction gap reaches the conductivity limit of plasmons.[9–13] In good agreement with recent quantum analysis,[12,13] as the junction gap closes, we see the progressive tuning of plasmon resonances from the bonding dipole plasmon (BDP) to the bonding quadrupole plasmon (BQP), to the charge transfer plasmon (CTP). The latter is most clearly illustrated through SERS of an unintentionally chemisorbed CO molecule at the hot spot.

Our analysis clarifies continuua (band-spectra) that commonly appear in SERS arise from CTP resonances. The observations of magnetic and quadrupolar Raman spectra confirm surface enhanced Raman optical activity (SEROA),[14] which although reported[15–17] has been contested on general grounds.[18] The process can be driven by multipolar fields, which arise when nanometric asperities decorate the junction. The single molecule nature of the measurements leads to the compelling mechanistic assignments of SERS.

In standard implementations of Raman spectroscopy on molecular ensembles, orientational averaging contracts the observables to intensities and depolarization ratios of vibrational modes.[19] Moreover, the appropriate long-wave limit ($\langle r \rangle / \lambda \sim 10^{-3}$-$10^{-4}$, where r is the molecular length scale and λ is the wavelength of light) implies that only the local response to field amplitudes determines scattering matrix elements. For single molecules immobilized on the time scale of detection, the full tensor nature of the scattering process comes to force. The intensity of a given vibrational mode is now dictated by the orientation of the molecule relative to the vector field. Moreover, since local fields at nano-junctions vary on nm-scale, $\langle r \rangle / \lambda \sim 1$, the response is nonlocal.[20] Therefore, a multipolar expansion of the molecular response and local fields is necessary to interpret spectra. Where either the junction or molecule is not stationary, spectra fluctuate, as extensively catalogued ever since the earliest single molecule SERS measurements.[21] We equate fluctuating spectra to single molecule trajectories tracked through far-field measurements akin to global positioning with local antennae. The pre-requisites for such tracking are: a) knowledge of local fields, which in the classical limit can be reliably obtained through finite element analysis, b) knowledge of the molecular polarizability tensor and enhancement factors that may go beyond physical mechanisms.[22,23] The limitations of these idealizations become clear in the joint SERS and atomic force microscopy (AFM) measurements

on single dumbbells that we report. We will find that the structure on finer scale than resolvable through AFM controls the photo-physics; moreover, we will find that such structures evolve during irradiation of the junction. As expected, classical fields are inadequate to describe junctions with gaps < 5 Å, and in the conductivity limit where Raman reduces to photo-current scattering on the molecule, reformulation of the observables is necessary.

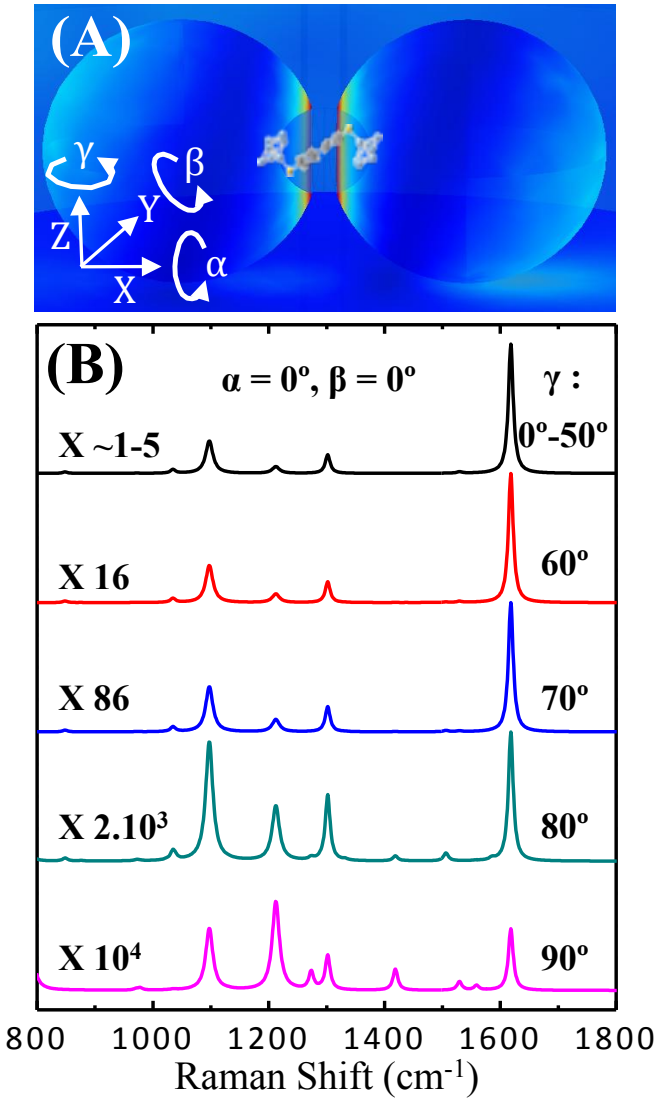

Figure 2.1. A) The geometry of dumbbell and the coordinate system used. B) Raman spectra as a function of rotation angle *γ*, along the *z*-axis, assuming a single enhanced field along the *x*-axis.

2.3 The framework for interpretations

In the effective medium framework, the dumbbell antenna is considered to be a polarizable medium in which the molecule is embedded. In the dipole-coupling limit, the scattering tensor that controls the SERS intensity is:

$$\{S_n^2\} = \sum_n \left| \boldsymbol{\varepsilon}_S^* \boldsymbol{P^T \beta' R^T \alpha'}_n \boldsymbol{R \beta P \varepsilon}_i \right|^2 = \sum_n \left| \boldsymbol{E}_S^L \boldsymbol{\alpha'}_n(\Omega) \boldsymbol{E}_i^L \right|^2 \quad 2.1$$

$\boldsymbol{E}_{i,S}^L$ are the enhanced local fields along incidence and scattering directions, $\boldsymbol{\alpha'}$ is the $3\times3\times n$ tensor of polarizability derivatives for the n-observable vibrations, and $\Omega=\{\alpha,\beta,\gamma\}$ are the Euler angles that determine the molecular orientation relative to the local fields defined on the dumbbell frame, described by the $\boldsymbol{R}$ rotation matrices; $\boldsymbol{\beta}$ is the matrix of enhancement factors along the principle axes of the dumbbell, $\boldsymbol{P}$ is a 2×3 projector that transforms the transverse polarization components of the far-field, $\hat{\boldsymbol{\varepsilon}}_{i,S}$, to the image plane. This projection is necessitated because we use high NA objectives, which generate and collect longitudinal field components with phase shift that varies across the focal plane.[24] The essential physics is contained in the $\boldsymbol{\alpha'}$, $\boldsymbol{\beta}$ and $\boldsymbol{\beta'}$ matrices. The polarizability derivative ellipsoid determines the angular resolution of the measurement. Because of the large polarizability associated with π-conjugated electrons, the DBDT ellipsoid is an elongated cylinder: for all observable modes, $\alpha'_{xx} >> \alpha'_{yy}, \alpha'_{zz}, \alpha'_{ij(i\neq j)}$, where x defines the long axis of the molecule (see fig.1). As a result, for a large cone around coaxial alignment of molecule and single applied field, the spectra are indistinguishable. This is illustrated in Figure 1 for a dumbbell irradiated with light polarized along its long axis. Distinct spectra appear when the relative tilt between principle axes exceeds φ = 60°, with concomitant drop in intensity. Since the linker is chemically bonded, large angle excursions will be accompanied by contraction of the junction gap, which may compensate for variations in orientation dependent intensity. As such, consistent time histories of spectral intensities contain

important information. Our strategy will be to match experimentally observed spectra, to then infer the local fields.

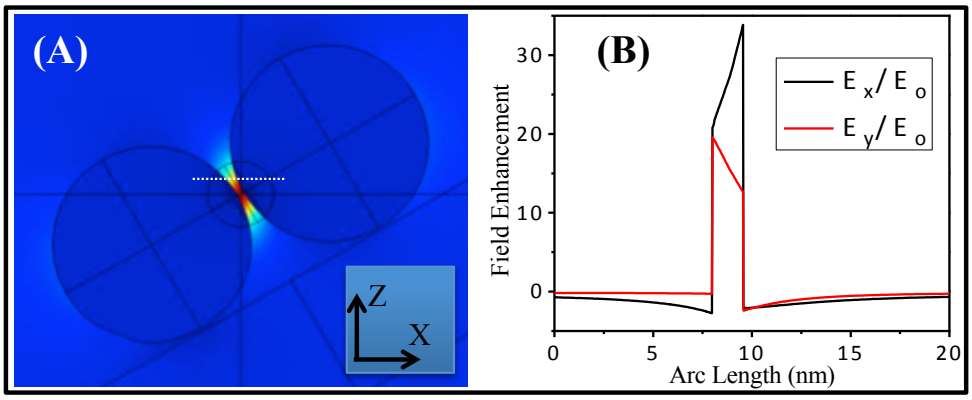

Figure 2.2. A) Local fields in the idealized dumbbell junction, for dumbbell tilted at 45° relative to the propagation direction (*z*) of the excitation laser. B) Electric field profiles at the nano-junction along the dotted line in (A) show that the local field and field gradient are comparable.

The local fields are displacements given by the sum of applied field and induced polarization: $D = E^0 + 4\pi P$. In the effective polarizable medium, the E^4 law of SERS enhancement factors (EF) becomes:[25]

$$EF = \left|\frac{D(\upsilon_s)}{E^0}\right|^2 \left|\frac{D(\upsilon_i)}{E^0}\right|^2 \qquad 2.2$$

The elements of the β matrices determine the vector components of enhancements:

$$\beta_{ji} = \frac{D_{ji}(\upsilon_i)}{|E^0|} = \delta_{ji}(\upsilon_i) + \chi_{ji}(\upsilon_i)\hat{\varepsilon}_i \qquad 2.3a$$

$$\beta'_{js} = \frac{D_{js}(\upsilon_s)}{|E^0|} = \chi_{js}(\upsilon_s)\hat{\varepsilon}_s \qquad 2.3b$$

They represent the dielectric response of the dumbbell, in terms of spectral susceptibilities, $\chi_{j\sigma}(\upsilon)$. Where appropriate, we rely on numerically computed local fields using FDTD

methods.[26] This classical treatment, assumption of linear response, and idealized junction geometries serve only as guides. For junction gaps < 5 Å, classical electrodynamics fails.[27] Moreover, the assumption of perfect spheres will prove inadequate. Variations in morphology of the junction can dominate observables.[28,29] A gainful strategy is to initiate a spectral search with local field components based on model considerations, and then carry out an exhaustive search of the Euler space. We compute spectral intensities:

$$I_n(\upsilon) \propto (\upsilon_i - \upsilon_n)^3 \upsilon_n^{-1} g f(T) S_n^2 \tag{2.4}$$

and compare them to intensity normalized spectra: $\sum_n I_n = 1$. A faithful reproduction of the observed spectrum determines the vector field experienced by the molecule, described by the field density matrix:

$$\rho(E) = |R(\Omega)\varepsilon_i\rangle\langle\varepsilon_s R(\Omega)| \tag{2.5}$$

which defines the spectrum: $S_n = Tr[\alpha_n' \rho(E)]$.

We will find that eqn. 1 is not sufficient to understand many of the spectra. Both quadrupolar and magnetic dipole Raman scattering, which can be driven by gradients of the enhanced local field,[30] will appear. Even for the idealized dumbbell depicted in fig. 2.2, the displacement (local field) and its linear dispersion are comparable at the hot spot, $D \sim \langle r \rangle dD/dr$. Therefore, multipolar response cannot be dismissed. Expansion of the polarizability of the dumbbell to first order in spatial dispersion: [20]

$$P_i^{(1)}(\upsilon, r) = \frac{1}{4\pi}\left\{\left[\varepsilon_{ij}(\upsilon) - \delta_{ij}\right]E_j(\upsilon, r) + \Gamma_{ijn}^{(1)} \nabla_n E_j(\upsilon, r)\right\} \tag{2.6}$$

generates the electric dipole-magnetic dipole and electric dipole-electric quadrupole Raman scattering terms. Their squared matrix elements, to lowest order, are given by:

$$|\boldsymbol{S}|_m^2 = \boldsymbol{D_i^* R^T \alpha' R D_s \, D_s^* R^T G' R M_i} \tag{2.7}$$

$$|\boldsymbol{S}|_q^2 = \boldsymbol{D_i^* R^T \alpha' R D_s \, D_s^* R^T A R Q_i} \tag{2.8}$$

in ***G'***, ***A*** matrices contain the electric dipole-magnetic dipole $G'_{a,b} = < \mu_{e,a}\mu_{m,b} >$ and electric dipole-electric quadrupole $A_{a,bc} = < \mu_{e,a} q_{bc} >$matrix elements,[31] which we compute through the ROA module of Gaussian 09 suite.[32] In eqn. 7, $\boldsymbol{M}_i$ represents the incident magnetic field vector, $M_{ab}=D_a\partial D/b - D_b\partial D/a$ in eqn. 8, the incident quadrupole field vector, $\boldsymbol{Q}_i$, has six elements, three diagonal Q_{aa} and three cross terms $Q_{ab}=D_a\partial D/b + D_b\partial D/a$, which only differ from the magnetic terms by the relative phase between local fields. The matrix elements and their numerical evaluation are described in the literature.[33] We have considered a variety of structures to model DBDT attached to two silver spheres, and find polarizabilities calculated based on the Ag_7-S-DB-S-Ag_7 structure as an adequate representation of the experiments.[7] The polarizability tensor is computed for the optimized minimum energy structure, in which the staggered phenyl rings impose D_2 symmetry on the linker, rendering all of its normal modes to be formally Raman active. The list of the prominent lines, their symmetries, and the explicit transition matrix elements that leads to their observation are given in table 1, in the methods section. In the analysis, we only consider overall orientations of the molecule relative to the local field.

2.4 An uneventful trajectory – An asperity in the gap

In fig. 2.3 we show a sequence of 35 spectra, consecutively recorded on a single dumbbell, with 10 s acquisition time per spectrum. The set was recorded after identifying an isolated dumbbell with the AFM, and after aligning the polarization of the applied field along its long axis. The field enhancement along this axis dominates by more than a factor of 10 in the idealized dumbbell, therefore SERS along this direction should be enhanced by more than 10^4, rendering all other fields negligible. Indeed, the spectrum consisting of the five totally symmetric A-modes (1577 cm^{-1}, 1267 cm^{-1}, 1185 cm^{-1}, 1065 cm^{-1} and 994 cm^{-1}, see table 1) can be

reproduced assuming parallel incident and scattered local fields. This, in turn, determines the three Euler angles that define the orientation of the molecule relative to the field (see fig. 2.3b). Throughout the sequence, the molecule remains confined to the narrow volume in Euler space, $\Omega = \{\alpha,\beta,\gamma\} = \{90\pm20^{o}, 0^{o}, 20\pm10^{o}\}$. For the ~5 min duration of observation, the molecule behaves as expected for a chemically bound linker at the hot spot of the dumbbell.

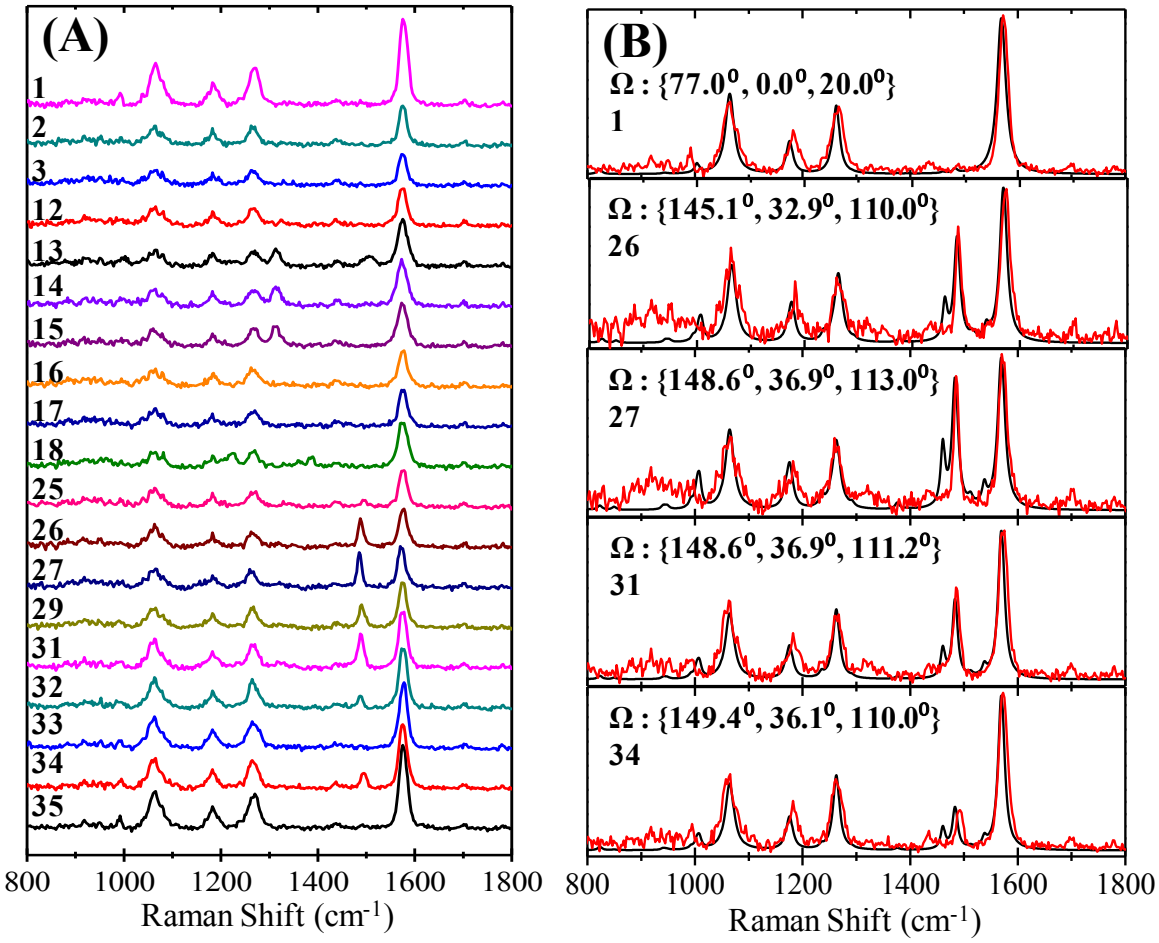

Figure 2.3. An uneventful trajectory. A) Spectra in a sequence of 35 consecutive acquisitions, with 10 s collection time per acquisition. The prominent spectrum is that of DBDT aligned along the long axis of the dumbbell (compare to Fig. 2.1). The main fluctuation is the highlighted line at 1495 cm^{-1}. B) The fluctuation can be reproduced assuming imaginary field components: $\hat{\varepsilon}_s$ = [1,0.2i,1], $\hat{\varepsilon}_i$ = [1,1,0.2i], and small variations in orientation. The extracted local field density is defined as $|\varepsilon_i R^T(\alpha,\beta,\gamma)><R(\alpha,\beta,\gamma)\varepsilon_s|$, at rotation angles indicated in the figure.

In addition to the normal linker spectrum we see two other lines, at 1496 cm^{-1} and at 1310 cm^{-1}, which appear and disappear uncorrelated in time. DBDT contains a symmetric H–C=C–H rocking mode associated with ring deformation at 1496 cm^{-1} (see table 1). The intensity of this transition is ~40 times weaker than the main lines when the molecule is aligned with the field. Under the assumption of a single enhanced field component, therefore parallel scattering, $\hat{\varepsilon}_i \cdot \hat{\varepsilon}_s = 1$, the observed spectrum cannot be reproduced for any orientation of the molecule. It can only be reproduced if we assume complex field components in both incident and scattered channels. The appearance and disappearance of the 1496 cm^{-1} peak, without changing intensities of the other lines or the overall intensity of the spectrum, can be accomplished with small reorientations of the molecule subject to the complex fields, E_i = [1, 0.2i, 1] and E_s = [1,1, 0.2i], as illustrated in fig. 2.3b. The spectral sensitivity to orientation is remarkable – the observed fluctuation can be accomplished by motion within a 5° cone. The essential ingredients of the observed fluctuation are: a) more than one active enhancement direction, b) optical activity admitted by the complex fields. Noting that the effect is transient (the spectrum reverts to linear, parallel SERS subject to one field component) and that the molecular orientation is preserved, the structure of the junction must have evolved. Although the vector field density see eqn. 5) is fully determined by the fit, there is not a trivial mapping to reconstruct a unique local structure. Nevertheless, a sense of the structural change can be obtained by decomposing the spectrum as a sum of parallel and perpendicular scattering: $\beta_{xx}^4 \left|\hat{\varepsilon}_x \alpha'(\Omega) \hat{\varepsilon}_x\right|^2 + \beta_{xy}^4 \left|\hat{\varepsilon}_y \alpha'(\Omega') \hat{\varepsilon}_x\right|^2$. The first term represents the linker oriented along the long axis of the dumbbell, while in the second term we find $\Omega' \cong \{0°, 70°, 5°\}$ and $\beta_{xy}/\beta_{xx} \sim 10$, *i.e.,* this scattering component is enhanced by a factor of 10 above that of the long-axis. Fields along two different directions and different field

strengths suggest the formation and disappearance of an asperity with a radius of curvature of $R' \sim R|\beta/\beta'| \sim 3nm$ and oriented along Ω' relative to the molecule.

We can eliminate several other possibilities. It is not likely that the fluctuation is due to the appearance of a second molecule(s). To observe perpendicular scattering, α'_{xy}, two enhanced fields are required, which is not equivalent to two different molecules and a single field. Also, the absence of correlation between this single line fluctuation and the rest of the spectrum would be difficult to rationalize for two independent scattering centers, $c_1I_1 + c_2I_2$, since in all lines there would have to be the conservation principle that $c_1+c_2 = 1$. We have considered the possibility that the fluctuation is an attempt by the molecule to walk, as seen for dithiols through scanning tunneling microscopy.[34] To this end, we have considered both homolytic and heterolytic cleavage of one S-Ag bond, to produce the radical Ag-S-DB-S or the anion Ag-S-DB-S$^-$. In the radical, the C=C ring modes split, while in the anion the entire peak red-shifts. Although many features are common to all three spectra, a satisfactory match cannot be obtained for one-sided linkage.

We cannot account for the 1310 cm^{-1} line in the present model. It appears to be a splitting of the in-plane C-H vibrations. In the staggered geometry, nearly degenerate modes of poorly coupled phenyl rings is to be expected. Upon twisting to co-planarity, these modes should split. This expectation was not borne out in computed spectra as a function of twist angle. Instead, we see shifts and splittings of vibrations that are coupled to the C-S-Ag motion (see table 1). The failure of the analysis to account for changes in vibrational frequency highlights the limitations of the analysis. Finally, there are minor spectral features that are unaccounted, which are extraneous to DBDT. The binder on the silver spheres and the polymer film on the slide are the most likely contributors. In addition to their smaller Raman cross sections, we reason that they

are not more prominent because of the synthetic strategy. For the spheres to be linked by a 1 nm-long molecule the facets must be relatively clear of other species.

2.5 As the spheres fuse

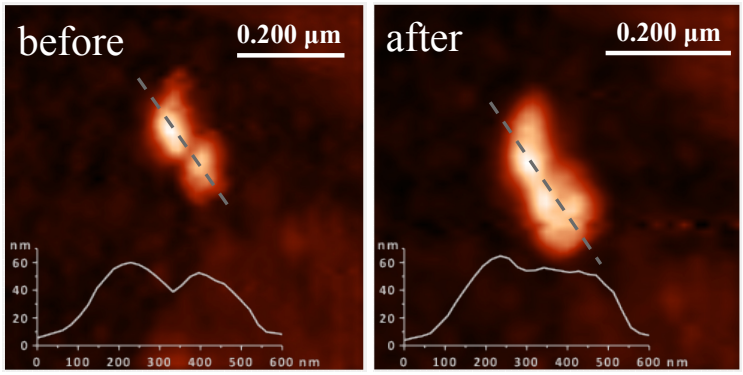

Figure 2.4. AFM images of the dumbbell before and after recording the SERS sequence. The resolution is sufficient to identify the isolated dumbbell and its principle axis for the purpose of aligning the polarization of the incident field. As the junction fuses during the measured sequence, the effective inter-sphere distance becomes negative.

We consider a sequence of SERS spectra recorded during the fusion of the nanospheres. The AFM images of the dumbbell before and immediately after recording the sequence are shown in fig. 2.4. The fusion is light induced,[35] initiated by the poor anchoring of the dumbbell in the PVA film. Otherwise, the irradiation intensity (~1 mW/µm^2) is the same as in the first sequence. The image plot of fig. 2.5 shows the consecutively recorded spectra, at 10 s acquisition per spectrum. Selected spectra are shown in figs. 5b and 6b. The contrast with the trajectory of fig. 2.3 is stark. Dramatic variations occur in overall intensity, in relative intensities, and a reversible transition from line-spectrum to banded-spectrum is observed. In addition to DBDT, a line appears at 2115 cm^{-1}, characteristic for atop chemisorption of CO on silver.[36–40] CO is most likely derived from the PVA film, analogous to demonstrations of irradiated carbon clusters on

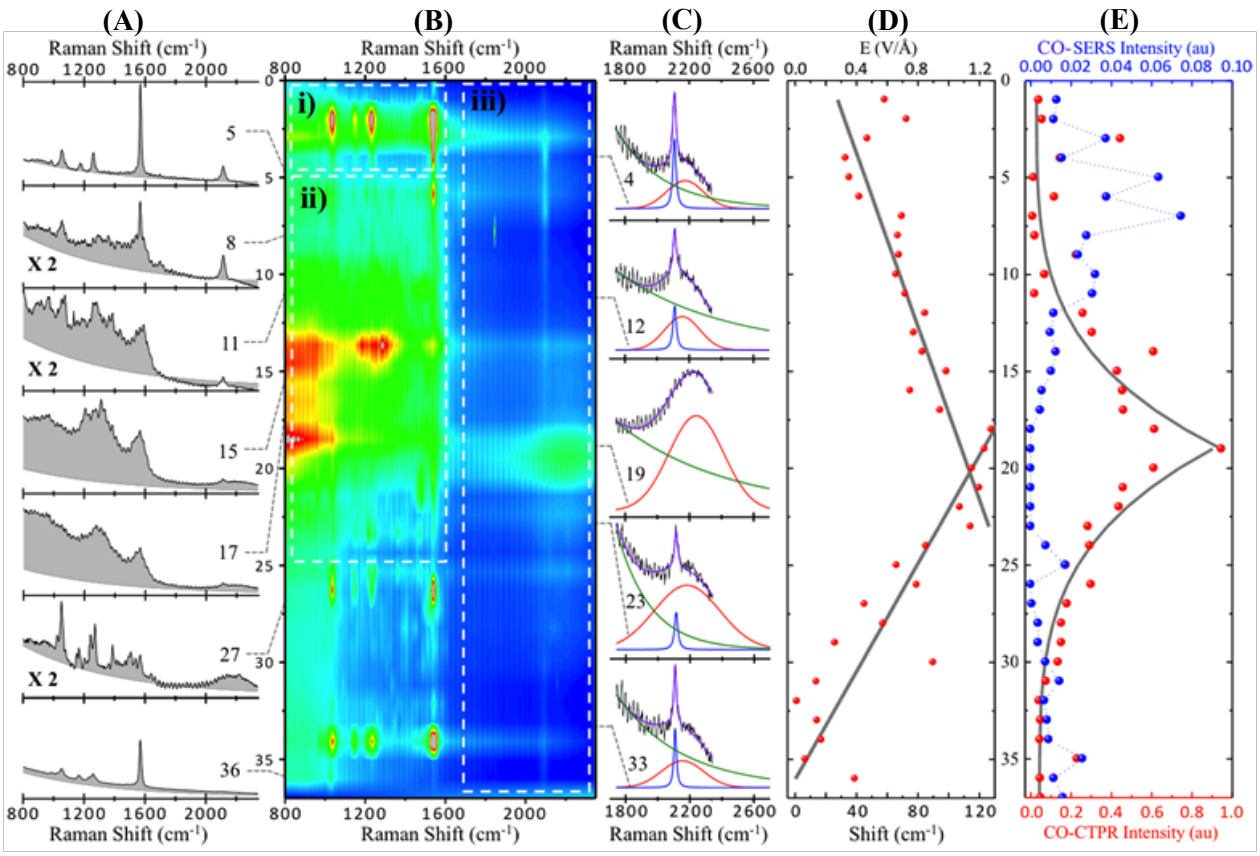

Figure 2.5. A) Image plot of a sequence of 36 SERS spectra recorded consecutively, during the fusion of the dumbbell. The white squares highlight: i) The 50-fold fluctuation in overall intensity of the normal SERS line-spectrum, ascribed to tuning across the BDP resonance by the closing junction, ii) The development of band-spectra and a dramatic increase in integrated intensity, assigned to the transition to the conductivity limit where current passing though the molecule leads to Stark shifting and broadening. c) The CO spectral region, which shows evolution that parallels but trails that of DBDT. B) Selected spectra from the image plot: #5 – SERS line-spectrum of DBDT and CO; #8 – onset of band-spectrum at the DBDT site while the normal SERS of CO is observed; #15 and #17 – the dominance of band-spectra at both sites, #27 – re-emergence of lines at the DBDT site, while CO remains in the CTP regime, #36 – the normal SERS line-spectrum of DBDT, the molecule is now outside the conductivity range of the spheres and appears unscathed by the fusion process. C) Decomposition of the CO spectrum into the normal SERS line at 2115 cm^{-1}

and the broad CTPR band with evolving band center. D) The sequential spectral shift of the CO charge transfer resonance (bottom abscissa), and the associated Stark field (top abscissa). The shift reaches a limiting value of ~100 cm^{-1}, which corresponds to 1 V/Å. E) The intensity of the normal CO SERS line (blue) and the CTPR band (red). Note the 10-fold difference in scales. The curves are the fourth power of the local field obtained from the spectral shift in (D).

roughened silver or gold where generation of CO at plasmonic hot-spots is seen.[41] At room temperature, CO only binds to unsaturated surface atoms of noble metals, as rigorously demonstrated through particle size dependent desorption measurements on gold.[42] We can be sure that CO is attached to an atomically sharp asperity in the junction, otherwise it would desorb. Moreover, once formed, we can be sure that the temperature at the CO site does not exceed ~350 K. Therefore, the fusion sequence we follow is not due to melting, but rather driven by the polarization forces at the hot-spot.[36] The vibrational frequency of CO is sensitive to its adsorption site; and interacting CO molecules, such as can be generated at high surface coverage, red-shift and develop a broad red band.[39] Here, a broad blue-shifted band appears with intensity anti-correlated to the normal SERS line of CO. We will assign the blue band, which shows the characteristic Stark shift of CO, to the charge transfer plasmon resonance (CTPR).

The assignable spectra of DBDT (fig. 2.6b) determine the trajectory of the molecule in Euler space (fig. 2.6a). The molecular orientation spans the full Euler space. The trajectory starts in the normal linker orientation (#1-5) and reaches the vertical plane bisecting the fusing nano-spheres (#28). In addition to normal Raman, in which all four field-interactions are dipole coupled (table 1 footnote), we see spectra in which one of the fields is either quadrupole (SEQRS) or magnetic dipole coupled (SEMRS). These appear before and after the broadening of lines seen in spectra #11-20 of the sequence (fig. 2.5). Searches of the Euler space establish that

the SEMRS is dominated by a magnetic field along the *z*-axis, while the SEQRS is due to the $q_{xx,}$ quadrupole. Both the intensities and directions of these scattering components are difficult to understand in terms of field gradients alone. For example, the SEQRS, which is dominated by two lines (fig. 2.6b), makes it clear that this is not a minor component of the overall scattering, but rather the only component. The switch from normal dipolar Raman to SEQRS can be understood as the tuning of field plasmon resonances. At junction gaps of $d \sim$ 1-2 Å, the dipolar plasmon shifts to the IR and the binding q_{xx} quadrupolar plasmon (BQP) comes into resonance with the excitation laser (2.3 eV).[12,13] Indeed, the entire spectral sequence is most consistentlyexplained by recognizing that plasmon resonances tune through the fixed excitation frequency as the spheres fuse and this determines the observable elements of the Raman tensor. This applies to both the DBDT and the CO spectra, as we expand below.

During the first 50 s sequence (fig. 2.5, #1-5), the intensity of the entire normal DBDT spectrum breathes by a factor of ~50. The implied fluctuation in the local field is a factor of $2.5 \sim 50^{1/4}$. During this episode, the spectrum is strictly the dipolar SERS (see #5 in fig. 2.5b). Since the linker starts at the hot-spot, aligned along the largest field, the increase in local field must be associated with the tuning of the plasmon resonance by contraction of the junction. This can be accomplished by the approaching crevice of fusing spheres. Thus, for 30 nm silver spheres separated by 1 nm, we calculate an enhancement factor of $\beta_{xx} = 40$. At the crevice of a fused pair of spheres, 1 nm removed from the contact point, we calculate $\beta_{xx} = 90$, which is reasonably consistent with the observed intensity fluctuation. The crevice must recede for the intensity to revert. Alternatively, and more consistent with the full history, the intensity fluctuation can be understood as the tuning-in of the bonding dipolar plasmon (BDP) resonance as the inter-sphere gap contracts. At 532 nm, the excitation is to the red of the dipolar plasmon resonance for perfect

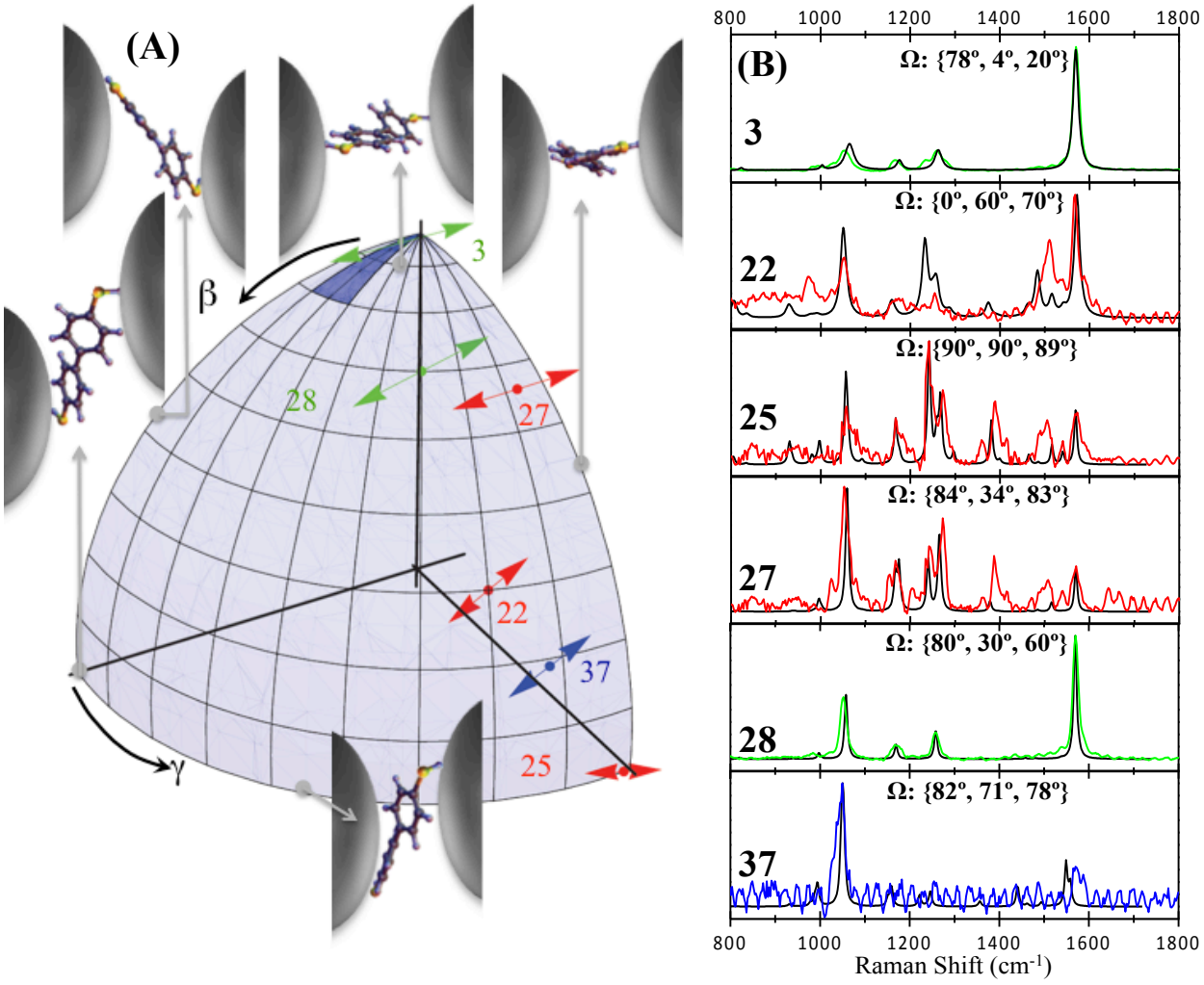

Figure 2.6. A) SERS trajectory in Euler space. The polar and azimuthal angles are relative to the dumbbell frame, while the orientation of the double-sided arrows indicates rotation of the molecular plane relative to its principle axis. Structures are shown at selected angle to visualize the molecule-junction orientation. Note, the full length of the molecule is 11Å, the orientations make it clear that the junction hovers between contact and ~ 5Å. The color code is matched with the spectral reproductions in Fig. 2.6B. (B) Spectral matches are color coded to identify the Raman scattering process as: dipolar (green), dipole-magnetic dipole (red), dipole-quadrupole (blue) at the indicated Euler angles.

silver spheres separated by 1 nm.[7] The resonance red-shifts as the gap closes.[12,13] Note, the AFM determined shape of the dumbbell after fusion is equivalent to a negative gap, *i.e.,* the shape corresponds to that of overlapping spheres. Accordingly, the sequence captures the cross-over region where the effective gap distance changes sign and the BDP resonance tunes down to zero-frequency. In the process, the BDP resonance must necessarily pass through 532 nm, and this would explain the fluctuation in overall intensity of the normal Raman spectrum.

The episode of overall intensity fluctuation is followed by the transition to band-spectra (#12-20) in which only the parentage of DBDT lines is apparent. The integrated intensity under the band-spectra is an order of magnitude larger than the most intense line-spectrum seen in the sequence. We associate the onset of band-spectra with the transition to the conductivity limit.[43] In this limit, the field plasmons are shorted by the current carrying CTP, Raman scattering is accompanied by photo-current passing through the molecule and vibrational resonances can be expected to broaden *via* inelastic electron scattering. Note, after embedding in the junction, the molecule reappears unscathed (#36), therefore the confining junction of the molecule re-opens. Characteristically, the multipolar Raman spectra appear at the transition from line-spectra to band-spectra. As the junction re-opens, we first see SEMRS (#22-25), then the normal Raman spectrum of the molecule in the vertical plane (#28), then the normal linker spectrum in the horizontal plane (#36), followed by the SEQRS (#37) before the molecule is lost from sight. The fusion sequence appears to track the tuning of plasmonic resonances. As the gap distance passes through zero and assumes effective negative values, the BDP, BQP and CTP resonances should scan sequentially through the excitation wavelength.[12,13] This nicely explains the sequence of dipolar Raman, multi-polar Raman, and band spectra (#1-20), and the reversal of the process in the same order (#20-36).

2.6 CO as a gauge of local fields

The above picture is re-enforced and quantified by the CO spectra, the evolution of which trails that of DBDT. The faint SERS of CO appears as the DBDT line-spectrum reaches its maximum intensity (#3), which we associated with the gap-tuned BDP resonance. The intensity of the CO line peaks (#4) and after fluctuating, it decays while its blue-shifted CTPR band grows. The anti-correlated history of the SERS line *vs.* CTPR band is quantified by decomposing the spectrum into two components (fig. 2.5c). The extracted peak shift of the CTPR and integrated intensities of SERS and CTPR are plotted in Fig. 2.5D,E. As the SERS intensity decays to zero, the CTPR intensity builds-up to its maximum value, to an integrated intensity that is an order of magnitude larger than that of the SERS line (see fig. 2.5e). The process reverses: the band intensity decays and the SERS line reappears. The CTPR band shifts linearly while its intensity grows exponentially, and both spectral shift and intensity reverse sign at the same time (fig. 2.5d, e). The sequence identifies the closing and re-opening of the junction at the CO site. The contact point is sharply defined in the case of CO, to be contrasted with the DBDT where the band-spectra evolve more gradually reflecting the contortions of the molecule (fig. 2.6a) as the gap closes.

The CTP resonance is consistent with its assignment to SERS when current is passing through the molecule. Since CO is subject to a first order Stark shift of 10^2 cm^{-1} $(V/Å)^{-1}$,[44,45] we can deduce the local field experienced by it. The peak shift indicates a DC field, while the peak width (300 ± 50 cm^{-1} throughout) should be determined by the combination of AC Stark shift and dephasing. Since the junction is asymmetric, due to one-sided chemisorption of CO, it should lead to rectification of the optical field.[46] The peak shift is used to construct the secondary axis in fig. 2.5d. The field reaches a limiting value of 1.1 V/Å, therefore a chemical potential

across the 1.1 Å bond length of CO of 1.2 eV. As a single channel conductor, the current passing through the molecule would be subject to the quantum of conductance $G_0 = 2e^2/h = 7\times10^{-5}\ \Omega^{-1}$. Consistent with this, the limiting current $J = VG_0 = 0.07$ mA, which equals 4×10^{14} e^-/s, corresponds to the transfer of one electron per vibrational cycle of CO: $\omega = 3.95\times10^{14}$ cycles/s (2100 cm^{-1}). While the spectral shift is linear with time, the accompanying intensity of the CTPR is highly nonlinear, and holds important clues to the nature of the enhanced scattering process. Identifying the Raman scattering intensity with the transition current $I \sim E_L^4 \langle u\omega \rangle^4 \sim E_L^4 \langle J \rangle^4$, we may expect it to evolve at least with the fourth power of the local field, which is indicated in Fig. 2.5E. This ignores the field dependence of the current, $\langle J \rangle$, which if associated with photo-field induced tunneling then an exponential dependence on junction gap and field would be expected. Indeed, the observed intensity dependence can be better fit to an exponential. Closer inspection of the intensity shows a symmetric staircase about the peak, suggestive of quantized conductance channels as seen in break-junctions.[47] The conductance should be determined by the number of contacts between silver atoms during the closing of the junction. In contrast with the field measured by the vibrational shift, which gauges current through the CO bond, the intensity should be determined by the photo-current sustained across the entire fusing junction. An asymmetric metal-insulator-metal photo-tunnel junction, Ag-CO-Ag, corresponds to a rectifying photodiode.[46,48] The plasmonic nature of the junction endows it with a frequency tunable antenna,[49] completing the design elements for the ideal photo-collector.[49] We will expand on this important tangent elsewhere; here, we focus on the spectral analysis of light scattering processes.

The determination of the local field by the Stark shift allows a direct measure of SERS enhancement factors. Given the irradiation intensity of 1 mW/μm^2 (8.6X10^{-4} V/Å), to reach 1 V/Å, the field must be enhanced by $E/E_0 = 1.1\times10^3$, with associated Raman enhancement factor

in excess of $EF = (E/E_0)^4 = 10^{12}$. Such enhancement is necessary to see a single CO molecule in SERS given its Raman cross section of 3.3×10^{-31} cm^2/sr,[50] which is nearly three orders of magnitude smaller than that of DBDT. Evidently, within the same nano-junction the local field experienced by CO is nearly 10 times larger than by DBDT: CO must be chemisorbed on an atomically terminated sharp protrusion, which we deduced based on the requirement for chemisorption at room temperature.[42] Previously, ensemble measurements of SERS of CO have been used to associate spectra with local structure.[41] The large enhancements we ascribe to a protrusion within the hot spot of the dumbbell is contained in the fractal structures considered in the interpretation of SERS on colloidal preparations.[51]

The field-induced blue-shift of the CO band is informative. The Stark shift of CO chemisorbed on metals has been analyzed.[52,53] The blue-shift arises at positive applied potentials, as a combination of electrostatic shift and reduction of π^* back-donation from the metal *d*-electrons. The shift suggests a net depletion of back-donated electrons during the CTP excitation, which involves electrons near the Fermi edge.[54,55] Given the short dephasing time of the CTP, the observed linewidth should be determined by non-adiabatic evolution on the ground vibronic state, common to damping of molecular vibrations on metal surfaces.[56,57] The contrast between SERS and CTPR is significant. Based on the 30 cm^{-1} width of the normal SERS line, the observed vibrational dephasing time of CO is 1.1 ps, in line with prior measurements[58,59] and typical for CO chemisorbed on metal surfaces.[60] The dephasing time of the CTPR band is 100 fs, on the time scale of electron-phonon scattering in metals. The contrast seems less dramatic if we consider vibrational dephasing by the local density of electrons, $1/\tau = \pi\omega(\delta n)^2/2$, where δn is the fluctuation in the number of back-donated *d*-π^* electrons:[56] δn = 0.02 would explain the normal SERS line, while the CTPR lifetime would suggest a threefold increase: δn = 0.06

electrons. This may be a reflection of the fact that *d*-electrons in silver are deeply buried,[40] while the current in CTP is principally carried by the *sp* electrons at the Fermi edge[12] with the π^* orbital of CO acting as a conductive bridge.

2.7 Conclusions

Consistent with our prior analysis, the presented SERS trajectories suggest that we are observing a single molecule on a single nano-dumbbell. The trajectories illustrate the concept of tracking a single molecule in 3D space, in the inhomogeneous local field of a nanojunction. The motions we follow are sluggish, matched with the data collection time of a frame per 10 s. Principally, they involve the restructuring of the junction. We have seen the appearance and disappearance of an asperity nearby the molecule, a process that leads to surface enhanced Raman optical activity – linearly polarized excitation leads to elliptic excitation and scattering due to sub-structure of the junction. This underscores the challenge in interpreting polarization dependent SERS measurements.[7,61]

The fusion sequence interrogates the full range of plasmonic activity at a nano-junction and the evolution of spectral response during the field to current transition of the junction plasmon. The principle motion in this sequence is the closing and re-opening of the gap, at the gentle pace of ~ 1 Å/min. The gap, which may not exceed the S-S separation of the linker of 11 Å, can be gauged by the Euler-space trajectory of the molecule (fig. 2.6). At contact with CO, the physical gap would be limited by its bond-length of 1.1 Å. However, the effective inter-sphere distance assumes negative values as the neck of the junction widens. In the process we observe the sequential evolution of the Raman spectra of the linker from dipolar SERS, to SEQRS and SEMRS, to intense band-spectra, tracking the predicted spectral evolution of the dumbbell

plasmon from BDP, to BQP, to CTP as a function of gap distance. The assigned multipolar spectra identify some of the origins of fluctuations and blinking seen in single molecule SERS. We identify the cross-over to the conduction limit as the transition from line- to band-spectra. In the case of CO, the normal SERS line converts to a broad blue-shifted band, subject to first-order Stark-effect. The spectral shifts of the bands in DBDT are smaller and typically red shaded. In the absence of a permanent dipole, DBDT is subject to second order Stark shift, $\Delta\upsilon \propto \alpha' E^2/2$, therefore mode specific and quadratic in the field. This provides an explanation for some of the continua observed in SERS, the origin of which has been extensively deliberated.[62–64] The CTPR continua are distinct from broadened Rayleigh, in which electron-hole pair excitation of the metal leads to scattering on defects and surface states, and leads to a tail originating at the excitation origin.[65] Mechanistically, the CTPR continua fit the model of ballistic electron-hole scattering on interfacial molecules.[66] The compelling assignments of spectra and mechanisms in the present derive from the engineered nano-structure and the requirement of consistency of histories imposed by single-molecule trajectories. The same applies to the observation of CO chemisorption on an asperity, which otherwise is difficult to recognize in ensemble measurements. We expect quantitative treatments of these prototypical systems to be possible with the development of its essential ingredients: coupled molecule-plasmon dynamics and light scattering in current carrying junctions.[67] Beside fundamental motivations, it may be recognized that CTPR in an asymmetric photo-tunneling junction combines the ideal design elements of a photo-voltaic cell.[68]

2.8 Methods

2.8.1 Experimental

The synthetic strategy to prepare the nano-dumbbells has been reported previously.[69] Briefly, a colloidal suspension of 35±5 nm citrate capped silver nano-spheres is prepared with a narrow size distribution. The citrate is then exchanged with bis(p-sulfonatophenyl) phenylphosphine, which serves as a protective capping agent. A 1mM DBDT solution is added to the suspension, allowed to sit for ~3 hrs, followed by centrifugation. The resulting solution consists of ~50% nano-sphere dimers, which is characterized by transmission electron microscopy. The strategy ensures that the linker is at the hot-spot of the nanosphere dimer, but does not guarantee that the dumbbell is assembled by one linker alone.

Joint AFM/Raman measurements are carried out under ambient conditions, on dry mounted dumbbells prepared by spin-coating or drop casting a ~5 pM solution on a 150 micron-thick microscope slide.[7] A dilute solution of polyvinyl alcohol (PVA) is added to the aqueous suspension prior to coating, and the slides are either pre-heated or heat cycled on a hot plate after preparation. The polymer film provides the mechanical stability required for AFM imaging, and serves as the essential heat sink for thermal stability. The AFM resolution is limited. It serves to identify dumbbells that are isolated in the field of view of the high NA objective, and serves to identify the orientation of the dumbbell to align the polarization of the laser with a half-wave plate. The excitation source is a continuous wave, single mode laser operating at λ = 532 nm. A 1.25 NA oil immersion lens is used to focus the laser on the sample, and to collect the backscattered Raman light through a pair of notch filters (Semrock, 1:10^6 extinction). The spatially filtered scattered light is spectrally dispersed in a 0.25-m monochromator and recorded on a CCD array (Andor, V401-BV). The effective instrument resolution is 10 cm^{-1}.

2.8.2 Computational

Calculations were performed using the methodologies implemented in Gaussian 09. The system is modeled as DBDT attached to seven silver atoms on either side: Ag_7-S-DB-S-Ag_7. Unconstrained geometry optimization was performed using the B3LYP functional.[70] The final calculations employ the def2-TZVP basis set[71] with matching pseudopotentials for silver (> 1000 basis functions). The optimized structures are verified to not have imaginary vibrational frequencies. The polarizability tensors are obtained using the ROA module in Gaussian 09. In the relaxed geometry, the phenyl groups of DBDT are staggered. The symmetry of the linker (ignoring silver atoms) is reduced to D_2, therefore all 60 of its normal modes are formally Raman active. In Table 1 we list the prominent lines observed in the spectra, their symmetry classification in D_2, and the matrix elements of the transitions observed. Note, inclusion of the silver atoms into consideration (a total of 102 normal modes are computed), further reduces the symmetry to C_s. Accordingly, modes that entail significant C-S-Ag motion (indicated by * in table 2.1) cannot be classified under D_2 and are sensitive to the assumed chemisorption model.

Table 2.1. Observed and Calculated (B3LYP/def2-TZVP) Vibrational Frequencies and their Assignments

Mode	Frequency (cm^{-1})		Assignments		
#	calculated[a]	experimental	transition[b]	$\Gamma(D_2)$[c]	description
93	1580	1579	R_{xx}, M_{yy}	A	aromatic C=C stretch coupled to C-C stretch
92	1547	1548	$Q_{z,xy}$	B_z	ring deformation
91	1521	1516	M_{xz}	B_y	ring deformation
90	1492	1493	R_{xx}, M_{xx}	A	HC=CH rock coupled to ring deformation
88	1388	1380	M_{xy}	B_z	HC=CH scissor
86	1300	1298	M_{xy}	B_z	HC=CH rock
84	1271	1267	$[R_{yy}/M_{xz}]$ *	$[A/B_y]$*	C-C stretch combined to C-S-Ag motion
83	1243	1242	M_{xy}	B_z	aromatic C=C stretch coupled to H-C rock
81	1183	1185	R_{xx}	A	HC=CH dihedral bend
80	1163	1159	$[M_{yx}]$*	$[B_x]$*	HC=CH scissor
77	1075	1068	$Q_{x,yz}$	B_x	C-S stretch coupled to ring expansion
76	1071	1065	R_{xx}, M_{yy}	A	C-S stretch
75	1010	994	$[R_{xx}]$*	$[A/B_x]$*	in-plane aromatic ring deformation

a) The calculation model the system as Ag_7-S-DB-S-Ag_7, in its minimum energy configuration. The frequencies are scaled, using the single scaling factor of 0.9675.

b) The dominant matrix element in observed scattering processes: SERS, $R_{ab} =< \mu_{ea}\mu_{eb} >$; SEMRS, $M_{ab} =< \mu_{ea}\mu_{mb} >$; and SEQRS, $Q_{a,bc} =< \mu_{ea}q_{bc} >$. Note, each of these elements describe only two field-matter interactions. The scattering probabilities are squared quantities, with four field-matter interactions. Our treatment is limited to probabilities given by: $|R_{ab}|^2$ for SERS, $R_{ba}M_{ab}$ for SEMRS, $R_{ba}Q_{a,bc}$ for SEQRS.

c) The irreducible representations are for the linker biphenyl with staggered rings, in D_2 symmetry. Instead of the more common notation $B_{1/2/3}$ of the asymmetric modes we have

indicated the principle axes by the coordinate system used in Fig. 2.1, hence $B_{x/y/z}$. (*) indicates modes that do not belong to D_2 symmetry, due to involvement of motion along C-S-Ag.

2.9 References

(1) Le Ru, E.; Etchegoin, P. G. Single-Molecule Surface-Enhanced Raman Spectroscopy. *Annu. Rev. Phys. Chem* **2012**, 1–23.

(2) Kreibig, U.; Vollmer, M. *Optical Properties of Metal Clusters*; Springer-Verlag: Berlin, 2006.

(3) Gunnarsson, L.; Rindzevicius, T.; Prikulis, J.; Kasemo, B.; Käll, M.; Zou, S.; Schatz, G. C. Confined Plasmons in Nanofabricated Single Silver Particle Pairs: Experimental Observations of Strong Interparticle Interactions. *J. Phys. Chem. B* **2005**, *109*, 1079–1087.

(4) Encina, E. R.; Coronado, E. A. Plasmon Coupling in Silver Nanosphere Pairs. *J. Phys. Chem. C* **2010**, *114*, 3918–3923.

(5) Nordlander, P.; Oubre, C.; Prodan, E.; Li, K.; Stockman, M. I. Plasmon Hybridization in Nanoparticle Dimers. *Nano Lett.* **2004**, *4*, 899–903.

(6) Whitmore, D.; El-khoury, P. Z.; Fabris, L.; Chu, P.; Bazan, G. C.; Potma, E. O.; Apkarian, V. A. High Sensitivity Surface-Enhanced Raman Scattering in Solution Using Engineered Silver Nanosphere Dimers. *J. Phys. Chem. C* **2011**, *115*, 15900–15907.

(7) Banik, M.; Nag, A.; El-Khoury, P. Z.; Perez, A. R.; Guarrotxena, N.; Bazan, G. C.; Apkarian, V. A. Surface-Enhanced Raman Scattering of a Single Nanodumbbell: Dibenzyldithio-Linked Silver Nanospheres. *J. Phys. Chem. C* **2012**, *116*, 10415–10423.

(8) Kedziora, G. S.; Schatz, G. C. Calculating Dipole and Quadrupole Polarizabilities Relevant to Surface Enhanced Raman Spectroscopy. *Spectrochim. Acta Part A* **1999**, *55*, 625–638.

(9) Romero, I.; Aizpurua, J.; Bryant, G. W.; García-Vidal, F. Plasmons in Nearly Touching Metallic Nanoparticles: Singular Response in the Limit of Touching Dimers. *Opt. Express* **2006**, *14*, 9988–9999.

(10) Lassiter, J. B.; Aizpurua, J.; Hernandez, L. I.; Brandl, D. W.; Romero, I.; Lal, S.; Hafner, J. H.; Nordlander, P.; Halas, N. J. Close Encounters between Two Nanoshells. *Nano Lett.* **2008**, *8*, 1212–1218.

(11) Pérez-González, O.; Zabala, N.; Aizpurua, J. Optical Characterization of Charge Transfer and Bonding Dimer Plasmons in Linked Interparticle Gaps. *New J. Phys.* **2011**, *13*, 083013.

(12) Marinica, D. C.; Kazansky, a K.; Nordlander, P.; Aizpurua, J.; Borisov, a G. Quantum Plasmonics: Nonlinear Effects in the Field Enhancement of a Plasmonic Nanoparticle Dimer. *Nano Lett.* **2012**, *12*, 1333–1339.

(13) Esteban, R.; Borisov, A. G.; Nordlander, P.; Aizpurua, J. Bridging Quantum and Classical Plasmonics with a Quantum-Corrected Model. *Nat. Commun.* **2012**, *3*, 1–9.

(14) Jensen, L. Surface-Enhanced Vibrational Raman Optical Activity: A Time-Dependent Density Functional Theory Approach. *J. Phys. Chem. A* **2009**, *113*, 4437–4444.

(15) Kneipp, H.; Kneipp, J.; Kneipp, K. Surface-Enhanced Raman Optical Activity on Adenine in Silver Colloidal Solution. *Anal. Chem.* **2006**, *78*, 1363–1366.

(16) Abdali, S. Observation of SERS Effect in Raman Optical Activity, a New Tool for Chiral Vibrational Spectroscopy. *J. Ram. Spectrosc.* **2006**, *37*, 1341–1345.

(17) Acevedo, R.; Lombardini, R.; Halas, N. J.; Johnson, B. R. Plasmonic Enhancement of Raman Optical Activity in Molecules near Metal Nanoshells. *J. Phys. Chem. A* **2009**, *113*, 13173–13183.

(18) Etchegoin, P. G.; Galloway, C.; Le Ru, E. C. Polarization-Dependent Effects in Surface-Enhanced Raman Scattering (SERS). *Phys. Chem. Chem. Phys.* **2006**, *8*, 2624–2628.

(19) Wilson, E. B.; C., D. J.; Cross, P. C. *Molecular Vibrations: The Theory of Infrared and Raman Vibrational Spectra*; Dover: New York, 1980.

(20) Svirko, Y. P.; Zheludev, N. I. *Polarization of Light in Nonlinear Optics*; Willey: New York, 1998.

(21) Nie, S.; Emory, S. R. Probing Single Molecules and Single Nanoparticles by Surface-Enhanced Raman Scattering. *Science (80-.).* **1997**, *275*, 1102–1106.

(22) Morton, S. M.; Jensen, L. Understanding the Molecule-Surface Chemical Coupling in SERS. *J. Am. Chem. Soc.* **2009**, *131*, 4090–4098.

(23) Lombardi, J. R.; Birke, R. L. A Unified View of Surface-Enhanced Raman Scattering. *Acc. Chem. Res.* **2009**, *42*, 734–742.

(24) Novotny, L.; Hecht, B. *Principles of Nano-Optics*; 1st ed.; Cambridge University Press: New York, 2011.

(25) Le Ru, E. C.; Etchegoin, P. G. Rigorous Justification of the |E|4 Enhancement Factor in Surface Enhanced Raman Spectroscopy. *Chem. Phys. Lett.* **2006**, *423*, 63–66.

(26) *We Use the Comsol Multiphysics (ver. 4.2) Code for the Simulations.*

(27) Zuloaga, J.; Prodan, E.; Nordlander, P. Quantum Description of the Plasmon Resonances of a Nanoparticle Dimer. *Nano Lett.* **2009**, *9*, 887–891.

(28) Luo, Y.; Pendry, J. B.; Aubry, A. Surface Plasmons and Singularities. *Nano Lett.* **2010**, *10*, 4186–4191.

(29) Luo, Y.; Lei, D. Y.; Maier, S. a; Pendry, J. B. Transformation-Optics Description of Plasmonic Nanostructures Containing Blunt Edges/corners: From Symmetric to Asymmetric Edge Rounding. *ACS Nano* **2012**, *6*, 6492–6506.

(30) Ayars, E. J.; Hallen, H. D.; Jahncke, C. L. Electric Field Gradient Effects in Raman Spectroscopy. *Phys. Rev. Lett.* **2000**, *85*, 4180–4183.

(31) Buckingham, A. D.; Dunn, M. B. Optical Activity of Oriented Molecules. *J. Chem. Soc.* **1971**, 1988–1991.

(32) Frisch, M. J.; Trucks, G. W.; Schlegel, H. B.; Scuseria, G. E.; Robb, M. A.; Cheeseman, J. R.; Scalmani, G.; Barone, V.; Mennucci, B.; Petersson, G. A.; et al. GAUSSIAN 03, Revision C02; Gaussian Inc.: Pittsburgh, PA, 2003. Frisch, M. J.; Trucks, G. W.; Schlegel,

H. B.; Scuseria, G. E.; Robb, M. A.; Cheeseman, J. R.; Scalmani, G.; Barone, V.; Mennucci, B.; Petersson, G. A.; et Al. GAUSSIAN 03, Revision C02; Gaussian Inc.: Pittsburgh, PA, 2003.

(33) Ruud, K.; Helgaker, T.; Bour, P. Gauge-Origin Independent Density-Functional Theory Calculations of Vibrational Raman Optical Activity. *J. Phys. Chem. A* **2002**, *106*, 7448–7455.

(34) Kwon, K.-Y.; Wong, K.; Pawin, G.; Bartels, L.; Stolbov, S.; Rahman, T. Unidirectional Adsorbate Motion on a High-Symmetry Surface: "Walking" Molecules Can Stay the Course. *Phys. Rev. Lett.* **2005**, *95*, 0–3.

(35) Hallock, A.; Redmond, P. L.; Brus, L. E. Optical Forces between Metallic Particles. *Proc. Natl. Acad. Sci.* **2005**, *102*, 1280–1284.

(36) Dilella, D. P.; Gohin, A.; Lipson, R. H.; Mcbreen, P.; Moskovits, M. Enhanced Raman Spectroscopy of CO Adsorbed on Vapor- Deposited Silver. *J. Chem. Phys.* **1980**, *73*, 4282–4295.

(37) Abe, H.; Manzel, K.; Schulze, W.; Moskovits, M.; Dilella, D. P. Surface-Enhanced Raman Spectroscopy of CO Adsorbed on Colloidal Silver Particles. *J. Chem. Phys.* **1981**, *74*, 792–797.

(38) Seki, H. SERS Excitation Profile of Pyridine and Co on Silver in UHV. *J. Electroanal. Chem.* **1983**, *150*, 425–436.

(39) Dumas, P.; Tobin, R. G.; Richards, P. L. Study of Adsorption States and Interactions of CO on Evaporated Noble Metal Surfaces by Infrared Absorption Spectroscopy. *Surf. Sci.* **1986**, *171*, 555–578.

(40) Föhlisch, a; Nyberg, M.; Hasselström, J.; Karis, O.; Pettersson, L. G.; Nilsson, A. How Carbon Monoxide Adsorbs in Different Sites. *Phys. Rev. Lett.* **2000**, *85*, 3309–3312.

(41) Kudelski, A.; Pettinger, B. Fluctuations of Surface-Enhanced Raman Spectra of CO Adsorbed on Gold Substrates. *Chem. Phys. Lett.* **2004**, *383*, 76–79.

(42) Lemire, C.; Meyer, R.; Shaikhutdinov, S. K.; Freund, H.-J. CO Adsorption on Oxide Supported Gold: From Small Clusters to Monolayer Islands and Three-Dimensional Nanoparticles. *Surf. Sci.* **2004**, *552*, 27–34.

(43) Atay, T.; Song, J.-H.; Nurmikko, A. V. Strongly Interacting Plasmon Nanoparticle Pairs: From Dipole−Dipole Interaction to Conductively Coupled Regime. *Nano Lett.* **2004**, *4*, 1627–1631.

(44) Lambert, D. K. Of the First-Order Stark Effect of Co on Ni(110). *Phys. Rev. Lett.* **1985**, *50*, 2106–2109.

(45) Lambert, D. K. Vibrational Stark Effect of Adsorbates at Electrochemical Interfaces. *Electrochim. Acta* **1996**, *41*, 623–630.

(46) Sanchez, A.; Davis, C. F.; Liu, K. C.; Javan, A. The MOM Tunneling Diode: Theoretical Estimate of Its Performance at Microwave and Infrared Frequencies. *J. Appl. Phys.* **1978**, *49*, 5270–5277.

(47) Krans, J. M.; Rultenbeek, J. M. van; Fisun, V. V.; Yanson, I. K.; Jongh, L. J. de. The Signature of Conductance Quantization in Metallic Point Contacts. *Nature* **1995**, *375*, 767–769.

(48) Hobbs, P. C. D.; Laibowitz, R. B.; Libsch, F. R. Ni-NiO-Ni Tunnel Junctions for Terahertz and Infrared Detection. *Appl. Opt.* **2005**, *44*, 6813–6822.

(49) Choi, K.; Yesilkoy, F.; Ryu, G.; Cho, S. H.; Goldsman, N.; Dagenais, M.; Peckerar, M. A Focused Asymmetric Metal–Insulator–Metal Tunneling Diode: Fabrication, DC Characteristics and RF Rectification Analysis. *IEEE Trans. Electron Devices* **2011**, *58*, 3519–3528.

(50) Hyatt, H. A.; Cherlow, J. M.; Fenner, W. R.; Porto, S. P. S. Cross Section for the Raman Effect in Molecular Nitrogen Gas. *JOSA* **1973**, *63*, 1604–1606.

(51) Stockman, M. I.; Shalaev, V. M.; Moskovits, M.; Botet, R. Enhanced Raman Scattering by Fractal Clusters: Scale-Invariant Theory. *Phys. Rev. B* **1992**, *46*, 2821–2831.

(52) Head-gordon, M.; Tully, J. C. Electric Field Effects on Chemisorption and Vibrational Relaxation of CO on Cu(100). *Chem. Phys.* **1993**, *175*, 37–51.

(53) Wasileski, S. A.; Weaver, M. J.; Koper, M. T. M. Potential-Dependent Chemisorption of Carbon Monoxide on Platinum Electrodes: New Insight from Quantum-Chemical Calculations Combined with Vibrational Spectroscopy. *J. Electroanal. Chem.* **2001**, *500*, 344–355.

(54) Kresse, G.; Gil, A.; Sautet, P. Significance of Single-Electron Energies for the Description of CO on Pt(111). *Phys. Rev. B* **2003**, *68*, 073401–1 – 4.

(55) Gajdo, M.; Eichler, A.; Hafner, J. CO Adsorption on Close-Packed Transition and Noble Metal Surfaces: Trends from Ab Initio Calculations. *J. Phys Condens. Matter* **2004**, *16*, 1141–1164.

(56) Persson, B. N. J.; Persson, M. Vibrational Lifetime for CO Adsorbed on Cu(100). *Solid State Comm.* **1980**, *36*, 175–179.

(57) Tully, J. C.; Gomez, M.; Head-Gordon, M. Electronic and Phonon Mechanisms of Vibrational Relaxation: CO on Cu(100). *J. Vac. Sci. Technol. A* **1993**, *11*, 1914–1920.

(58) Nanba, T.; Yamamoto, I.; Ikezawa, M. Surface Enhanced Raman Scattering of CO Adsorbed on Silver Film. *J. Phys. Soc. Jpn.* **1955**, *1986*, 2716.

(59) Pettenkoffer, C.; Otto, A. "Chemical Effects" of Vibrational Lifetime and Frequencies of CO on Ag. *Surf. Sci.* **1985**, *151*, 37–51.

(60) Rydberg, R. Vibrational Lineshape of Chemisorbed CO. *Phys. Rev. B* **1985**, *32*, 2671–2673.

(61) Le Ru, E. C.; J, G.; Felidj, N.; Aubard, J.; Levi, G.; Hohenau, A.; Krenn, J. R.; Blackie, E.; Etchegoin, P. G.; Ru, E. C. Le; *et al.* Experimental Verification of the SERS Electromagnetic Model beyond the |E|^4 Approximation : Polarization Effects. *J. Phys. Chem. C* **2008**, *112*, 8117–8121.

(62) Bosnick, K.; Jiang, J.; Brus, L. E. Fluctuations and Local Symmetry in Single-Molecule Rhodamine 6G Raman Scattering on Silver Nanocrystal Aggregates. *J. Phys. Chem. B* **2002**, *106*, 8096–8099.

(63) Moore, A. a; Jacobson, M. L.; Belabas, N.; Rowlen, K. L.; Jonas, D. M. 2D Correlation Analysis of the Continuum in Single Molecule Surface Enhanced Raman Spectroscopy. *J. Am. Chem. Soc.* **2005**, *127*, 7292–7293.

(64) Lombardi, J. R.; Birke, R. L. Excitation Profiles and the Continuum in SERS: Identification of Fano Line Shapes. *J. Phys. Chem. C* **2010**, *114*, 7812–7815.

(65) Otto, A.; Akemann, W.; Pucci, A. Normal Bands in Surface-Enhanced Raman Scattering (SERS) and Their Relation to the Electron-Hole Pair Excitation Background in SERS. *Isr. J. Chem.* **2006**, *46*, 307–315.

(66) Michaels, A. M.; Nirmal, M.; Brus, L. E. Surface Enhanced Raman Spectroscopy of Individual Rhodamine 6G Molecules on Large Ag Nanocrystals. *J. Am. Chem. Soc.* **1999**, *121*, 9932–9939.

(67) Galperin, M.; Ratner, M. a; Nitzan, A. Raman Scattering from Nonequilibrium Molecular Conduction Junctions. *Nano Lett.* **2009**, *9*, 758–762.

(68) Grover, S.; Moddel, G. Applicability of Metal/Insulator/Metal (MIM) Diodes to Solar Rectennas. *IEEE J. Photovolt.* **2011**, *1*, 78–83.

(69) Guarrotxena, N.; Ren, Y.; Mikhailovsky, A. Raman Response of Dithiolated Nanoparticle Linkers. *Langmuir* **2011**, *27*, 347–351.

(70) Becke, A. D. Density-Functional Thermochemistry. III. The Role of Exact Exchange. *J. Chem. Phys.* **1993**, *98*, 5648–5652.

(71) Schafer, A.; Huber, C.; Ahlrichs, R. Fully Optimized Contracted Gaussian Basis Sets of Triple Zeta Valence Quality for Atoms Li to Kr. *J. Chem. Phys.* **1994**, *100*, 5829–5835.

CHAPTER 3:

Fluctuation is SM-SERS and Multipolar Raman

3.1 Abstract

Surface enhanced Raman scattering of molecules adsorbed on metal surfaces is commonly subject to intensity fluctuation. This is to be expected in the single molecule limit. As such, intensity fluctuations are often interpreted as the signature of small ensembles of molecules. The origin of intensity fluctuations remains a subject of deliberation. Here, we provide an analysis of a time-series of SERS spectra recorded in the Van Duyne lab, which parallel our observations on the same system. The spectra show fluctuations both in intensity and peak position. Main features of the fluctuating spectra can be explained in terms of field gradient driven multipolar Raman scattering. The long wave limit does not hold for molecules excited in the near-field of nanojunctions, where fields may vary on the length scale of the molecule. As a result, field gradient induced Raman transitions, which include magnetic and quadrupolar Raman transitions, become comparable in intensity to electric-field driven normal (dipolar) Raman transitions. This was shown in our prior work on dibenzyl dithiol on silver dumbbells.[1] Here, we use the same formalism to interpret the SERS spectra of bipyridyl ethylene (BPE) on gold nanosphere dimers encapsulated in silica shells.

3.2 Normal Raman Spectra (NRS)

We show in fig. 3.3.1 the spectral match for the most commonly occurring SERS spectrum of BPE, which characteristically appears at the beginning of time-series studies. The spectrum is quite similar to that of the non-resonant Raman of the molecule in the bulk (fig. 3.1b). We show the spectral match (fig. 3.1a) for the normal dipolar Raman spectrum predicted in the present calculation. Note that the relative intensity of the two strongest modes at ~1640 cm^{-1} and ~1600 cm^{-1} are reversed in the simulation. Other than that, all other lines appear to be adequately reproduced both in their relative intensities and frequencies. The calculated normal mode frequencies and intensities are compared to the matched experimental lines in table 1. The mismatches in frequencies range from ±3 to ±30 cm^{-1}. The spectra is calculated according to the general form

$$\{S_n^2\} = \sum_n \left| \boldsymbol{\varepsilon}_s^* \boldsymbol{P^T \beta' R^T \alpha'}_n \boldsymbol{R \beta P \varepsilon}_i \right|^2 = \sum_n \left| \boldsymbol{E}_s^L \boldsymbol{\alpha'}_n(\Omega) \boldsymbol{E}_i^L \right|^2 \qquad 3.1$$

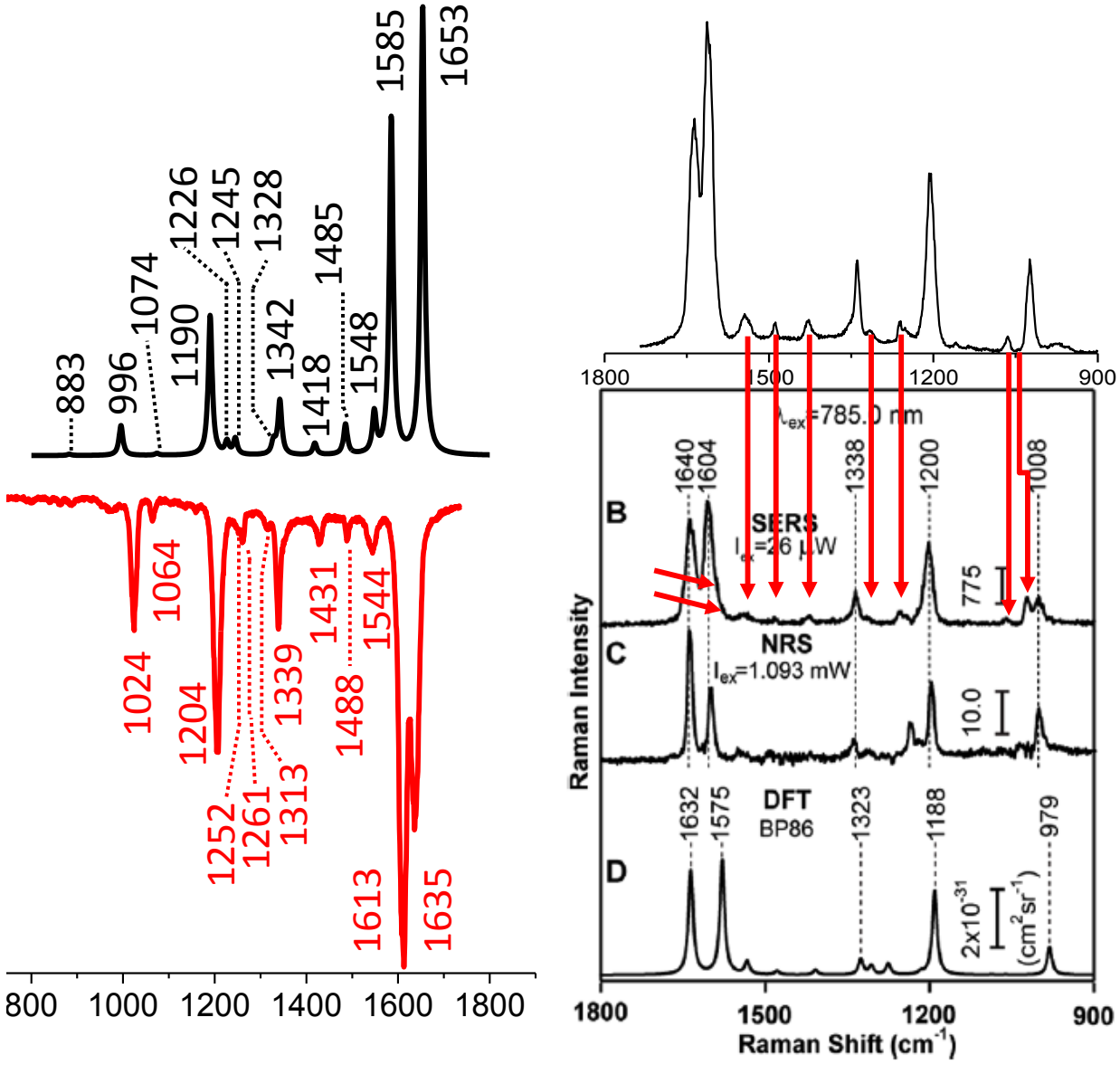

Figure 3.1. (Left) The normal Raman spectrum of BPE calculated (black) and SERS (red) with corresponding frequencies; (Right) Comparison of the experimental spectrum with previously established DFT calculation and bulk BPE spectrum

Table 3.1. The Experimental and calculated Raman lines of BPE and corresponding intensities

	Experiment		Calculation		
	Frequency	Intensity	Frequency	Intensity	Frequency error
A	1635	0.70	1653	1.00	-18
B	1613	1.00	1585	1.00	28
C	1544	0.09	1548	0.08	-4
D	1488	0.05	1485	0.07	3
E	1421	0.05	1418	0.03	3
F	1339	0.22	1342	0.12	-3
G	1317	0.02	1328	0.01	-11
H	1261	0.07	1245	0.04	16
I	1252	0.04	1226	0.04	26
J	1204	0.48	1190	0.30	14
K	1064	0.04	1074	0.005	-10
L	1024	0.25	996	0.07	28
M	886	0.01	883	0.003	3

3.3 Fluctuations in Raman Spectra

We should be clear at the outset that the scope of the present analysis is limited to identifying the spectroscopic origin of the fluctuations. No attempt is made for an exact reproduction of the spectra. We will use calculations based on the isolated bare molecule, therefore there will be no attempt to explain spectral shifts (meandering). The calculation is in C_{2h} symmetry, the molecule has inversion symmetry, therefore the mutual exclusion rule of IR and Raman active lines holds. The 13 assigned lines in table 1, which are common to both SERS and the nonresonant Raman spectrum of the molecule in the bulk, are ascribed to the g-modes. Clearly, the u/g consideration breaks down when the molecule is strongly perturbed by binding interactions and forbidden

modes may become allowed. While this undoubtedly is part of the dynamics behind the fluctuations, it alone cannot explain the observed spectral fluctuations. In particular, the strong structural perturbation model cannot explain the observation of new modes appearing in the spectra that are as strong as the strongest allowed modes, while most other spectral features are unperturbed. We should point that, in departing with the earlier work of Schatz and Van Duyne on the same molecule[2] in which orientationally averaged spectra are used (fig. 3.1c), we evaluate the spectrum for a single orientation of the molecule relative to the field (E-field along the long axis of the molecule in fig. 3.1a). That the two calculations yield nearly identical spectra is characteristic of aromatic molecules with a dominant principle axis, which leads to a polarizability ellipsoid that is dramatically stretched along the long axis.

A series of fluctuating spectra recorded from an isolated single Au-dumbbell is shown in fig. 3.2. The entire sequence of 360 spectra contains four instances in time where they fluctuate, what may be associated with four main events. These instances are noted as 1, 2, 3 and 4 on the time-series in the image plot (fig. 3.3). The spectra recorded outside these three time-windows vary in overall intensity, but do not show significant variation in their spectral pattern - they define the base spectrum (S_b), which is nearly identical to the normal SERS spectrum shown in fig. 3.1. The fluctuating spectra are grouped as S_1 (fig. 3.3a), S_2 (fig. 3.3b), S_3 (fig. 3.3c) and S_4 (fig. 3.3d) in order of their appearance in time.

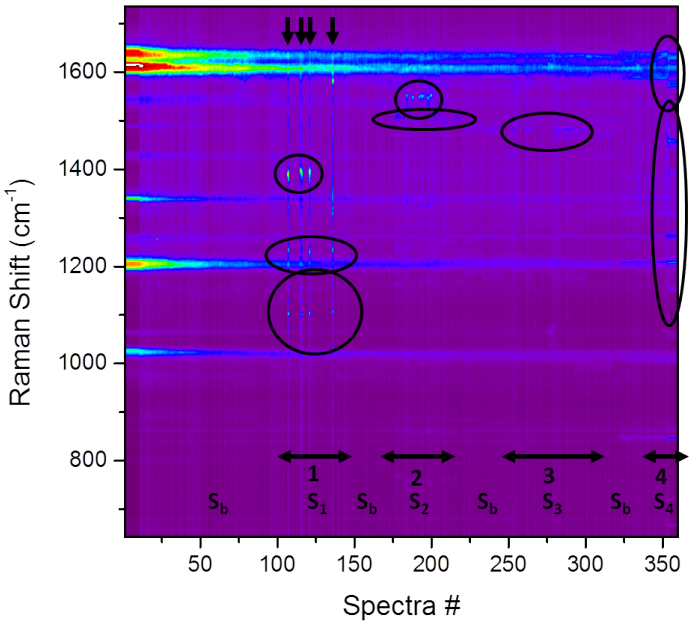

Figure 3.2. Fluctuating Raman spectra of BPE recorded on a single dumbbell as a function of time.

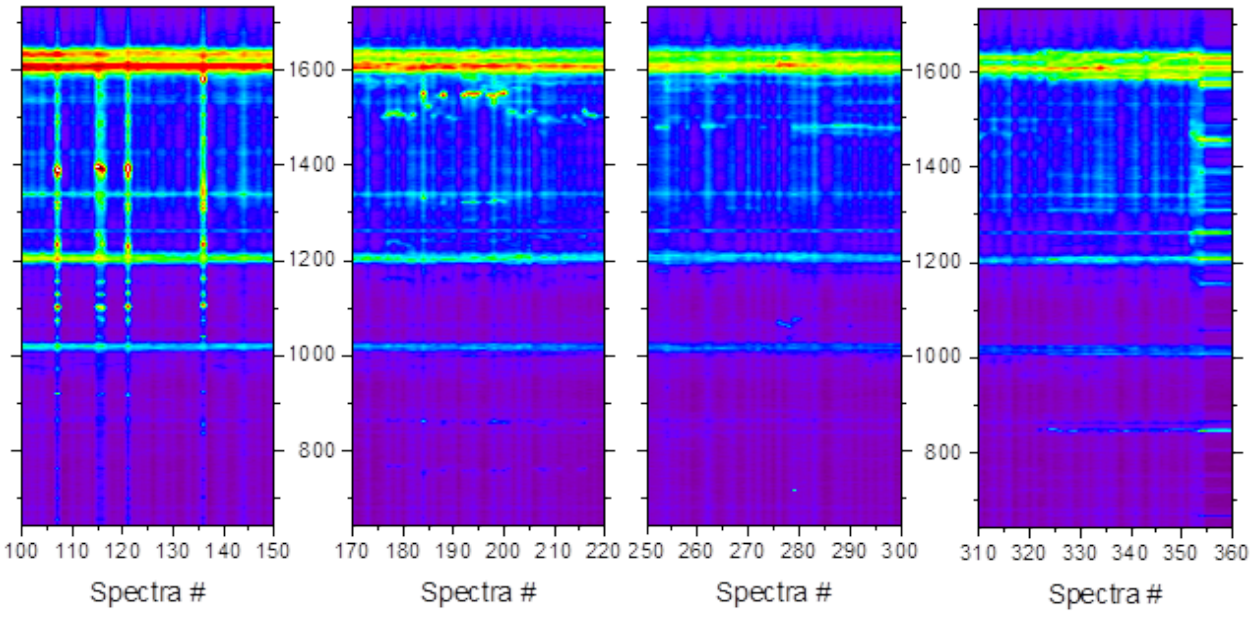

Figure 3.3. Four time-sections that will be used to elaborate the fluctuation in Raman spectra.

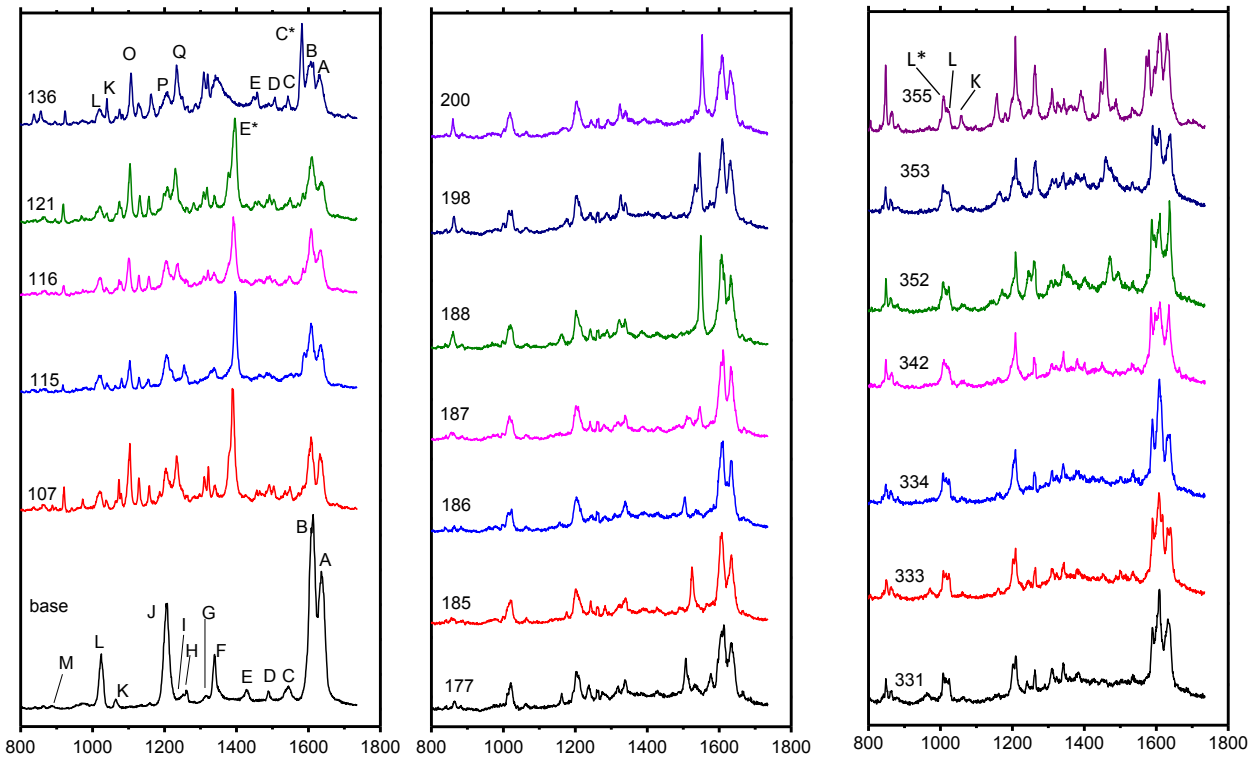

Figure 3.4. First second and fourth time segments from the image plot of fig. 3.2.

The commonly occurring SERS, or the NRS of bulk BPE, allow the assignment of the normal (dipolar) Raman lines. In the fluctuating spectra recorded in regions S_1 and S_3 of figs. 3.3a and 3.3c, new lines appear and disappear in time, as exemplified by the set in fig. 3.4. (The spectra at the vertical streaks of fig. 3.3a are plotted in fig 4a). For a close up, consider fig. 3.5. Spectrum # 56 is the normal Raman spectrum, with all lines accounted in table 1. A new line (C*) appears in spectra # 167 and 335, at ~1580 cm^{-1}. Lines A, B and C are present in the normal Raman spectrum, C* is not.

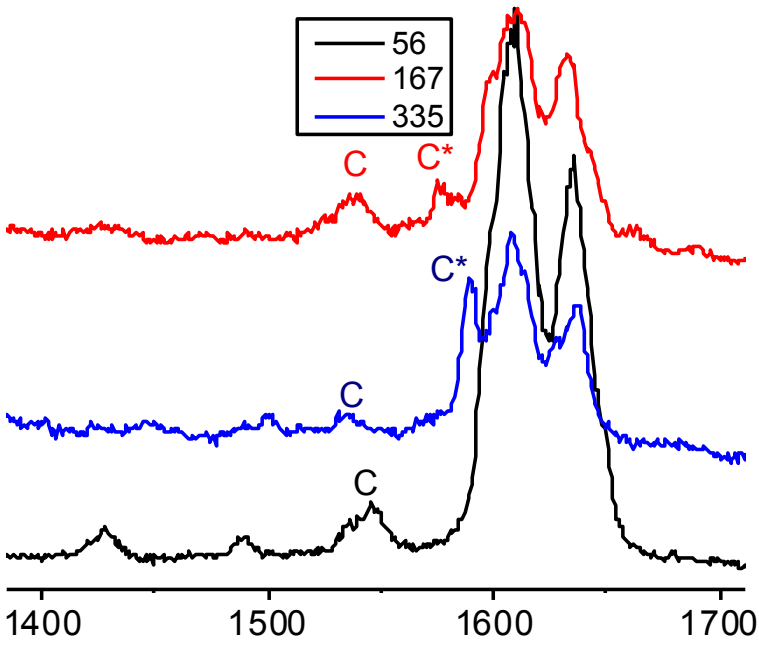

Figure 3.5. Appearance of non-Raman line(C*).

3.4 Raman-forbidden lines and their assignments

Another strong line (E*), which is absent in the NRS of BPE, appears at ~ 1390 cm^{-1} in spectra #107 - #121. The fluctuating spectra show many more lines than the NRS, as in # 107, 116, 121 and 136. The observed number of lines exceeds the total number of Raman allowed g-modes in this spectral range. The shear count of the observed lines forces the conclusion that Raman-forbidden u-modes are being observed in addition to the allowed g-modes. This is not a weak effect - some of the new u-lines are as intense as the most intense normal Raman lines. In Table 2 we provide all the normal modes of the molecule along with their parity, and the spectral range in which their assignments appear.

Table 3.2. Normal mode analysis of BPE and corresponding parity

mode #	Calculation (ω_{calc}) As calculated	Anharmonicity corrected "g"-modes	Anharmonicity corrected "u"-modes	ω_{expt}		
56	1688	1653		1631-1639	A	C=C stretch
55	1632		1588	1608-1620	B	Ring deformation with aeromatic H-C=C-H scissor
54	1627	1585				
53	1590		1553	1573-1590	C*	aeromatic H-C=C-H rocking
52	1581	1548		1535-1545	C	
51	1527		1491	1540-1550	D	aeromatic H-C=C-H rocking
50	1520	1485		1480-1507		
49	1446		1422	1390	E*	Ring deformation with aeromatic H-C=C-H scissor
48	1442	1418		1425,1460-70	E	
47	1375		1346	1339	F	aeromatic H-C=C-H rocking
46	1365	1342				
45	1343	1328		1317	G	aeromatic H-C=C-H rocking
44	1326		1295			
43	1281	1245		1261	H	Ring deformation; not complementary
42	1278		1253			
41	1248		1188	1252	I	aeromatic H-C=C-H scissor
40	1247	1226				
39	1232		1211	1204	J	Ring deformation; C-H scissor
38	1215	1190				Ring deformation
37	1115	1097		?		aeromatic H-C=C-H scissor
36	1113		1093			
35	1090		1086	1064	K	Ring deformation

34	1090	1074				
33	1010		973	1010	L*	Ring deformation
32	1009	995		1024	L	
31[$]	1002		987	1010		Out of plane aeromatic H-C=C-H wag with H-C=C-H[*] twist
30	998	1008				Out of plane aeromatic H-C=C-H twist
29	998		1019			
28	975	982				Out of plane aeromatic H-C=C-H twist
27	971		977			
26[$]	908	917				Out of plane aeromatic H-C=C-H wag with H-C=C-H[*] twist
25[$$]	890	883		886	M	Ring deformation with =C-C=[*] stretch
24	870		868	880		Out of plane aeromatic H-C=C-H wag
23	866	892				with =C-C=[#] stretch
22[$$]	847		845	865	N	Ring deformation with =C-C=[*] stretch
21	834		835	848		Out of plane aeromatic H-C=C-H wag
20	805	804				with H-C=C-H[*] wag (#21)/twist (#20)

[*] non-aeromatic;
[$],[$$]identical mode pattern with complementary parity;
highlighted rows are M-N, L-L*, C-C* are the u-g mode pair that can be distinctly identified

Note, the g/u exclusion principle holds only for dipolar coupling to the electric field. The u modes are Raman active in magnetic and electric quadrupolar Raman scattering. Except for the 1653 cm^{-1} mode, the g/u modes appear in pairs in table 3.2, as in-phase and out-of-phase components of a given normal mode, with ~0.1-20.0 cm^{-1} energy splitting between the pairs. Whether the g or u mode is higher in a given pair is not systematic. Since the frequency differences in the pairs are within the accuracy of the calculations, the experimental lines cannot be assigned based on frequencies alone. Since most of the g-modes were already assigned in the

normal Raman spectrum, the new lines that appear to fluctuate in time will principally be assigned to the u-modes. We will use the alphabetic naming of normal modes given in table 3.2.

Prior to the simulations, it is useful to consider a few of the assignments more closely, to highlight the challenges. In the calculated lines, there is only one u/g pair (1418/1422 cm^{-1}) in a span of ~ 150 cm^{-1} (see table 2) However, several lines (F, G,and H) appear in this range in the experimental spectra. F is well established as a normal Raman line. E* appears as a multipolar (quadrupolar) line, which is often the brightest line in the entire spectrum. It seems to appear at ~1470 cm^{-1} (#352 - #355) and at ~1390 cm^{-1} (#107 - #126) in the different segments. Also, occasionally there is another shoulder present at ~1375 cm^{-1}. The theory cannot account for splitting of nondegenerate spectral lines. This can arise either from strong intermolecular coupling where there are several molecules, or could potentially be due to the time-sampling of bistable sites under the inhomogeneously broadened line. Hence, both E* and its shoulder are assigned to the 1418 cm^{-1} u-mode. By default, the 1470 cm^{-1} line is assigned to the 1422 cm^{-1} g-mode (Table 3.2). The time series S_3 is characterized by the meandering of the ~1480 cm^{-1} line and its bifurcation between spectra #280 and ~#290. This main distinguishing feature in S_4, which is suggestive of intermolecular coupling between two molecules, cannot be addressed by the calculations. All other features of the spectra are reasonably explainable.

3.5 Theoretical framework

To simulate the spectral patterns, we assume linearly polarized electric field $E = \begin{pmatrix} 1 \\ 0 \\ 0 \end{pmatrix}$ and a field gradient matrix comprised of only four terms: $E' = \frac{dE_i}{dj} = \begin{pmatrix} 0 & 0 & 1 \\ 0 & 0 & 1 \\ 1 & -1 & 0 \end{pmatrix}$. This choice

of field gradient matrix implies B along E: $B_i = \boldsymbol{\varepsilon_{ijk}}\left(\frac{dE_j}{dk} - \frac{dE_k}{dj}\right) = \begin{pmatrix}1\\0\\0\end{pmatrix}$. This implies a chiral local field, $\mathbf{E}\times\mathbf{B} \neq 0$, which can be separately justified (see eqn. 2 below). We allow independent rotation of the gradient matrix and the electric field relative to the molecular frame; as such, we do not limit the simulations to chiral local fields. Rotation of the molecular polarizability tensor by Euler angle {α,β,γ} is equivalent to rotation of the electric field relative to the molecular frame $E(\alpha\beta\gamma) = \mathbf{R}(\alpha,\beta,\gamma)E$, and the operative field gradient matrix is rotated to $E'(\alpha'\beta'\gamma') = \mathbf{R}(\alpha',\beta',\gamma')E'\ \mathbf{R}^{\mathbf{T}}(\alpha',\beta',\gamma')$. Although we allow for independent rotation of field and field gradient matrix, the best spectral matches are obtained for {α,β,γ} ~ {α',β',γ'}, i.e., electric and magnetic fields point along the same axis (chiral). This can be easily justified by expanding the incident fields to first order in spatial dispersion, $e^{ikr} = 1 + ikr$. Considering propagation along the z-axis, we obtain:

$$\langle(1 + ikz)(\partial_x + \partial_y)\rangle^2\langle dd\rangle = \langle dd\rangle\sum_{i,j=x,y}\left(\omega\langle d_i\rangle - a\ k\langle m_j\rangle\right)^2 + (b\ \omega k\langle q_{iz}\rangle)^2 \qquad 3.2$$

which contains, electric dipole (d), magnetic dipole (m), dichroic (md) cross term under the square in eqn. 3.2 and quadrupolar (q_{iz}) transitions. The relative strength of the magnetic and quadrupolar transition is given by *a* and *b* respectively. The individual terms in 3.2 are evaluated as:

$$dd = \langle\varepsilon_s|\boldsymbol{\alpha'}|\varepsilon_i\rangle \qquad 3.3a$$

$$md = \langle\varepsilon_{s,\alpha}\left|\boldsymbol{G'_{\alpha,\beta}}\right|\delta\varepsilon_{i,\beta}\rangle \qquad 3.3b$$

$$qd = \langle\varepsilon_{s,\alpha}|\boldsymbol{A_{\alpha,\beta\gamma}}|\delta\varepsilon_{i,\beta\gamma}\rangle \qquad 3.3c$$

with α', G', A tensors obtained from the ROA suite in Gaussian.

3.6 Simulations

Spectral reproduction of each and every spectrum will be very tedious. Instead, we pick few representative entries from each set in time that contains the fundamental nature of spectral fluctuation that the molecule undergoes. A set of these chosen spectra is shown in fig. 3.6, where #121 is from S_1, #177 & 198 are from S_2, #333, 351, 352 & 353 are from S_4.

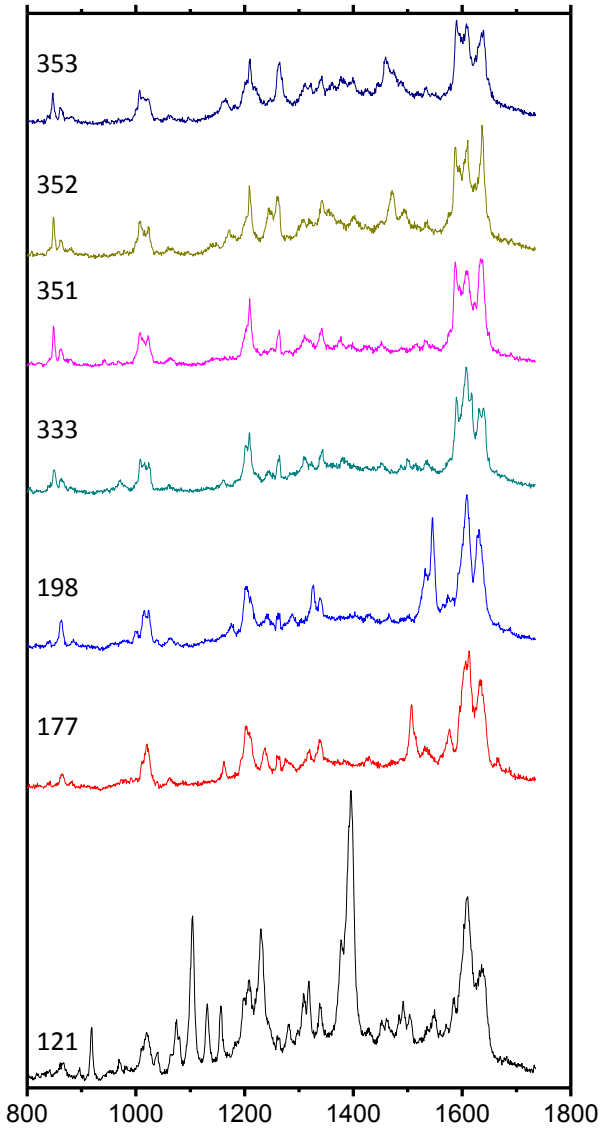

Figure 3.6. Representative individual spectra from the entire time series, to which theoretical spectra will be simulated.

3.6.1 S_2 Event:

We consider in fig. 3.7 two characteristic spectra, #177 and #198 from the S_2 set. The two spectra can be reproduced as a combination of only electric and magnetic dipolar Raman (b=0 in eqn. 2), with electric field and field gradient pointing in the same direction E||B. Few degrees of molecular reorientation, or deviation between E and B axes, leads to subtle spectral variations, as in the experiment. To be more precise, consider the strong high frequency lines: A, B, C* and C. The A:B ratio stays fairly constant as in normal Raman. C* and C are the u/g symmetry pairs of the same mode, predicted to be only 5 cm^{-1} apart. C* upshifts in frequency and C downshifts in frequency making them appear as distinct lines. E* is absent in the entire sequence; C is weak in #177, almost absent in #185 & 198, and clearly absent for the rest of the series. D can vary in intensity and can become the strongest line in the spectrum. Although every normal mode has a symmetric (g) and a corresponding anti-symmetric (u) counterpart, either, both or none of these modes may light up. A is only activated by electric dipolar Raman, D is magnetically active, B has contributions from both of these channels. F-G doublet feature around 1320 cm^{-1}, L-L* doublet feature around 1110 cm^{-1} and low lying N mode can be clearly identified. Several other lines can also be identified with lesser degree of accuracy as in fig. 3.7. Position of D remains ambiguous as it appears at 1504 cm^{-1} in #177 and 1545 cm^{-1} in #198.

At this specific molecular orientation $\{\alpha,\beta,\gamma\} \sim \{50,75,0\}$, electric quadrupolar transition activates E*, which is absent in the entire S_2 set. Absence of E* eliminates the quadrupolar contribution to the spectral match (b=0). The spectral reproduction of the set S_2 suggests parallel electric and magnetic dipolar fields to be operative at the location of the molecule without any electric quadrupolar field present.

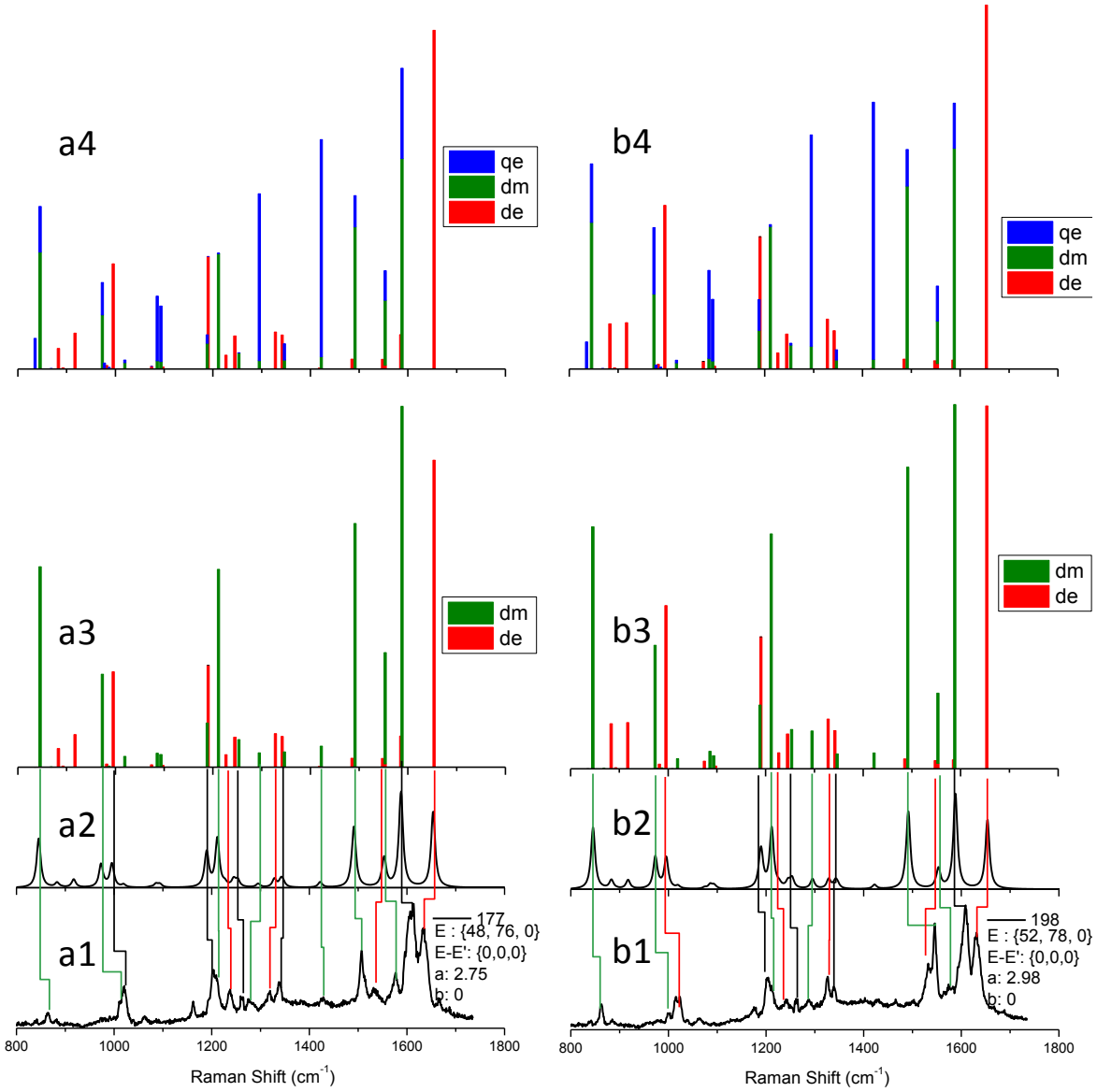

Figure 3.7. Two representative spectra (# 177 and 198) from the S_2 set are shown in panel a1/b1. The Euler angle rotation of the molecule with respect to local electric field is indicated in the legend, along with the difference in angles between electric and magnetic field. The coefficients, a and b, are the relative weights of the magnetic and quadrupolar terms that appear in equation (2). The synthetic spectrum assumes 10 cm^{-1} Lorentzians associated with each line. Note the absence of the quadrupolar (blue) lines in the spectra. b=0 implies absence of quadrupolar contribution to the Raman spectrum. Stick spectrum of unscaled multipolar components is shown in panel a4, and a3 contains those scaled by a and b. Without any correction of spectral position leads to spectra obtained in a2 which is spectral reproduction on the experimental spectrum a1. Red, green and

black lines are drawn to provide visual cue corresponding only electric dipolar Raman, only magnetic dipolar Raman and both.

3.6.2 S_4 Event:

In the S_4 event, the spectral fluctuation is characterized by the varying relative intensity of A, B and C. Four different A:B:C intensity patterns are seen in the four selected spectra from this time segment, in fig. 3.8. D is absent in the entire series, E* is present in #352, 353 but absent/weak in #333, 351. Once again, E* is predominantly a quadrupolar transition, which is implied by the indicated "b" value of the fitting function for #333 & 351, which is somewhat lower that the b-values seen in #352 & 353. L-L* doublet appears as a broad peak in the measurement, and can be identified through the simulation. According to the electronic structure calculation, for the doublet near 1010 cm^{-1}, there is a pair (mode 32-33 in table 2) of u- and g-modes that are nearly degenerate in the calculated spectrum. Experimentally, we observe a Raman line at 1024 cm^{-1} (L) and occasionally another weak line 1010 cm^{-1} (L*). Moreover, the 1010 cm^{-1} line is accompanied by the lines that are assigned to quadrupolar/magnetic response. The discrepancy of 20 cm^{-1} in splitting between these lines is typical of the mismatch between calculation and theory. Similar interpretation holds good for M-N pair where M is assigned to 886 cm^{-1} 25^{th} mode with g-parity and N is assigned to 865 cm^{-1}, which is 22^{nd} mode with u-parity. M is one of the normal Raman lines that is present in NRS. Although weak, M is present in series S_2. N is it's sister mode with u-parity which is very distinct in S_4. Two other modes of u-parity create the low-lying cluster of lines at ~850 cm^{-1} in S_4. Mode# 21 and 24 at 848 cm^{-1} 880 cm^{-1} mostly magnetic whereas N at 865 cm^{-1} has both magnetic and quadrupolar contribution. It is also worth mentioning that these low lying modes mostly result from out of plane vibrations. These extra modes will disappear if the embedment geometry of the molecule forbids out of plane deformations and N will be the only line in this region as in S_2.

Moreover, throughout the time series there are distinct lines that show splittings. #333 in fig. 3.8 is one typical example. In this case, line A and B are clearly split, and the splitting in C appears as a shoulder. Splittings like these are distinguishable and recurrent. The effect might be argued in favor of presence of few molecules. In the case of coupling between two molecules, strongly coupled lines split into two components, into an in-phase and out-of-phase pair. In multiple coupled molecules, more complicated splitting patterns can be expected, which in the present would be expected to lead to asymmetric, split, inhomogeneous line profiles. Indeed, there is significant variation and fluctuations in linewdiths and profiles, as can be seen by inspection of spectra #351, 352 & 353 in fig. 3.8. It can be seen that the A, B & C lines are sharp (~5 cm^{-1}) in #352, moderately broad (~12 cm^{-1}) in #351 and quite broad (~18 cm^{-1}) in #353. Multiple coupled molecules is a plausible contribution to this.

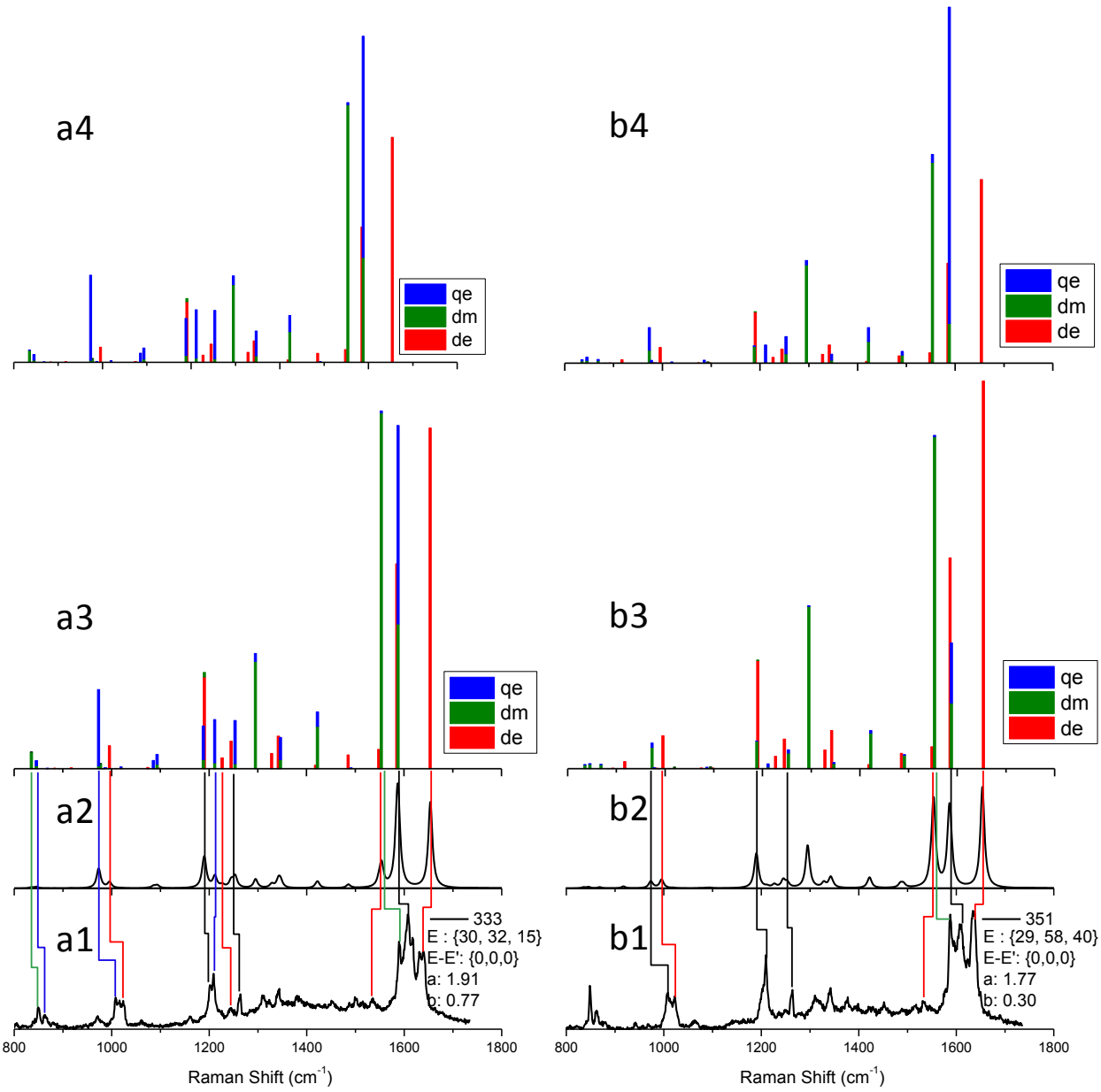
a4
b4
qe
dm
de
a3
b3
a2
b2
a1
b1
333
E : {30, 32, 15}
E-E': {0,0,0}
a: 1.91
b: 0.77
351
E : {29, 58, 40}
E-E': {0,0,0}
a: 1.77
b: 0.30
800
1000
1200
1400
1600
1800
Raman Shift (cm-1)

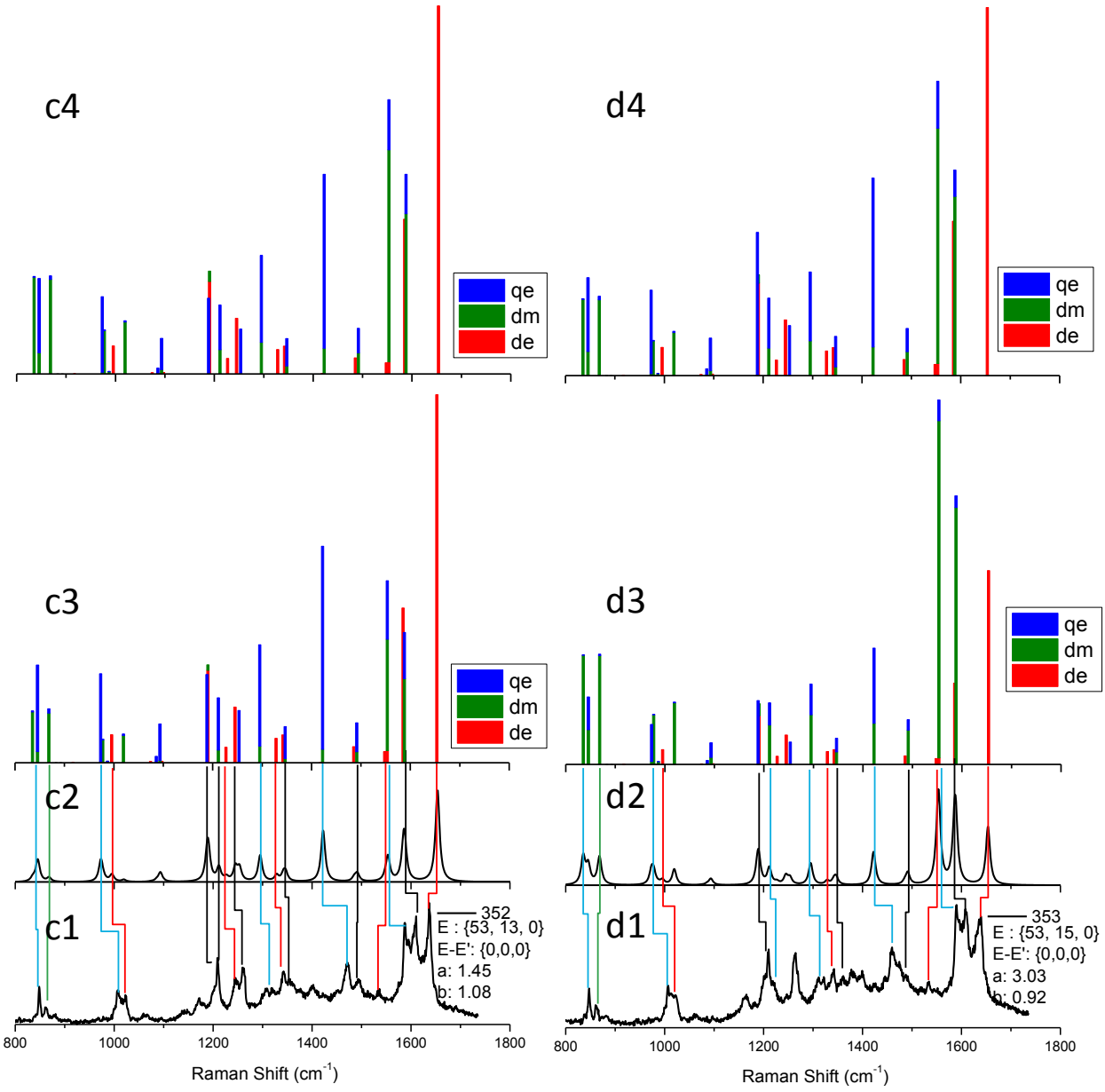

Figure 3.8. Four representative spectra (# 331, 351, 352, 353) from the S4 set. Note the variation in relative intensities of the three main lines A:B:C. The trends can be reproduced by adjusting the mag:quad (a:b) ratio, and varying the orientation of the molecule relative to the E field, which is taken to be parallel to the B-field. The rest of the spectral features are adequately reproduced, especially if one recognizes that the there can be orientational fluctuations on a time scale faster than the acquisition time. Over here, the blue and cyan guideline corresponds to only quadrupolar vs. both quad-mag contribution to be present. Up-shifted assignment of E*-line should be noted.

3.6.3 S_1 Event:

The E* line, which is prominent in the S_1 set (first panel fig. 3.2), is all but absent in S_2. It appears in S_4 (panel c and d in fig. 3.8), and can be clearly identified as quadrupolar. Note however that this assignment implies that there is a 60 cm^{-1} downshift of this assignment between the two sets: 1394 cm^{-1} in S_1 (#107, 115, 116, 121) and ~1456 cm^{-1} in S_4 (#352, 353, 355). It is not possible to assign these lines to different normal modes. The calculation predicts only two modes in this spectral range: one g-mode at 1418 cm^{-1} and one u-mode at 1422 cm^{-1}. The large shift of this line may be associated with the fact that in the S_1 set, where the down-shifted E* line is prominent, we also see bright (vertical) streaking. The latter we associate with arcing across the junction. As such, it may be the case that the E/E* line undergoes a large shift when current passes through the molecule. The discrepancy in the position of the assigned E* line in S_1 is shown in fig. 3.9. Note also the small separation between E and B field directions assumed in that simulation. In spectrum # 121, several other lines can be identified to the prediction.

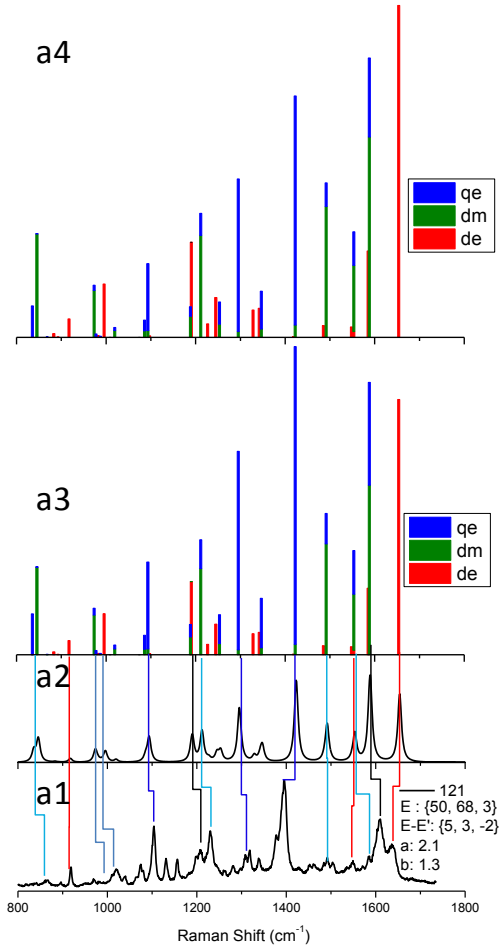

Figure 3.9. A spectrum from S_1, in which the discrepancy between the predicted position of the E*-line and it's down-shifted assignment should be noted.

3.7 Concluding remarks

Summarizing, the entire time series starts with very bright normal dipolar Raman spectra, which decays in intensity during the first ~100 measurements. Then (S_1) a few arcing events are seen, which may be a possible result of plasmonic current tunneling from metal to metal through the molecule. The entire spectrum brightens and extra lines (E* at ~1394 cm^{-1} and several others in the range 1000-1400 cm^{-1}) show up. The spectra can be adequately explained by the inclusion of field gradient induced multipolar Raman with comparable magnetic and quadrupolar contributions. Following in (S_2), C* appears intermittently and D meanders between 1490 cm^{-1} and 1540 cm^{-1} (presence of C* and D is almost complementary; only in #177 both C* and D are present but of them are weak) and E* stays mostly absent. The condition for spectral reproduction demands presence of only magnetic dipolar spectra along with the electric dipolar (normal Raman) spectra. The quadrupolar response at this field-molecule relative orientation results in strong E* line, which is absent in S_2, thereby confirming the absence of a quadrupolar field at the molecular site. E disappears at #220 and starting at #223 (S_3) E* appears. E* meanders until #265, disappears until #280, when it appears again and evolves as split doublet until #300, and disappears thereafter. The physics of meandering and splitting spectral lines stays beyond the scope of current analysis. The meandering of spectral lines may be associated with variations in molecular environment. A shift in line position, as opposed to line broadening, suggests single molecule behavior. Note that asymmetric chemisorption of the molecule (one ended) would break the u/g symmetry and could turn on the u modes, along with possible shifts of the lines directly affected by binding. At the very end of the sequence (S_4) A, B, C, D and E* are present with various relative intensity. E* appears at ~1450 cm^{-1} in this region. With respect to electric dipole, spectral reproduction in this region requires comparable magnetic dipolar

contribution, and similar or much less quadrupolar contribution (quadrupolar contribution can be assessed by the strength of E*).

The fluctuating series of spectra undoubtedly reflects an evolving junction, and geometry of molecule-junction binding. As the junction evolves, so does the local field and field gradient experienced by the molecule. E/E* modes correspond to large motion of the pyridine (Nitrogen) atom. Since the entire molecule is bound through N to the metal, the corresponding modes will be seriously affected. In this particular case, the u-(g-) mode correspond to the N atoms moving out of (in) phase. So, symmetric vibration will correspond to physical translation across the anchored gap as opposed to the molecule rotating across the junction for anti-symmetric vibration. Nevertheless, one of the u-g-pair may undergo large shift over the other.

The best spectral matches are obtained with E||B. For few spectra in series S_1, there is a small angle between the electric and magnetic local fields (as deduced from the required rotation angle between the defined field and field gradient matrix) e.g., $\Delta\Omega = \{5°, 3°, -2°\}$ in spectrum #121. E||B implies plasmon oscillations accompanied with circulation about the dumbbell long axis (a vortex at the junction).

3.8 References

(1) Banik, M.; El-Khoury, P. Z.; Nag, A.; Rodriguez-Perez, A.; Guarrottxena, N.; Bazan, G. C.; Apkarian, V. A. Surface-Enhanced Raman Trajectories on a Nano-Dumbbell: Transition from Field to Charge Transfer Plasmons as the Spheres Fuse. *ACS Nano* **2012**, *6*, 10343–10354.

(2) Yang, W.; Hulteen, J.; Schatz, G. C.; Duyne, R. P. Van. A Surface-Enhanced Hyper-Raman and Surface-Enhanced Raman Scattering Study of Trans-1 , 2-Bis (4-Pyridyl) Ethylene Adsorbed onto Silver Film over Nanosphere Electrodes. Vibrational Assignments: Experiment and Theory. *J. Chem. Phys.* **1996**, *104*, 4313–4323.

Chapter 4:

Electronic Raman Spectrum of Plasmonic Nano Antennae

4.1 Abstract

We characterize the broad background present in the Surface enhanced Raman spectra (SERS) to electronic Raman scattering (ERS) of the metal. The background that we observe from our gold dumbbell equipped with *trans*-1,2-bis(4-pyridyl)-ethylene (BPE) as SERS reporter molecule is generic. A simple model of joint electron-hole distribution is used to simulate the spectrum with good fidelity. Since the occupation probability of the free carriers follow Fermi-Dirac statistics, The anti-Stokes in ERS can be used to measure the local temperature, on nm-scale. In effect, the method yields a nano-thermometer.

4.2 Introduction

Surface enhanced Raman spectra (SERS) recorded on plasmonic nanoparticles are almost always accompanied with a scattering background. The experiments described here are on silica encapsulated gold dumbbells with *trans*-1,2-bis(4-pyridyl)-ethylene (BPE) as SERS reporter. The experimentally obtained SERS consists of sharp vibrational lines of BPE riding on top of a background that appears as a broad continuum. The origin of the background continuum is not molecular. We assign it to electronic Raman of the plasmonically active gold nanoparticles that comprise the dumbbell structure.

4.3 Electronic-Raman

Indeed gold has a broad interband transition peaked at about 2.5 eV (500 nm) which extends down to 2 eV (620 nm).[1] However, based principally on polarization, the Stokes side of the Raman spectrum does not contain an emission feature that can be assigned to an interband transition. Interband transitions, absorption followed by fluorescence, should be accompanied by electron-electron or electron-phonon collisions, which scramble the polarization of the emission. The scattering strength of the background continuum is strongly polarized, with little or no isotropic component. And the strong dipolar asymmetry of emission implies that the radiation is taking place prior to scattering or dephasing. Hence, the emission retains the polarization information of the excitation beam and recognizes the physical shape and orientation of the dumbbell with which the emission is aligned. Luminescence prior to dephasing, defines Raman. We therefore assign the continuum to Raman of the gold nanoparticles.

4.4 electron-hole distribution: Mathematical formulation of Electronic Raman

In the absence of interband transitions, dephasing is the governing mechanism of absorption in metals. Assuming a Fermi surface parabolic in the energy-momentum plane, vertical transition cannot simultaneously conserve energy and momentum. In a single band, there is no vertically accessible state. Hence, electron-electron or electron-phonon scattering must be present to conserve momentum (non vertical transition). In the visible region, i.e. below the metal plasmon resonance, the optical response of the metal is characterized by its permittivity $\varepsilon = \varepsilon' + i\varepsilon''$, where ε' and ε'' are the real and imaginary part of the dielectric response. ε' relates to the elastic response that leads to Rayleigh scattering, while ε'' relates to the dissipative absorption. ε'' arises strictly from electron-electron or electron-phonon scattering. Here, we focus our attention on inelastic coherent scattering without real absorption, which in Raman is often represented to occur via virtual states. This is the so-called $R^{(3)}$ component of the imaginary third order polarization, which defines Raman[2] This effectively non-resonant Raman scattering process may be cast in the form of Fermi's golden rule:

$$W(\omega_{is}) = \frac{2\pi}{\hbar}\sum_m \sum_n |M_{nm}|^2 \delta(\hbar\omega_{is} - \mathcal{E}_{nm}) \qquad 4.1$$

in which $\omega_{is} = \omega_i - \omega_s$ is the Raman shift given as the difference between incident and scattered photon frequencies, and $\varepsilon_{nm} = \varepsilon_n - \varepsilon_m$is the energy difference between initial and final states, and the summation is over all initial and final states. Identifying the initial states as the occupied electron states of the metal in energy representation, $P_e(E)$, and the final states as the available hole states, $P_h(E+\boldsymbol{\varepsilon}_{nm})$, the double summation in 4.1 reduces to the integral over the joint electron-hole pair distribution:

$$W(\mathcal{E}) = \frac{2\pi}{\hbar}\int |M_{eh}|^2 \rho(E) f(E) \rho(E+\mathcal{E})\big(1 - f(E+\mathcal{E})\big) dE \qquad 4.2$$

The matrix element represents the spatial part of the light matter interaction, $A \cdot \nabla$. Recognizing that only p-polarized light, with electric field normal to the metal surface can lead to excitation; and that the penetration depth of the field into the metal half-space is limited to the skin depth $1/q$, and taking $\boldsymbol{A} = \boldsymbol{A_0} e^{-qz} = \boldsymbol{A_0} e^{-qr_\perp}$ for electron-hole pair excitation, the matrix element reduces to:

$$\begin{aligned} M_{eh} &= A_{0,i} A_{0,s} \int e^{-2qr_\perp} \left\langle k'(E+\varepsilon) \middle| \partial_\perp \partial_\perp \middle| k(E) \right\rangle dr_\perp \\ &= A_{0,i} A_{0,s} k'k \int_0^\infty e^{-i(k-k')z - 2qz} dz \\ &= A_{0,i} A_{0,s} k'k \frac{1}{2q + i(k-k')} \\ &= \frac{2m_e}{\hbar^2} \sqrt{E(E+\varepsilon)} A_{0,i} A_{0,s} \frac{1}{2q + i\sqrt{2m\varepsilon/\hbar}} \end{aligned} \quad 4.3$$

Note, in the case of a plane wave $q = \infty$, only Rayleigh scattering is possible, $M_{eh} = \delta[k,k']$. It is the damping function that allows Raman. Assuming a density of states given for a 3D Fermi gas, $\rho(E) = \sqrt{E}$, the spectrum reduces to:

$$W(\mathcal{E}) = \frac{4\pi m_e}{\hbar^4} I_i I_s \int E^{\frac{3}{2}} f(E) (E+\mathcal{E})^{3/2} \big(1 - f(E+\mathcal{E})\big) \frac{1}{2q^2\hbar/m_e + \mathcal{E}} dE \quad 4.4$$

Note, both incident and scattered fields appear in this expression, as would be for in stimulated Raman. This will be modified below, when we take the explicit form of the scattering into account. The scattered field will be replaced either by the vacuum density to treat spontaneous Raman, or by the local density of states to treat plasmon enhanced Raman. More importantly, we note that the same form would have been obtained if we were to carry out the evaluation of the matrix element in energy representation, and were to assume the orthogonality of the Bloch states to be relaxed by Landau damping. These two models essentially come out to be the same, as verified by numerical calculations because, for dephasing time $\tau \sim 5\ fs$ and Fermi velocity $v = 1.8*10^8\ cm/s$, penetration depth $l = v\tau \sim 10\ nm$. In both cases, the spectral profile would be

determined by the Lorentzian function. Although qualitatively in agreement with the experiment, this model cannot be brought into quantitative agreement with the observed spectra, as illustrated in fig. 4.1. The comparison misses in two distinct aspects on the Stokes side: the spectrum is too sharp at small shifts and it never decays to zero. The latter is clear from the functional composition of eqn. 4.4 The density of states grows exponentially at large shifts, and therefore

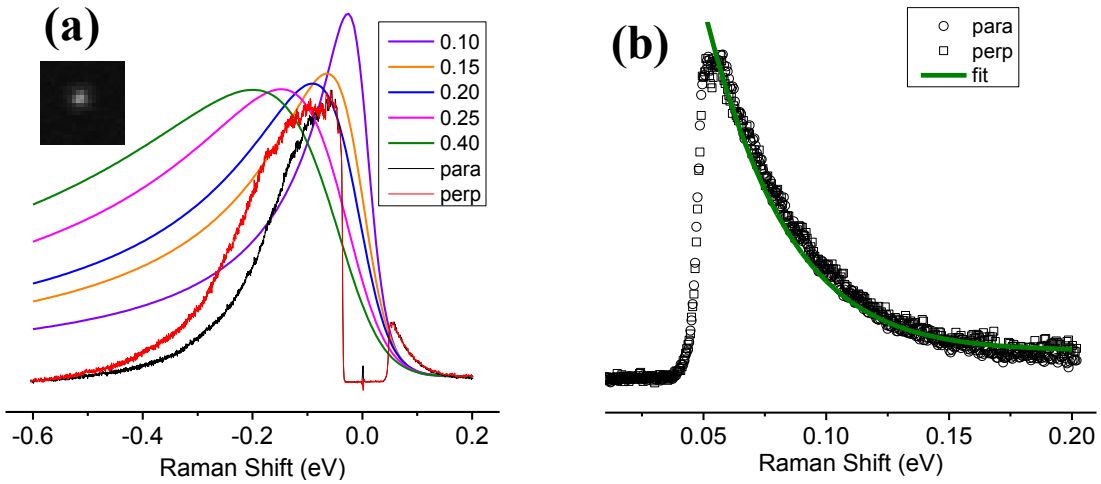

Figure 4.1: (a) Raman from a single gold particle (inset) parallel (red) and perpendicular (black) to excitation polarization. Plasmonic background according to eqn. 4.3 for the correlation function α_{mn} being Lorentzian is also shown as a reference with corresponding line-width listed in the panel. (b) With a scaling factor the anti-Stokes wing of the spectrum is best reproduced for $\Gamma = 0.4$ with some scaling factor, however comparison with (a) reveals this fit will miss the Stokes wing of the spectrum by far.

cannot be brought to zero by any power law – the matrix element (eqn. 4.3) must decay exponentially with the energy separation between states. Indeed, were we to make this assumption, then independent of any assumed density of states, a simple form defines the Raman spectral profile:

$$W(\mathcal{E}) \propto I_i I_s \int f(E)\big(1 - f(E+\mathcal{E})\big) e^{-|\mathcal{E}/\Delta|} dE \qquad 4.5$$

The comparisons in Fig. 4.2 illustrate that this form can be used to fit the data, with an extracted energy decay range of $\Delta \sim 0.08\ eV$. The suggestion is that the coherence between electron and hole states decays exponentially with their separation in energy. While this seems amenably reasonable, we consider whether the effect is spatial or dynamical in origin, i.e., whether it arises from the spatial matrix element in eqn. 4.1 or the dynamical correlation, which is hidden in the delta function.

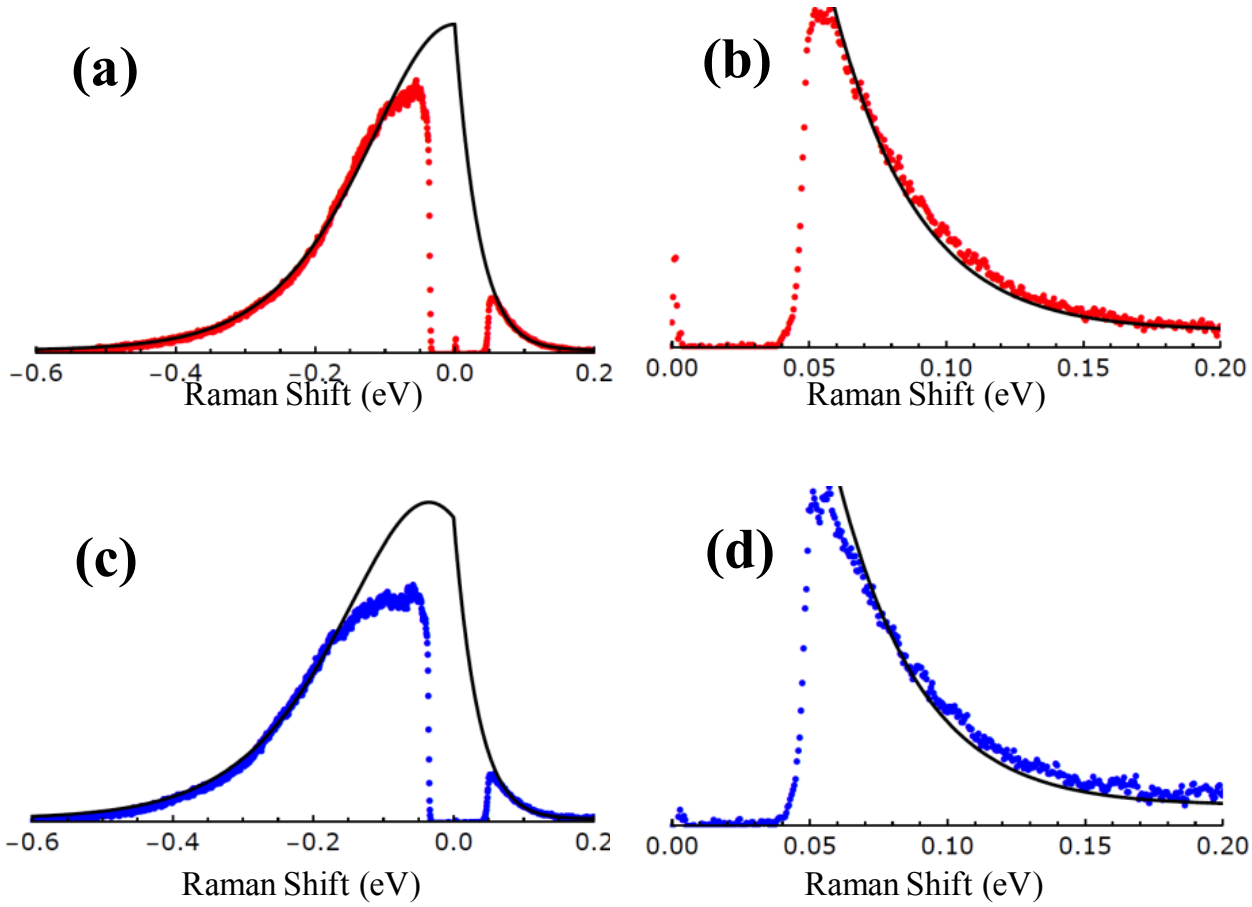

Figure 4.2: (a, b) Both parallel (red) and perpendicular (black) channel of Raman from the single gold particle can be fitted (black) simultaneously to eqn. 4.3 using exponential correlation function as in eqn. 4.5. (c, d) Detailed anti-Stokes wing of the spectrum and corresponding fit is shown. Fitting parameter: Δ_S = 0.070 eV, T_S = 420 K; Δ_{AS} = 0.078 eV, T_{AS} = 384K.

The outline of the spatial correlation argument was already made above. In effect, the orthogonality of k-states can only be realized when their overlap integral is carried out in full, [-∞ ,∞]. Since we are interested in states with that terminate on the image potential, which deviate significantly from strict k-states on their turning points, it is important to explicitly consider the

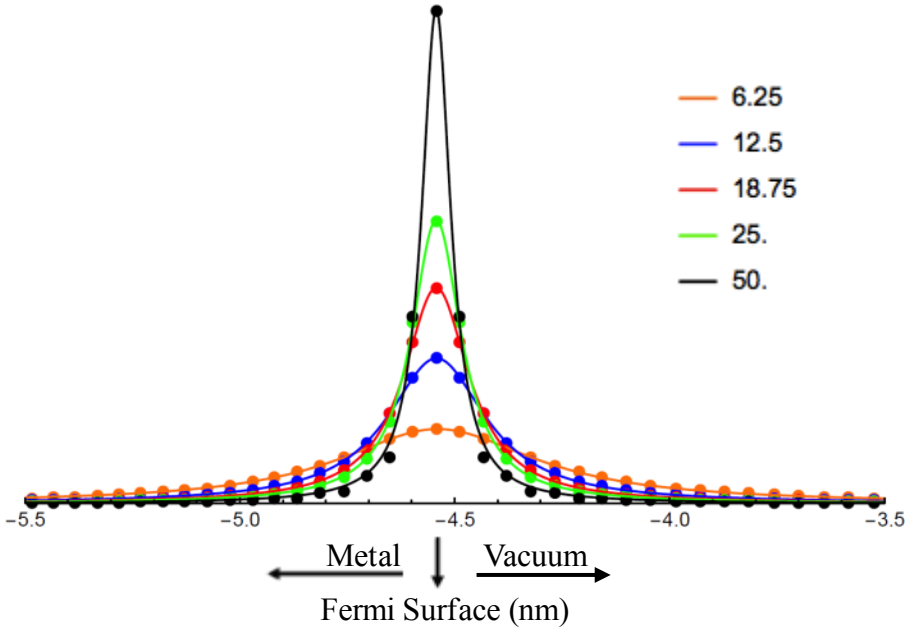

Figure 4.3: The overlap integral as a function of penetration depth (inset) using 1D wavefunctions that terminate on an image potential is Lorentzian. The overlap becomes more localized at the surface as penetration depth or damping length scale increases.

evaluation of the integral in eqn. 4.5. To this end, we compute the 1D wavefunctions that terminate on the image potential (see fig. 4.3), and we explicitly evaluate their overlap integrals subject to a damping (penetration) length scale, *1/q*:

$$M_{eh}(\mathcal{E}) = \int_0^\infty e^{-qz}\, \varphi^*(E+\mathcal{E}, z)\varphi(E, z)dz \qquad 4.6$$

The resulting function is shown for several choices of q. In all cases the spatial correlations fit to a Lorentzian as in eqn. 4.4, rather than an exponential as in eqn. 4.5. The dependence of the energy width of the Lorentzian on the damping length, 1/q, is shown in fig. 4.4. Note, at lengths of 20-40 nm, which is the accepted skin depth of gold,[3] the energy width of the correlation is $\Gamma \sim$ 0.17 eV, and this number should be compared with the Δ value obtained from the experimental fit to eqn. 4.5. Despite the different forms of the expressions, the energy widths are well motivated by either Landau damping time or a penetration length scale. However, this explicit treatment confirms eqn. 4.4 rather than justifying eqn. 4.5. It appears that the picture of single particle excitations is not an accurate representation of the observed Raman spectra.

The failure of the treatment may be traced to the assumption of phase coherence between the electron-hole states in evaluating M_{eh} through a strictly spatial overlap. Dynamical scattering between particles requires that the random phase approximation (RPA) be made in correlations between states. The reproduction of the spectra using eqn. 4.5 leads to the important conclusion, that the phase correlation between states decays as a function of their energy separation, with decay constant of ~ 0.10 eV. Alternatively, the exponential correlation between electron and hole states may be taken to indicate that rather than scattering within the metal half-space, with the evanescent field, the observed scattering process is dominated by the external field and surface states alone.

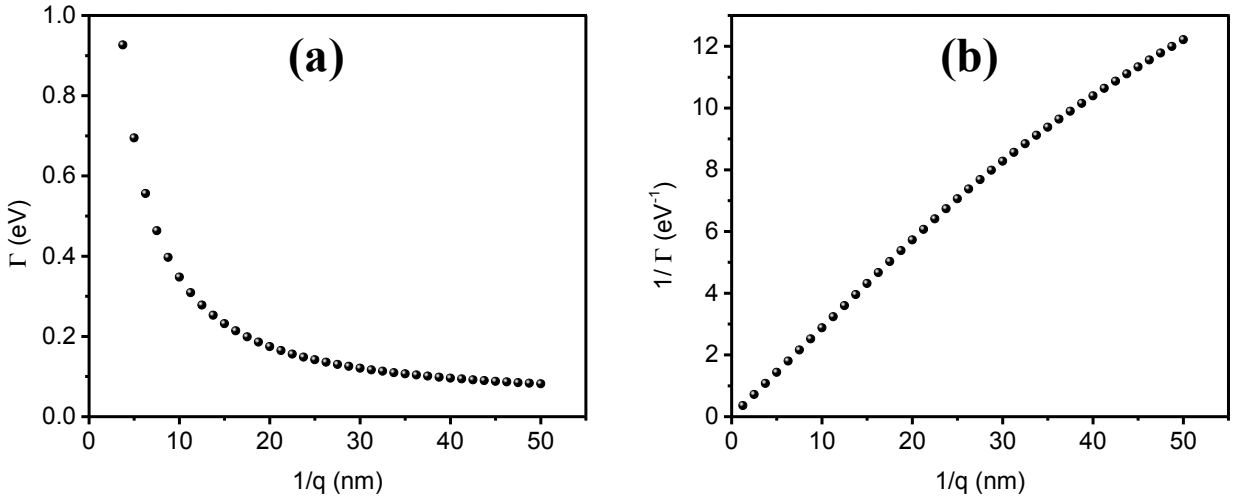

Figure 4.4: (a) The energy width of the Lorentzian (Γ) is inversely proportional to exponential damping length, 1/q. (b) 1/Γ vs. 1/q is almost a straight line through the origin. The minor change on slope may be associated to the artifact of restricting the calculation only to the surface states.

.

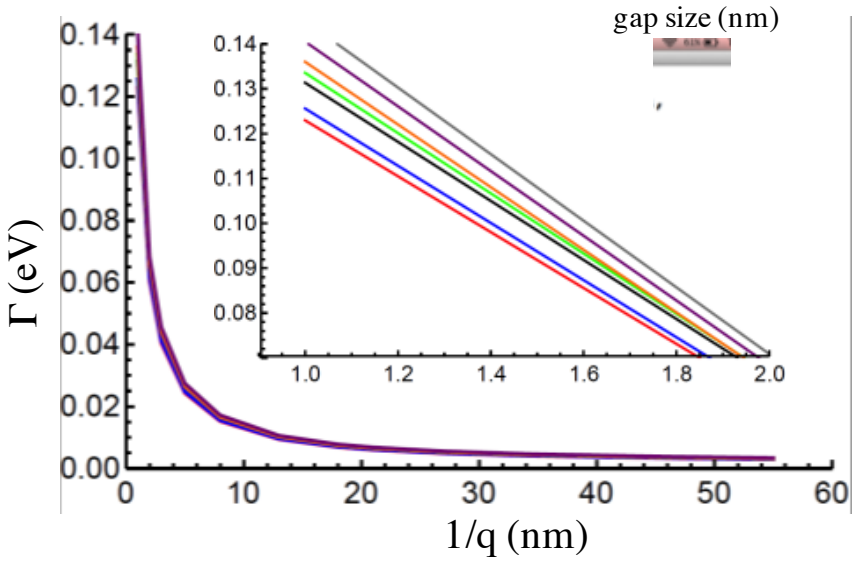

Figure 4.5: (a) The energy width (Γ) vs. damping length, 1/q. for variable gap-size, (inset) increase in gap size of a metallic junction increases the energy width as well.

So far, calculations have been performed on a metal vacuum edge. The energy width Γ = 0.07 eV as seen in Raman from single metal particle is decent match according to the modeling. However, we are mostly interested on metal-metal junction. In Fig. 4.5 we find that the energy width does dependence on penetration depth is a very slow function of gap size. We observe Γ = 0.07 eV for single metal particle however, ~ 0.2 eV suits better for the dimers.

The anti-Stokes scattering spectrum perfectly fits eqn. 4.5. The function, $S_{AS}(\delta\varepsilon;\ kT, \alpha, \varepsilon = \varepsilon_m - \varepsilon_n)$, is given in integral form, and as such is not very convenient for direct parametric fitting of the data. In fig 4.6 (b), we show its plot for several different values of kT, and for selected values of δ. The semilog plot makes it clear that the function is well approximated as an exponential, as is the anti-Stokes wing of the Raman spectra. The latter can be fit in the Boltzmann type equation, $S_{AS}(\omega) \propto \exp(-\hbar\omega/k_B T)$. We seek a transformation function between effective Boltzmann temperature (T_B) and real temperature (T). This is obtained by fitting the calculated Raman cross section, S_{AS}, at a given temperature, to the Boltzmann form. The transformation function is shown in fig. 4.6c.

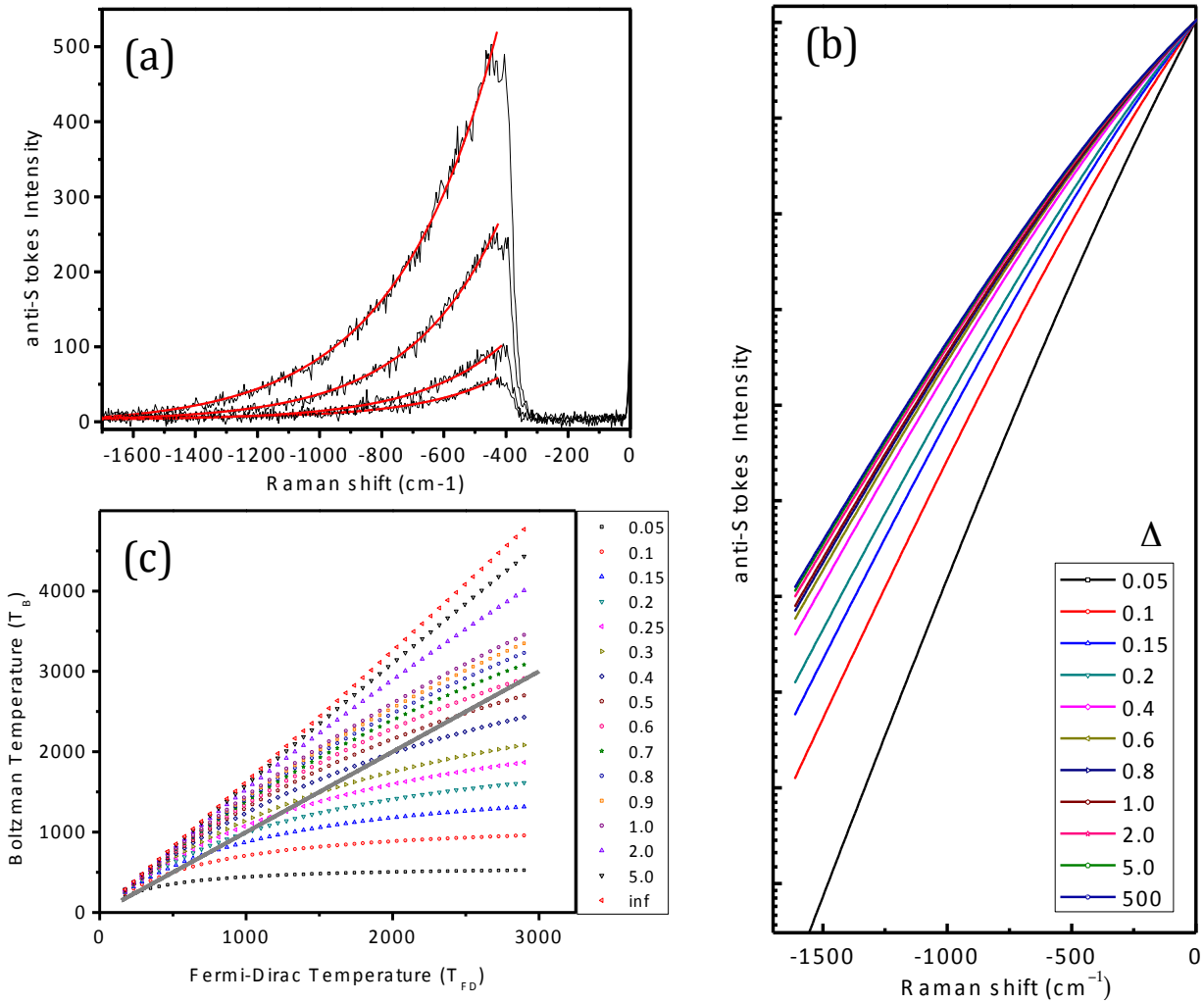

Figure 4.6: (a) Typical anti-Stokes wing of the Raman spectra from the nano-dumbbell (black) and decay rate of exponential fitting (red) gives the Boltzmann temperature (T_B). Panel (b) shows semilog plot of S_{AS} for few δ values as dictated by eqn. 4.5, and exponential fitting of S_{AS} can be used to connect T_B with Fermi-Dirac temperature (T_{FD}) as in panel (c).

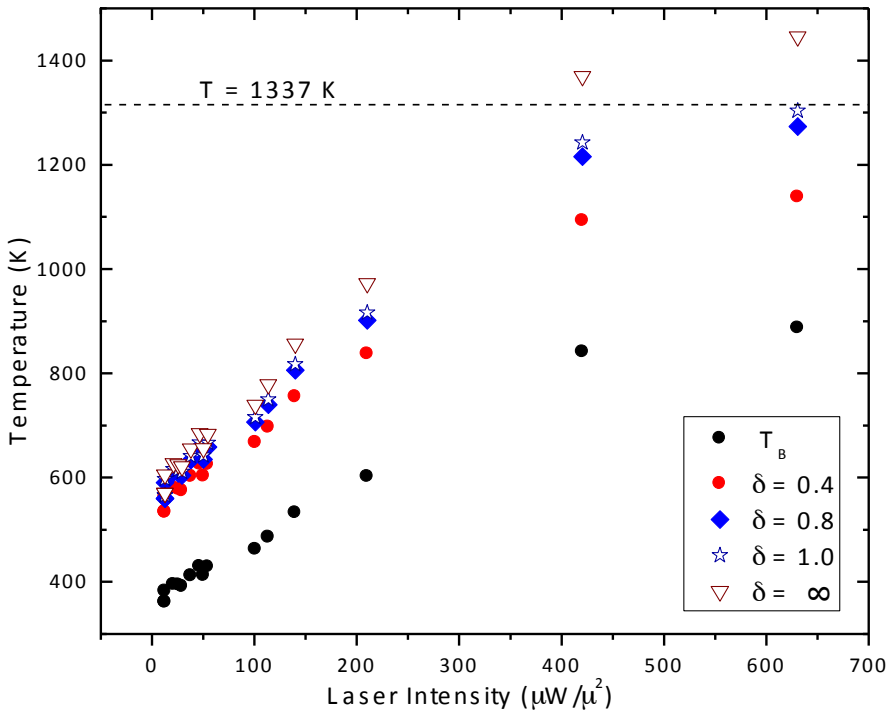

Figure 4.7: The experimental data fitted to exponential decay is measure of T_B (black dot). This temperature converted to more realistic T_{FD} according to the transformation found in Fig 4.6 (c) for δ = 0.4, 0.8, 1.0 and ∞ shows that δ = 0.2 is more appropriate for the range in use.

The implied temperature of the experimental data using this transformation is shown in fig. 4.7. The observed turnover in the T vs. I plot, which we associate with the melting of the gold dumbbell appears at T = 600° C, to be compared with the known melting temperature of 1064° C. The sensitivity of the transform to different values of δ is useful to establish whether the model is well determined. Based on the criterion of the melting point, we see that δ = 0.2 is a better fit. Given the approximations made, and the rather soft criterion for the goodness of the fit we can conclude that the surface states of the electrons primarily account for the observed Raman scattering,

4.5 Concluding Remarks

The more compelling finding in this chapter is the assignment of the observed scattering continuum to Raman scattering of the plasmon, namely the coherent (polarized) collective surface states of the metal. The polarization analysis that we will show in the next chapter indicates beyond the dipolar plasmon, magnetic, quadrupolar and dichroic contributions are clearly seen on the dumbbell antenna. This provides the first clear rationale for seeing the same components in SERS spectra of molecules – where the antenna has multipolar character, it will amplify the multipolar elements of the molecular polarizability tensor.

4.6 References

(1) Etchegoin, P. G.; Le Ru, E. C.; Meyer, M. An Analytic Model for the Optical Properties of Gold. *J. Chem. Phys.* **2006**, *125*, 164705.

(2) Mukamel, S. *Principles of Nonlinear Optical Spectroscopy*; Oxford University Press, 1995; p. 268.

(3) Johnson, P. B.; Christy, R. W. Optical Constants of the Noble Material. *Phys. Rev. B* **1972**, *1318*.

CHAPTER 5:

Raman of a nanosphere dimer antenna and its molecular load: Multipolar SERS and electronic Raman of plasmons

5.1 Abstract

We report polarization-resolved Raman scattering studies on TEM characterized individual gold nanosphere dimers functionalized with bi-pyridyl ethylene (BPE). The measurements allow the characterization of multipolar electronic Raman scattering on the nantenna and surface enhanced multipolar vibrational Raman of the molecule. The polarizability matrix of the nantenna is determined by the joint angular distribution of parallel and perpendicular scattering. Typical asymmetries in structure lead to multipolar response on the putative dipolar antenna. The response can be described by expanding the field-matter interaction to second order in spatial dispersion, subject to a single scaling factor $\zeta_A = 0.5 = 2\pi\lambda_A/\lambda_0$, where $\lambda_A = \lambda_0/12$ is the effective wavelength of the nantenna. Chiral plasmons, both left-handed and right-handed, can be identified on structurally similar nantennas. While the polarization pattern of the molecular SERS identically follows its nantenna, the local vector potential sampled by the molecule is not related to the radiation in the far field. This is established by assigning the fluctuating spectra of the molecule, to multipolar vibrational Raman driven by local field gradients at the intersphere junction. A scaling factor can also be defined for effective confinement of light at the junction, $\zeta_J = k_J\langle r\rangle \sim 1$, by associating the local field gradient with the wavevector $k_J = |\nabla E|$. In effect, non-resonant vibrational Raman optical activity is enhanced by $\varsigma_J^2/\varsigma_0^2 \sim 2\times10^5$ over its long-wave limit, when driven by local fields of the

junction. While the silica encapsulated gold dumbbells maintain their gross shape under irradiation, the morphology of the junction evolves. Small atomistic variations in the junction lead to observable fluctuations in SERS and control the characteristics of the nantenna.

5.2 Introduction

Plasmonic nanostructures are extensively used as nano-antennas (nantenna) to couple far-field radiation to molecular receivers.[1–3] They generate large local fields by confining radiation on spatial scales much smaller than the diffraction limit of light. Among other applications, nantennas enable surface enhanced Raman scattering (SERS),[4,5] whereby single molecule sensitivity is reached.[6–10] The nano-analog of the Hertzian dipole antenna, a dimer of metallic nanospheres, is among the more commonly used designs for this purpose. As such, it has been the subject of extensive experimentation,[6,7,11–18] and numerical,[19–22] analytical[23–26] classical and quantum analysis.[27–30] Notwithstanding the attractive simplification of the plasmonic response of idealized metal spheres, in practice, the system is much richer. Model assumptions break down at the intersphere junction, which is the most critical functional space of the nantenna, where the highest fields and currents are generated. Moreover, at junction gaps of < 1 nm, quantum effects, such as tunneling plasmons, become important.[31–33] Therefore, sub-nanometer scale morphology, which is difficult to control or characterize experimentally, can dominate local fields on molecular scales. That junction structure on atomic scales matter, was illustrated in a theoretical analysis of sodium nano-dumbbells, which allow nearly exact *ab initio* calculations.[34] Experimentally, the rich photophysics of a real plasmonic junction was highlighted in a study of SERS on a silver dumbbell undergoing light induced fusion.[17] Magnetic and quadrupolar SERS, charge transfer plasmon driven Raman, (CTPR), and rectification of photocurrent recognized

through Stark shifted Raman, could be identified. These observations have important implications with regard to molecule-plasmon interactions and applications therein: Stark shifted SERS demonstrates photo-current rectification at optical frequencies,[35] proving the validity of the rectenna concept for solar energy conversion;[36,37] and serves as a probe of local fields on the nanoscale.[38] CTPR has been used to track the making and breaking of bonds[39] and inter-sphere contacts with quantized conductance.[40] More generally, CTPR provides a direct connection between junction current and light scattering. [41–43] Multipolar SERS probes local field gradients, which has been previously recognized as a major source of fluctuations in SERS spectra.[44,45] These findings rest on the scrutiny of the molecular SERS response, and the multipolar response emphasizes that the molecule is excited by the near-field of the nantenna, which can be dramatically different that the free propagating far field that excites the nantenna. In this regard, scant attention is paid to the polarization sustained on the nantenna, which mediates the coupling between near and far field. Here, we recognize that the background in our SERS is due to the electronic Raman scattering (ERS) on the nantenna, and he induced plasmon can be fully characterized through polarization resolved measurements. Remarkably, we show that chiral plasmons are launched with linearly polarized plane wave excitation on a nominally achiral structure. The simultaneously measured ERS of the nantenna plasmons and the molecular vibrational SERS allow scrutiny of the relation between the multipolar response of the nantenna and the multipolar SERS of the molecular receiver.

Magnetic dipolar (M1) and electric quadrupolar (E2) transitions of a molecule are weak in comparison to electric dipolar (E1) transitions when driven by free propagating optical fields. The ratio of M1/E1 = E2/E1 transitions scales as $\varsigma^2 \equiv |k\langle d\rangle|^2$, where in vacuum $k = \omega/c = 2\pi/\lambda$ and $\langle d\rangle$ is a molecular length scale (length of the transition dipole). In vacuum, the long-wave

limit applies $\varsigma_0^2 \sim 10^{-4} << 1$, which justifies the neglect of the spatial dispersion of electromagnetic waves $\hat{\varepsilon}e^{ikr} = \hat{\varepsilon}$ in describing light-matter interactions. As such, the observation of multipolar vibrational Raman on plasmonic nanostructures implies enhancements of order $\varsigma^2/\varsigma_0^2 \sim 10^4$ beyond electric dipolar SERS enhancement factors, which commonly reach 10^8. Such large enhancements can be expected to give access to new physical phenomena, such as access to spin forbidden dark states of matter and weak effects, such as surface enhanced Raman optical activity[46–48] and vibrational dichroism.[18,49] It is therefore valuable to understand the nantenna mediated coupling of molecular multipolar transitions to the far field.

We present polarization-resolved Raman measurements on individual gold nano-dumbbells, which are characterized with ~ 1 nm resolution through transmission electron microscopy (TEM). The experimental platform, gold nanosphere dimers functionalized with bipyridyl ethylene (BPE) molecules then encapsulated in silica shells (see Fig. 1), has been utilized in prior studies,[18,50,51] and most recently in time-resolved coherent Raman measurements.[52] The diameter of the gold nanospheres we use, L~100 nm, is optimal for radiative damping of plasmons.[53,54] This allows observation of electronic Raman scattering on plasmons of the nantenna. The simultaneously recorded electronic Raman of the nantenna and the vibrational Raman spectrum of its molecular load allows the dissection of the two-step coupling of the field in the far zone, $r >> \lambda$, with the static zone, $r << L < \lambda$, sampled by the molecule. We show that the fields in the two zones are not related. They can be characterized by two different scaling factors, ς_A^2 and ς_J^2, which can be associated with the effective confinement of light on the nantenna and at the junction.

SERS on plasmonic structures is invariably accompanied by a background, the origins of which have been extensively deliberated.[55–61] A variety of scattering processes may contribute to

the background in different experimental systems and arrangements. Based on the shape dependent polarization of the scattering, the background continuum we see on individual gold nano-dumbbells can be readily assigned to Raman scattering on plasmons. Both dipolar and quadrupolar plasmons can be identified by their polarization patterns. This is understood by the fact that the long-wave limit does not apply to the nantenna. At optical wavelengths, for a nantenna of effective length $<L>$ ~ 100 nm, the scaling factor reaches unity $\varsigma_A^2 \sim 1$. Therefore, in addition to Raman driven by the local third order susceptibility, $\chi^{(3)}$, in which all four field interactions are dipole coupled to the far field; nonlocal response coupled through multipolar transitions and field gradients contribute (see Fig. 1). We show that Raman polarization patterns of the nantenna can be understood by expanding the response to second order in spatial dispersion, $R^{(2D)}$, with incident fields given as $(1 + ikz)\hat{\varepsilon}_i$ while retaining scattered fields as dipolar, $\hat{\varepsilon}_s$. The $R^{(2D)}$ response contains inseparable terms of electric dipole (d), magnetic dipole (m), electric quadrupole (q) and the cross term $<md>$ of dichroism, which implies excitation of chiral plasmons. Both left-handed and right-handed response can be seen on dumbbells that are only distinguished by structural asymmetries typical of real nanospheres.

In the single molecule limit, the tensor nature of Raman scattering is at full force. In contrast with bulk measurements where the vibrational Raman spectrum is characteristic of the molecule under study, in the single molecule limit the spectral intensity pattern depends on the relative orientation of the molecule and the applied field and its gradients. Given a reliable polarizability tensor of the molecule, in principle, it is possible to deduce the vector potential that generates a particular vibrational intensity pattern.[17,62] We show that the polarization patterns of the molecular lines follow those of the nantenna, even when the scattering involves manifestly different multipoles. The molecule samples local fields and field gradients driven by

displacement currents confined to the junction, and real currents driven by charge transfer plasmons. Hallmarks of the latter process are dramatic enhancement in SERS intensity and coalescence of line-spectra into band-spectra.[17,63] The controlling sub-nanometer morphology of the junction, which evolves under irradiation, remains illusive. Nevertheless, it is possible to cast the fluctuating spectra in $R^{(2D)}$ response, to extract a single scaling parameter, $\varsigma_j = k_l\langle r\rangle$, that characterizes the local field gradients, $k_l = |\nabla E|$, which control the intensity of multipolar Raman scattering.

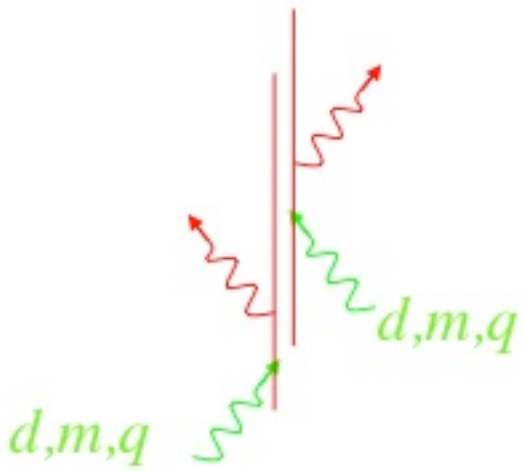

Figure 5.1 Feynman diagram of Raman scattering, showing the time ordered response, R_3, that distinguishes Raman from luminescence.[64] The local response pertains to all fields being coupled through electric dipoles (d), while the nonlocal response to second order in spatial dispersion couples two of the fields through electric dipole (d) magnetic dipole (m) and quadrupole (q).

5.3 Experimental

The experimental set-up is shown in Fig. 2. A λ/2-plate is used to rotate the polarization of the vertically polarized incident laser. The effect of the plate is to rotate the incident polarization by an angle 2φ, relative to the fast axis of the plate. This is equivalent to reflection of the field through the plane formed by the fast axis and propagation direction, $k = z$. The backscattered Raman that we collect passes through the same plate. Since the propagation direction is reversed, $k = -z$, the rotation is reversed. Accordingly, independent of the rotation angle of the λ/2-plate plate, which determines the direction of the polarization impinging on the sample, the double-pass geometry ensures that back-scattered Raman with polarization parallel to the excitation field appears vertically polarized (v), while perpendicular scattering appears horizontally polarized (h). After passing through the notch filter, a beam displacer is used to spatially separate the parallel and perpendicular components of the scattered light, followed by dispersing them on a 0.75-m monochromator (Shamrock 750, Andor) and simultaneously recording the spectra on a ccd array (Newton, Andor). We use a microscope objective with NA = 0.65 to attain an overall extinction ratio of 100:1. To the extent that Raman scattering $|\langle\hat{\boldsymbol{\varepsilon}}_s \cdot \boldsymbol{\alpha} \cdot \hat{\boldsymbol{\varepsilon}}_i\rangle|^2$ can be described in terms of transverse incident and scattered electric fields, $\hat{\boldsymbol{\varepsilon}}_{i,s}$, it is characterized by the 2X2 polarizability matrix $\boldsymbol{\alpha}$. With incident field linearly polarized along ϑ, the simultaneously recorded maps of the parallel and perpendicular polarized scattered radiation over $\vartheta \in [0,2\pi]$ uniquely determine $\boldsymbol{\alpha}$. This can be verified by noting that the state of polarization is completely specified by the Stokes vector, $\boldsymbol{S}$, whose elements are the projections of the Pauli spin matrices, $\boldsymbol{\sigma}_i$:

$$\boldsymbol{\alpha} = \frac{1}{2}\sum_{i=0}^{3} S_i \boldsymbol{\sigma_i}$$

Both spin matrices and their squares generate an orthogonal representation in the two-channel measurement; as such, allow determination of the polarizability matrix. This is explicitly shown in the appendix.

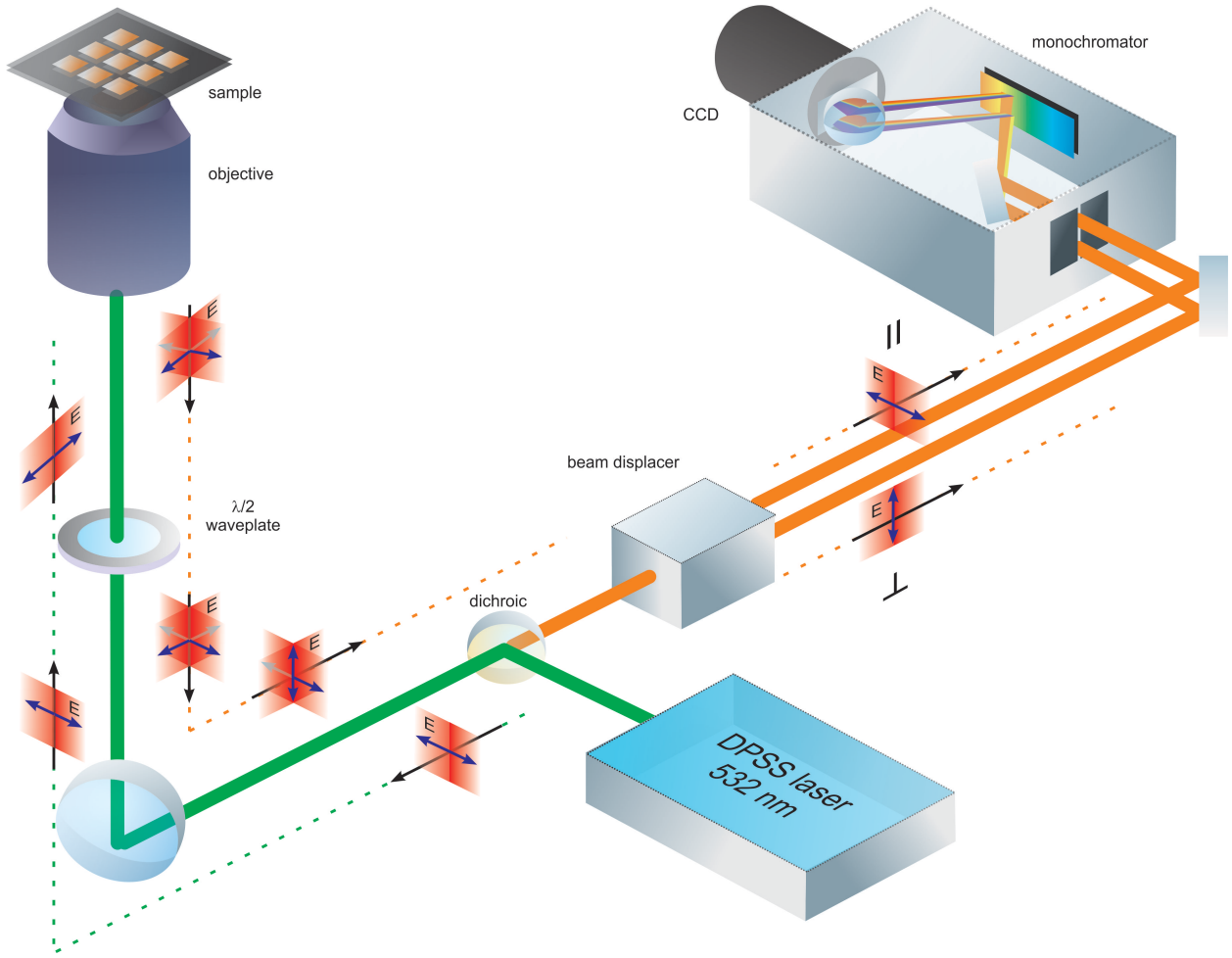

Figure 5.2: Experimental arrangement for polarization mapping of Raman scattering on single nano-dumbbells. We use a 0.75-m grating spectrometer equipped with cooled CCD, (BD) β-BBO beam displacer, (NF) notch filter, (λ/2) half-wave plate, (PD) photodiode used with removable glass beam-splitter for backscatter imaging. The setup allows rotation of the polarization of the linearly polarized laser, and the simultaneous recording of parallel and perpendicular components of the back-scattered Raman in the v- and h-displaced channels.

The measurements are carried out on *trans*-1,2-bis(4-pyridyl)-ethylene (BPE) functionalized gold nanosphere dimers (dumbbells) that are encapsulated in porous silica. The characteristic sphere diameter is 100±5 nm and the typical SiO_2 shell thickness is 70±5 nm. TEM images prior to irradiation show a typical junction gap of ~1 nm. Invariably, post-irradiation images show necking at the junction. The apparent necking is caused in part by the high energy electrons used to obtain high-resolution images. And although the contrast in the TEM images is reduced by scattering on the silica shell, close-ups of post-irradiated junctions invariably show metal junctions that are jagged on nm-scale. The measurement protocol is predicated by the fact that TEM measurements damage organic matter. It consists of: a) SEM mapping of the drop cast sample on a TEM grid, b) re-mapping the sample on the microscope using back-scattered light and matching the two maps, c) polarized Raman measurements on individual spatially isolated dumbbells, d) TEM characterization of the nanostructures on which SERS measurements were conducted. SEM allows characterization of structure with a resolution of ~5 nm, sufficient to establish the absolute orientation of the nanodumbbells.

5.4 Result and Analysis

The typical measurement on a single dumbbell is illustrated in Fig. 3. It consists of recording complete spectra at incident polarization angles between 0° and 360°, with 2° intervals, over the course of 2 hrs total acquisition time. The angle/time dependence of the spectral intensity presented in (Fig. 3c,d) shows, in addition to the angular modulation, a slow monotonous decay of the overall signal. The evolution preserves the polarization pattern determined by the gross shape of the nantenna. We ascribe the slow variation in scattering intensity to evolution of the plasmon resonances at 532 nm, which is significantly removed from the binding dipole plasmon resonance that peaks near 800 nm.[29] At junction gaps of ~1 nm, plasmon resonances rapidly evolve with small variations in the gap.[33,65,66] Moreover, the local field is reduced when shunted by photoinduced tunneling currents. Accordingly, we associate the radiation induced monotonous decline in intensity across the spectrum with structural evolution at the inter-sphere junction (see close-up in Fig 3f). We fit the intensity for a given spectral segment to the joint variables, $I_i(\vartheta,t) = I_i(\vartheta)exp(-t/\tau_i)$, to extract the evolution corrected angular functions, $I_i(\vartheta)$. We consider three spectral components: a) background subtracted molecular lines, b) the blue wing of the continuum, integrated between Raman shifts of 1700 cm^{-1} and 1900 cm^{-1} c) the red wing of the continuum, integrated between 350 cm^{-1} and 550 cm^{-1}. The polar plots that will be presented are color coded accordingly.

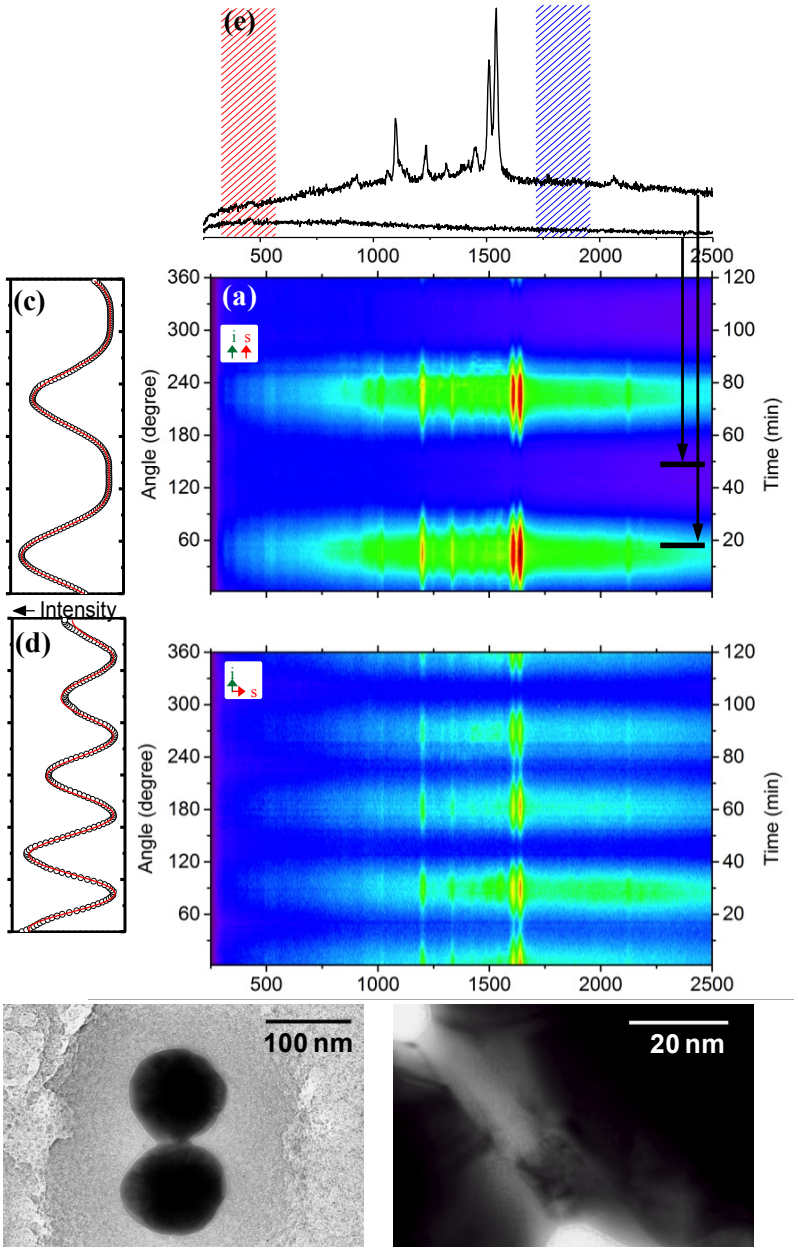

Figure 5.3: Raman spectra recorded as a function of excitation polarization angle/time: (a) parallel, (b) perpendicular scattering channels. Intensity profiles of The most prominent molecular line (1640 cm^{-1}) looses intensity over time (c,d) and the decay constant from exponential fit (red) will be used to correct all intensity profiles reported here-after. Spectral slices of characteristic Raman spectra and the range of the blue and the red wings of the continuum is shown in (e). TEM image (f) of the dumbbell from which the data was collected appear to be relatively spherical, however the junction (g) appears to have a narrow adjoining neck, which is only seen after irradiation.

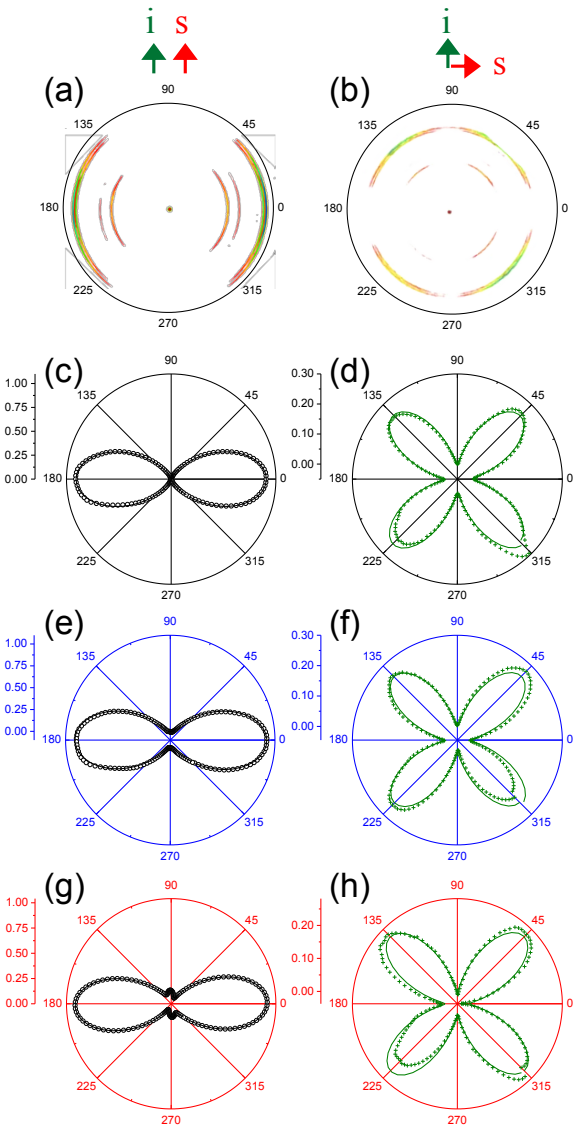

Figure 5.4: Polar plots of the line spectra in (a) parallel and (b) perpendicular scattering channels, (c,d) SERS of the vibrational line at 1640 cm^{-1}, (e,f) the blue continuum, (g,h) red continuum. The joint distribution functions in orthogonal channels are fitted by eq. 1, with the single normalization constant α_{xx}^2.

5.4.1 Dipolar nantenna

The background subtracted molecular SERS spectra as a function of incident polarization angle, are shown in the polar plots of Fig. 4a,b for the simultaneously recorded parallel and perpendicular scattering channels. All vibrational lines follow the same intensity pattern, which

is exemplified by the polar plots of the most intense line, in Fig. 4c,d. The response is determined by a single element of the polarizability matrix, α_{xx}, which leads to the joint polarization pattern (see appendix):

$$I^{\alpha_{xx}} = \begin{bmatrix} I_{\parallel}(\vartheta) \\ I_{\perp}(\vartheta) \end{bmatrix} = \alpha_{xx}^2 \begin{bmatrix} cos^4\vartheta \\ sin^2\vartheta cos^2\vartheta \end{bmatrix} \quad 5.1$$

The simultaneously recorded polarization patterns in the two orthogonal channels are fitted with the single normalization constant, α_{xx}^2, in Fig. 5.4. And, in reference to the SEM images, it can be established that *x* lies along the long-axis of the dumbbell, to within ~5°. Off-diagonal contributions α_{xy} in 5.1 would rotate the angular distribution, while any contribution from α_{yy} would add an isotropic component (would convert the figure eight of Fig. 5.4c into a peanut shape). All of the molecular lines obey 5.1. The molecular SERS appears to be driven by local fields that are coupled along the long axis of the dumbbell.

The joint angular distributions of the blue wing of the continuum, in parallel and perpendicular scattering channels, are shown in Fig. 5.4e,f. They are identical to that of the molecular lines. The continuous nature of the spectrum identifies its origin as electronic, its polarization identifies it as coherent scattering that recognizes the shape of the dumbbell, its Stokes shift distinguishes it from Rayleigh scattering, and the monotonous decay of the spectrum and its polarization distinguish it from inter-band fluorescence of gold. Also, the same background can be observed on bare dumbbells on which we find no molecular spectra. These observations are sufficient to assign the background to electronic Raman scattering of the nantenna, namely, Raman of the plasmon. This component of the electronic background reveals the susceptibility $\chi^{(3)} = \chi^{(3)}_{xxxx}$ of an ideal dipolar antenna. As such, the blue component of the

background can be assigned to Raman of the dipolar plasmon despite the fact that the excitation is far from the binding dipolar resonance.

The red wing of the continuum shows an additional, quadrupolar component in the parallel channel (Fig. 5.4g), but not in the perpendicular channel (Fig. 45.h). This observation is sufficient to identify the additional scattering term by the Pauli $\boldsymbol{\sigma}_1$ matrix (see appendix):

$$\boldsymbol{\alpha} = \frac{a}{2}(\boldsymbol{\sigma}_0 + \boldsymbol{\sigma}_1) + b\boldsymbol{\sigma}_1 = \begin{bmatrix} a+b & 0 \\ 0 & -b \end{bmatrix} \tag{5.2}$$

with associated joint angular distribution:

$$\begin{bmatrix} I_{\parallel}(\vartheta) \\ I_{\perp}(\vartheta) \end{bmatrix} = \begin{bmatrix} \left(acos^2\vartheta + b(cos^2\vartheta - sin^2\vartheta)\right)^2 \\ a^2cos^2\vartheta sin^2\vartheta \end{bmatrix} \tag{5.3}$$

The patterns in the two channels in Fig. 5.4g,h are simultaneously reproduced using 5.3. The extracted ratio of the two contributions, *b/a = 2/3*, shows significant variation, $0 \leq b/a \leq 5$, on different nantennas. We assign this spectrally distinct component to Raman scattering on the quadrupolar plasmon. The quadrupolar spectrum, which can be isolated at $\vartheta = 90°$ in the parallel channel, is shown in Fig. 5.3e. Remarkably, it does not show any molecular lines. Despite the fact that the scattered field intensity by the quadrupolar plasmon can be the dominant term on different nantennas, the molecular SERS is only broadcasted by the dipolar plasmon. It is useful to note that $\boldsymbol{\sigma}_1$ is the Jones matrix of the half-wave plate; as such, it can be recognized that the quadrupolar plasmon leads to Raman optical activity – it rotates the polarization of the scattered field by 2ϑ relative to the incident field.

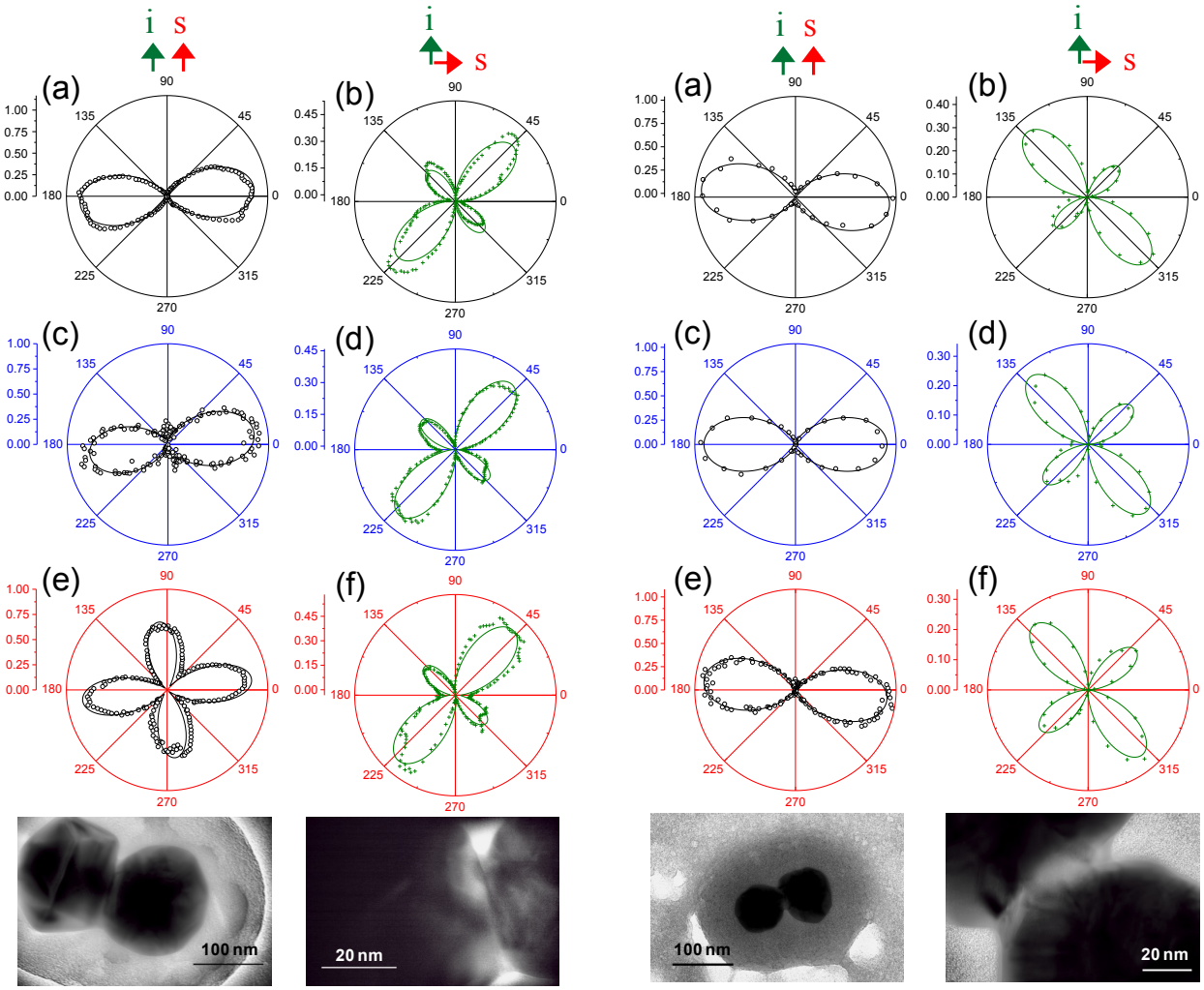

Figure 5.5/5.6: Nonlocal response: Scattering in the parallel (right column) and perpendicular channel (left column) of the molecular SERS (a,b) and the electronic background continuua blue (c,d) and red (e,f). The fits (solid) are to eqn. 5.6. High resolution TEM images (g,h) reveal faceting and deviation from ideal sphericity.

5.4.2 Chiral plasmons:

The same set of measurements, carried out on seemingly similar dumbbells, under similar conditions, is presented in Fig. 5.5-6. In distinct contrast with particle 1 (Fig. 5.4), the scattering on these particles shows broken symmetry. To the extent that the dumbbell has uniaxial symmetry, ignoring asymmetry introduced by irradiation along the z-axis, the material response should be symmetric with respect to reflection through any plane that contains the principle *x*-axis of the dumbbell. The horizontal axis of the maps in Fig. 5.4 are aligned with the x-axis. Clearly, the distributions in the perpendicular scattering channel of Fig. 5.5/6 b,d,f, are not symmetric with respect to reflection about the x-axis. We see that the principle scattering poles are rotated relative to the long axis of the nantenna by approximately +45° on particle 2 and -45° on particle 3. The patterns in the parallel channel are also tilted. The broken symmetry implies odd parity, characteristic of magnetic dipoles. The signed rotation of the polarization patterns identify chirality with opposite handedness on particles 2 and 3. Remarkably, the polarization patterns of the molecular lines follow those of the electronic background (see Figs. 5 & 6, panels b, d, f). Inspection of the TEM images reveals that the nanospheres in the dipolar nantenna are rounded and similar in size (Fig. 3f,g), while nantennas with multipolar response are more asymmetric: the nanospheres in particles 2 and 3 are more facetted and are unequal in size (Fig. 5.5g, h & 5.6g, h). Of the seven nanosphere dimers that were investigated in detail, particle 1 was the only one that showed strictly dipolar response. It appears that typical deviations of nanospheres from sphericity is sufficient to induce chiral response and to impose definite handedness, which is not trivially obvious by inspection of the shapes conveyed by the TEM images.

The observed polarization patterns in Figs. 5.5/6 can be obtained in Raman scattering by taking retardation into account, by expanding the two incident fields to first order in spatial dispersion. In effect, the long-wave limit, which allows the assumption of instantaneous field-matter coupling $\hat{V} = A_0\hat{\varepsilon}\cdot\nabla$, does not hold for excitation of the nantenna. It is necessary to include the spatial dispersion of the vector potential, $\hat{V} = A\cdot\nabla = A_0\hat{\varepsilon}e^{ikr}\nabla$. Note, four wave interactions $\langle\hat{V}_i^*\hat{V}_s^*\hat{V}_s\hat{V}_i\rangle$ describe the Raman process, two fields each to describe an incident (*i*) and scattered (*s*) photon. Expanding the incident plane wave to first order along its *z*-propagation axis, $e^{ikz} = 1 + ikz$; and limiting electric and magnetic dipoles to the long axis, the interaction of two fields $\hat{V}_i^*\ \hat{V}_i$ generates the four coupled terms (see supporting material):

$$\langle(1+ikz)\big(\partial_x+\partial_y\big)\rangle^2 = \omega^2\langle d_x\rangle^2 + k^2\langle m_x\rangle^2 - 2\omega k\langle d_x m_x\rangle + \omega^2k^2\langle q_{xz}\rangle^2 \qquad 5.4$$

namely, electric dipole, magnetic dipole, dichroic and quadrupolar transitions, in order. Then, to second order in spatial dispersion, (2D), the angular functions in the parallel and perpendicular channels can be transcribed from (4):

$$I^{(2D)}(\vartheta) = \begin{bmatrix} I_{\parallel} \\ I_{\perp} \end{bmatrix} \propto [(\omega|d|\cos\vartheta - k|m|sin\vartheta)^2 + \omega^2k^2|q|^2cos^2\vartheta]|d|^2\begin{bmatrix} cos^2\vartheta \\ sin^2\vartheta \end{bmatrix} \qquad 5.5$$

In the long-wave limit, $k \to 0$, we retrieve the local response 5.1. The nonlocal terms in (5) scale as $\langle kz\rangle \equiv \zeta_A$. This is clarified by the substitutions $|d|$ = <*ex*>, $|q|$ = <*exz*>, $|m| = \omega$ <*exz*>/2, to express the joint distributions in orthogonal polarizations (5) as a function of the single scaling variable:

$$I^{(2D)}(\vartheta) \propto [(\cos\vartheta - \zeta_A sin\vartheta/2)^2 + \zeta_A^2 cos^2\vartheta] \begin{bmatrix} cos^2\vartheta \\ sin^2\vartheta \end{bmatrix} \quad 5.6$$

With the exception of the parallel channel in the red wing of the continuum on particle 2 (Fig. 5e), the observed polarization patterns on particle 2 and 3 can be reproduced by the joint polarization distribution (6). The orthogonal pairs of polarization patterns – relative amplitudes, rotation, and angular distribution – are simultaneously reproduced with the single fitting parameter ζ_A, and normalization constant to convert (6) into equality. We find $\zeta_A \approx -0.5$ on particle 2, while it shows a spread on particle 3: $\zeta_A \approx 0.4$ for molecular lines and $\zeta_A \approx 0.15$ and 0.25 on the red and blue wings of the continuum. The sign of ζ_A accounts for the reversal of the relative rotation of polarization patterns in parallel and perpendicular channels seen on particles 2 and 3 (Fig. 5.5 versus Figs. 5.6). The sign, which is carried by the dichroic term $\langle d_x m_x \rangle$ in (5), determines the helicity of the excited plasmon; namely, by the relative phase between the time-harmonic, coaxial electric and magnetic dipole and their associated electric and magnetic fields. Clearly,, the handedness of the helical plasmon is reversed on the two particles. While deformation of the nanosphere is essential to couple the linear (electric dipole) and angular (magnetic dipole) oscillation of the surface charge density wave on the dimer, the structural feature that determines the sense of helicity is not obvious in the TEM images. A sign change in the chiral response could be associated with the location of the magnetic resonance relative to the excitation wavelength;[67] which in turn, must be determined by a subtle structural difference.

The parallel scattering channel in the red wing of the electronic background (Fig. 5.5e) reveals a magnified version of the quadrupolar plasmon seen on particle 1 (Fig 5.4g). While a smaller contribution there, here, it is the dominant term that acts as an independent channel:

$$I(\vartheta) = aI^{(2D)}(\vartheta) + bI^{\sigma_1}(\vartheta) \qquad 5.7$$

with relative weight b/a ≈ 5/1. Since at 90° the parallel channel isolates the quadrupolar plasmon, it is possible to decompose the electronic spectrum into quadrupolar and dipolar components, as in Figure 3. The discrepancy in the parallel channel between molecular lines and red continuum (Fig. 5a and 5e) is another illustration of the decoupling between quadrupolar plasmon and SERS. The converse of this consideration, that SERS is enhanced through the dipolar radiative plasmon, and the consistent reproduction of the dataset with minimal parametrization, confirm the $R^{(2D)}$ scattering scheme: the excitation of the plasmon is governed by the dispersive nonlocal interaction, while the radiation is dipolar.

It is useful to consider the states responsible for the magnetic and dichroic response. Using the well established hyberdization mode, if we limit the plasmon of the dimer to hybrids constructed of the $l = 1$, $m_l = 0, \pm 1$ monomer states, then ithe dimer states are $\Lambda = 2,1,0$ with $M = \Lambda, \Lambda\text{-}1,..- \Lambda$ where is the projection along the x-quantization axis. The dipolar response arises from a transition to $|m_l=0\rangle_1 \pm |m_l=0\rangle_2$ states, namely, to the binding or anti-bonding dipolar plasmon (not allowed in a perfectly symmetric dumbbell). The dichroic response arises from a transition to L = 2, M=1 state, while the magnetic transitions are to the in phase and out of phase circulation L = 2, M=0,±2. Note, in small nanospheres, d< 40 nm, the transverse excitations are strictly limited to qudrupoles. However, in larger spheres, due to retardation, states with angular momentum become accessible.

5.4.3 Molecular multipolar SERS:

The joint polarization distributions, which define the multipolar scattering mechanism and susceptibility of the nantenna, have no information about the scattering mechanism or the polarizability of the molecule. That information is contained in the SERS spectra. We show in Fig. 7 the vibrational Raman spectra of the molecule observed on the dipolar nantenna . The spectrum remains stationary during the acquisition of the data, during several hours of irradiation at an intensity of 50 $\mu W/\mu m^2$ (see Fig. 3a,b). Save for their overall intensities, the spectra observed in parallel and perpendicular channels are indistinguishable. They can only be reproduced by the normal Raman spectrum of BPE if we assume the long axis of the molecule to be tilted by 40°-60° relative to the field. This is illustrated in Fig. 5.7. For a molecule aligned with the long axis of the nantenna, the parallel channel yields the observed spectrum; however, the spectrum in the perpendicular channel is two orders of magnitude weaker and the pattern is very different. The difference in intensities reflects the strong anisotropy of the polarizability tensor, $\boldsymbol{\alpha}' = d\alpha/dq$, which is common to aromatic molecules where the polarizability ellipsoid of the bright modes is dramatically stretched along the long conjugation x-axis. To see the same spectrum with comparable intensities along orthogonal channels, the molecule must be locked at the magic angle. While plausible, this is a strong constraint under ambient conditions.

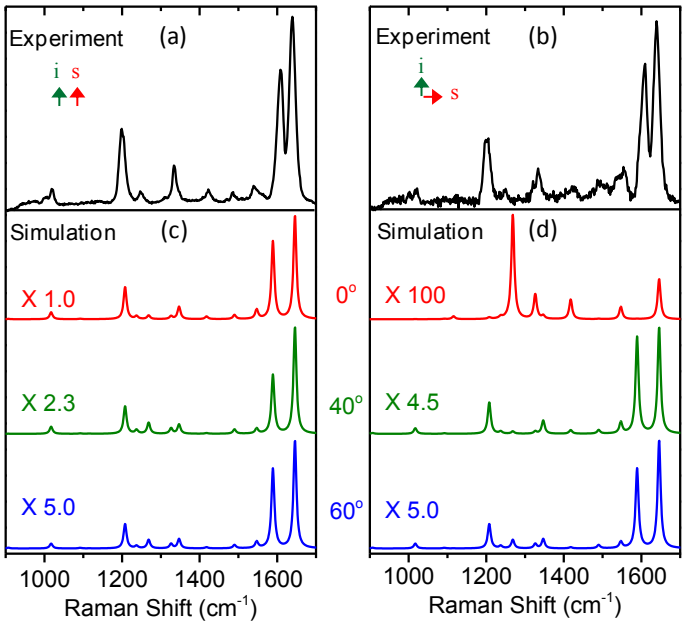

Figure 5.7: ***Parallel (a) and perpendicular (b) channel showing identical spectra on particle 1 (cuts from Fig 3).*** **Computed spectra at 0°, 40° and 60° for in plane molecular rotation with respect to its long axis. The experimental spectra are consistent with the normal dipolar Raman response of a molecule locked in orientation between 40° - 60° relative to the dumbbell axis.**

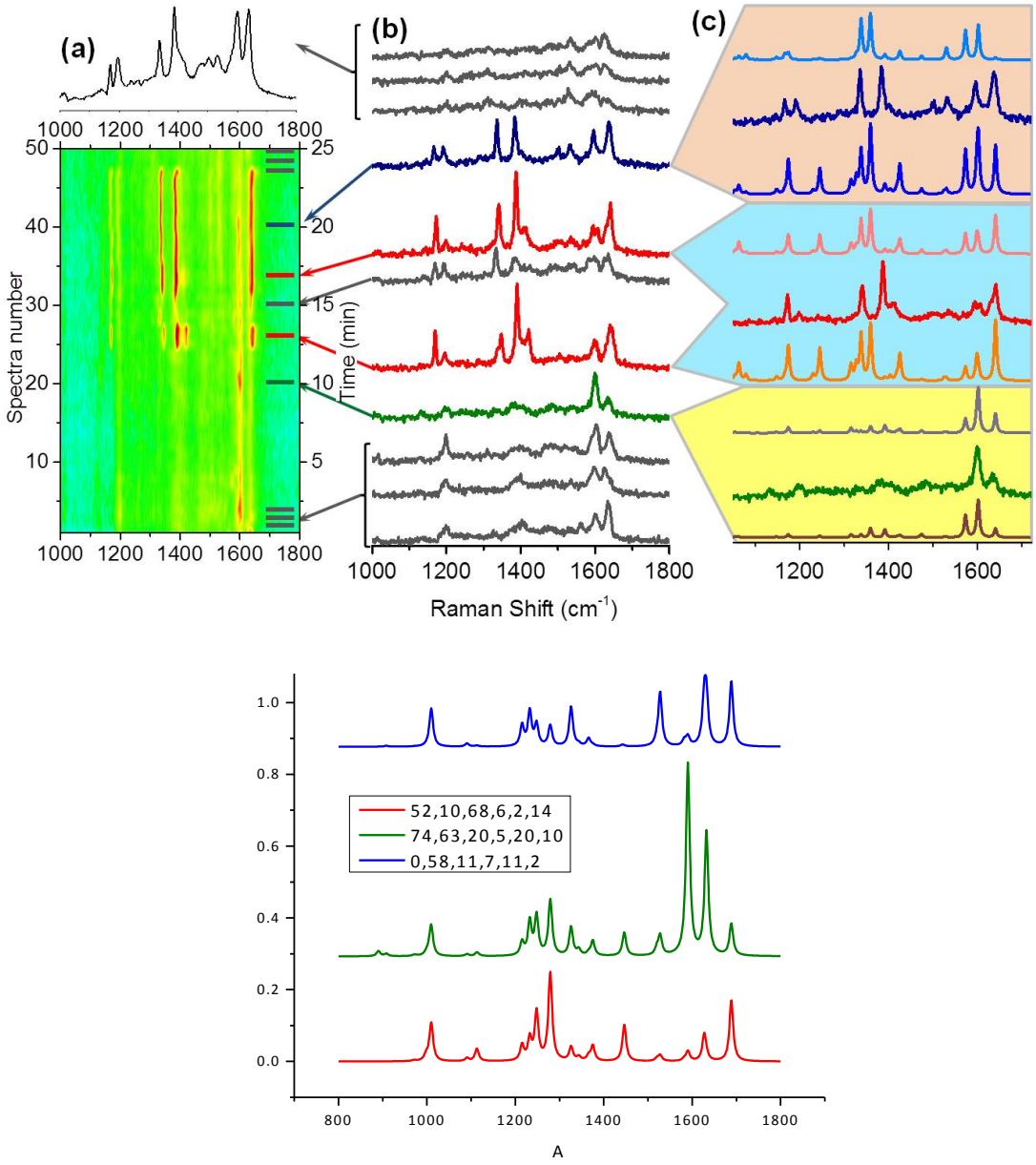

Figure 5.8: (a) Raman trajectory of particle 1 and a time integrated spectrum, (b) Sequentially recorded series of fluctuating spectra. Multipolar Raman formulation, eq. 8, qualitatively reproduces the observed spectral variations (c): at Euler angles {α, β, γ} = {0°, 57°, 34°} or {37°, 37°, 89°} for spectrum# 20 (blue), {56°, 16°, 72°} or {51°, 23°, 61°} for spectrum# 33 (red) and {52°, 35°, 77°} or {58°, 74°, 55°} for spectrum# 40 (green), where {0°, 0°, 0°} defines the direction in which unity {1,0,0} electric field is applied.

After continued irradiation of particle 1, the molecular spectrum starts to fluctuate. The spectrum obtained with an integration time of 250 s is shown in Fig. 8a, above the image plot of a trajectory constructed from spectra acquired with 10 s integration. Although, recurrences of the normal spectrum can be recognized at the beginning (spectra 1-3) and at the end of the trajectory (spectra 47-50), the selected spectra at intermediate times (spectra 20, 33, 40) reveal multipolar Raman scattering. The spectra can be understood, following the ansatz of the multipolar response of the nantenna (Eq. 6):

$$S^2(\alpha', \beta', \gamma') = \left(dd - \frac{a\zeta_J}{2} md\right)^2 + b^2 \zeta_J^2 (qd)^2 \tag{8}$$

where *α',β',γ',* are the Euler angles of rotation between molecular frame and nantenna, and the two fitting parameters (*a,b*) are now cast in terms of the junction scaling factor, ζ_J. The multipolar scattering tensors:

$$dd = \langle \varepsilon_s | \boldsymbol{\alpha'} | \varepsilon_i \rangle \tag{5.9a}$$

$$md = \langle \varepsilon_{s,\alpha} \left| \boldsymbol{G'}_{\boldsymbol{\alpha,\beta}} \right| \delta\varepsilon_{i,\beta} \rangle \tag{5.9b}$$

$$qd = \langle \varepsilon_{s,\alpha} | \boldsymbol{A}_{\boldsymbol{\alpha,\beta\gamma}} | \delta\varepsilon_{i,\beta\gamma} \rangle \tag{5.9c}$$

are evaluated using the polarizability derivative, $\boldsymbol{\alpha'}$, dichroism, $\boldsymbol{G'}$, and dipole-quadrupolar matrices, $\boldsymbol{A}$, computed with the ROA module of Gaussian 09,[68] and $\delta\varepsilon$ are evaluated for assumed local field gradient, $\partial E_\alpha / \partial \beta$. Since the computed matrices implicitly assume the long-wave limit, they are expected to be enhanced by, $\frac{\zeta_J}{\zeta_0} = \frac{k}{k_0}$, with effective wavevector determined by local field gradients $k_{\alpha\beta} = |E_\alpha^{-1} \, \partial E_\alpha / \partial \beta|$. The computed spectra, are for the unperturbed molecule, in C_{2h} symmetry. They are in general agreement with a prior analysis of the Raman, hyper Raman and IR spectra of BPE.[69] Due to the inversion symmetry of the molecule, the

normal modes occur in symmetric (g) and anti-symmetric (u) pairs split by 1-20 cm^{-1}, and the mutual exclusion of IR and Raman activity is obeyed. As such, the dichroic transitions that arise from the cross-term <*md*><*dd*> in (8), are absent. The construct is limited to magnetic and quadrupolar SERS driven by field gradients.

For the selected, commonly recurring, spectra in Fig. 8, we can find multiple acceptable molecular orientations for an assumed set of field-gradients, two of which are shown for each of the selected spectra in Fig. 9c. The possible matched orientations are spaced quite apart in Euler space, and minimizing molecular walk leads to a trajectory from {37°, 37°, 89°} through {51°, 23°, 61°} to {52°, 35°, 77°}. For this calculation, the initial assumptions are x-polarized excitation [1, 0, 0] and electric field gradient tensor $\frac{\partial E_i}{\partial j}$to be composed of only two terms: $\frac{\partial E_x}{\partial z} = 2$ and $\frac{\partial E_z}{\partial x} = 1$, which generates y-polarized magnetic field. Determination of molecular orientation comes from rotating the molecule to the specified Euler angle in the presence of above mentioned field and field gradients. Such a large motion appears unphysical, unless the local field experienced by the molecule is defined by an evolving nm-scale asperity in the gap. While the origin of the variation in local fields is indirectly inferred, the fits yield reliable estimates of the required enhancement of multipolar matrix elements. Acceptable fits are obtained for a/b = 15/4 and enhancement $\frac{\zeta_J}{\zeta_0} = \frac{k}{k_0} = \lambda/\lambda_e \sim 500$, which establishes the effective local wavelength $\lambda_e \sim 1$ nm. This is the key finding: field gradients on the molecular length scale are implied by the observation of fluctuation between dipolar and multipolar Raman.

5.4.4 Molecular spectra on the multipolar dumbbell:

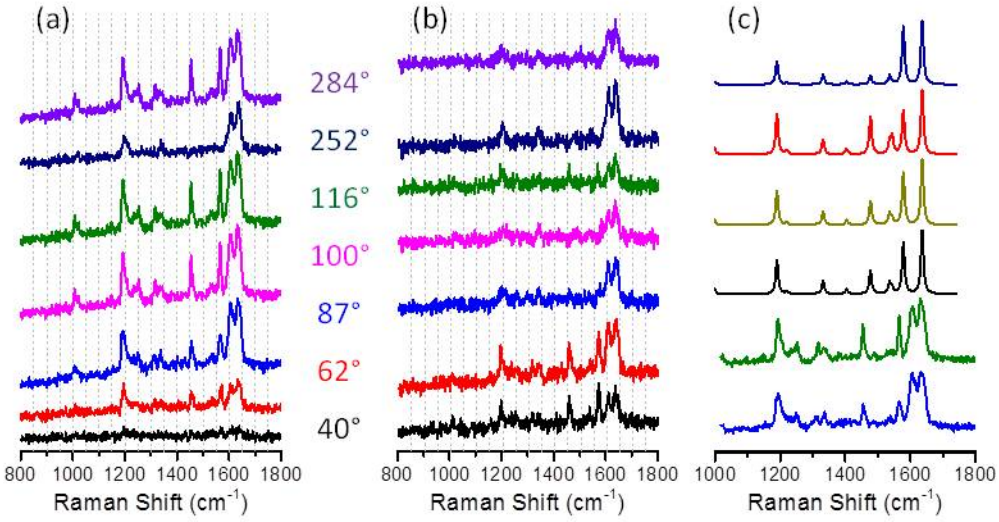

Figure 5.9: Parallel (a) and perpendicular (b) channel showing identical spectra on particle 3 (cuts from Fig 5). (c) Computed spectra at Euler angles {α, β, γ} = {36°, 7°, 18°} in blue, {18°, 82°, 0°} in red, {69°, 80°, 52°} in yellow and {67°, 81°, 36°} in black. The set shows intensity variation of ~1450 cm^{-1} and ~1580 cm^{-1} line as in experiment, while relative intensities of other modes stay fairly unaltered.

In Fig. 5.9a,b, we show the Raman spectra of the molecule recorded on particle 3. Although the spectra fluctuate, once again, the simultaneously recorded spectra are identical in the parallel and perpendicular channels. Despite the multipolar polarization maps of the molecular lines and nantenna seen in Fig. 5.5, the dipolar spectrum intermittently appears, as in the spectrum recorded at 252° in Fig. 5.9. Two new prominent lines, near 1450 cm^{-1} and 1580 cm^{-1}, can be seen to develop in time, and to fluctuate in synchrony. Closer inspection of their trajectories shows correlated meandering: sudden spectral shifts and line narrowing on the time scale of acquisition of 10 s/spectrum. The spectral shifts indicate strong perturbations that we do not address. Our focus is to understand the intensity patterns. The observed spectra can be

adequately reproduced, as illustrated in Fig. 5.9, assuming dipolar Raman driven by elliptically polarized local fields in orthogonal planes, $\hat{\varepsilon}_i$ = [1, 0.6i, 0] and $\hat{\varepsilon}_s$ = [0, 1, 0.6i]. This would arise from a magnetic field with equal Cartesian projections along the molecular $\hat{z}$ and $\hat{x}$ axes. Be it due to the displacement current of oscillating surface charge density across the junction gap, or real current due to the charge transfer plasmons, an azimuthal magnetic field $B\hat{\phi}$ arises along a loop that enclose the current. If we were to assume that the molecule is locked into position, then the fluctuation would suggest a slow evolution of the junction that leads to "arcing" near the molecule, which in turn generates the circulating local fields. Such events can be commonly identified. In fact, the captured episode and its reproduction is nearly identical to the "uneventful trajectory" tracked in our prior analysis of the closely related system on silver dumbbells.[17]

To underscore the role of junction asperities and photo-current, we show a SERS trajectory captured on a fourth dumbbell. The meandering SERS trajectory can be seen in the image plot. The fluctuating spectra are very similar to those seen on particle 3, and once again we see recurrences of the dipolar spectrum. Since the measurement spans 360° rotation of the incident field, the same relative angle between field and dumbbell is revisited after ~ 30 minutes of irradiation. The structureless band-spectrum appears at 96° and then again after 180° rotation, albeit with somewhat reduced intensity. Accepting this as the signature of Raman scattering driven by photo-current passing through the molecule, the sharp angle dependence would suggest "arcing" along a well defined protrusion. A single adatom in a ~ 1 nm junction is sufficient to close the gap to the tunneling regime of ~ 6-7 Å operative in STM junctions. Similar episodes are seen on multiple investigated dumbbells. We present this data to emphasize that structure on atomic scales play a defining role in determining fields and currents at the hot spot

of the nanojunction. These features, which evolve under irradiation, play a key role in coupling the molecular receiver to the far field.

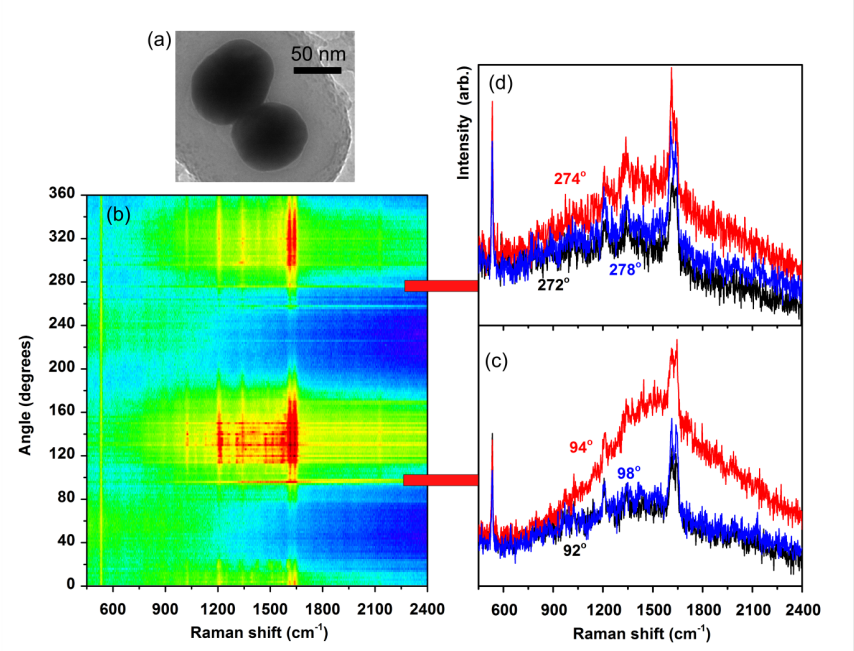

Figure 5.10: Polarization dependent SERS trajectory on a fourth dumbbell. (a) TEM image of the particle. (b) Parallel scattering channel as a function of angle showing the meandering of the molecular lines during the measurement and the repeated appearance of a band-spectrum as a function of excitation angle (positions shown with red lines). (c,d) Appearance and disappearance of "arcing" band-spectrum at sharply defined angles 94° and 274°.

5.5 Concluding remarks

The SERS background seen on individual gold nano-dumbbells can be readily assigned to electronic Raman scattering on its plasmons. This is most directly recognized by the polarization pattern of the scattering in the far field, where both the dipolar and quadrupolar plasmon of the dumbbell can be seen. We showed that the simultaneously recorded angular maps of parallel and perpendicular scattering allows retrieval of the polarizability matrix of the nantenna, and allows a detailed analysis of the nature of the induced polarization by the applied field. As a nonlinear process, Raman is more informative than linear extinction measurements. This is underscored, for example, by the identification of chiral plasmons and their handedness. Chiral plasmons are valuable meta-material elements for applications in light management,[70] including the generation of left-handed light.[71] While we do not have direct measurements, we suspect that atomic scale variations in the nano-junction control the sense of the polarization rotation on otherwise seemingly achiral and structurally very similar dumbbells (see Figs. 5,6). The polarization patterns of the plasmonic Raman was quantitatively reproduced by expanding the response to second order in spatial dispersion, $R^{(2D)}$, subject to the single scaling parameter, ζ_A, associated with the confinement of light on the nantenna. The inclusion of spatial dispersion is equivalent to nonlocal response, a consideration that is most clearly illustrated in the classical treatments of dichroism or helical response.[72] They can only be sustained on a dumbbell with broken inversion symmetry, and we show through electron microscopy that typical asymmetries of nanospheres are sufficient to drive these modes. The extracted value of the scaling parameter, $\zeta_A = 0.5 = 2\pi\lambda_A/\lambda_0$, establishes the effective wavelength of the polarization on the nantenna, $\lambda_A = \lambda_0/12 = 42\,nm$, at λ_0 = 532 nm for gold dumbbells made of nanospheres of 95 nm diameter. The effective wavelength of an antenna plays a key role in its characterization,[2]

therefore a direct method of its experimental determination is valuable. The extracted value is in line with theoretical determinations of on nano-rod dipolar antennas. [73]

The present analysis of the BPE molecular SERS on encapsulated gold dumbbells closely follows our prior treatment of dithio-linked bare silver dumbbells.[17] The conclusions made from the analysis of fluctuating spectra are nearly the same, including episodes extracted from trajectories that identify commonality in behavior. We ascribe the observed spectral fluctuations to variations in fields and field gradients experienced by the molecule, with histories determined by structural evolution of the nanojunction on atomic scales. Here, we show that the polarization patterns of molecular lines faithfully follow those of the nantenna, despite the absence of correlation between the interrogated fields and transitions. We observe fluctuating dipolar and multipolar vibrational Raman spectra of the molecule on a dumbbell that shows strictly dipolar response; and the same holds for dumbbells that show multipolar response. While perhaps this lack of correlation between far fields and static zone measurements is to be expected, the experiment illustrates the complexity of plasmonic nanojunctions. We used the $R^{(2D)}$ response framework to constrain the analysis of multipolar SERS, subject to the scaling parameter, ζ_J, which yields to alternative interpretations. The extracted values serve to quantify the enhancement of magnetic versus electric dipole transitions, and we find $\varsigma_J^2/\varsigma_0^2 \sim 2\times10^5$. This implies an overall enhancement of a magnetic transition by $E_F\varsigma_J^2/\varsigma_0^2 = 10^{13}$ if we assume a typical SERS enhancement factor of $E_F = 10^8$. The effect is due to the large field gradients experienced by a molecule in the near zone, which in turn can be associated with the effective confinement of light in the plasmonic junction. Thus, associating the gradient of the vector potential sampled by the molecule with an effective local wavevector, $k_l = |\nabla A|$, we can state with generality that $k_l\langle r\rangle \sim 1$ is implied when spectra fluctuate between dipolar and multipolar

Raman. If, instead, the measured multipolar enhancement factor is used to define an effective local wavelength, $\lambda_{e,J} = \frac{\lambda_0 \zeta_J}{\zeta_0} = \frac{\lambda_0 k_l}{k_0} \sim 1$ nm, we get the practical sense of extremely confined light.

In addition to enhanced electric fields, enhanced magnetic fields can be sustained on realistic nanojunctions. They originate from both displacement currents due to the modulation of surface charges, and real currents due to conductive nano-bridges and tunneling current driven by charge transfer plasmons. Molecules subjected to real current can be recognized by: a) dramatic increases in intensity due to oscillator strength borrowed from the plasmon, b) spectral broadening and coalescence of lines, which can be understood to arise from strong coupling to the metal electrons. Such charge transfer between molecule and metal can be regarded as the chemical contribution to SERS,[74,75] or tunneling current driven Raman.[76] The arcing spectra we showed are examples.

5.6 Appendix:

A) The simultaneously measured angular distributions of Raman scattering $|\langle\hat{\boldsymbol{\varepsilon}}_s \cdot \boldsymbol{\alpha} \cdot \hat{\boldsymbol{\varepsilon}}_i\rangle|^2$, along parallel $\hat{\boldsymbol{\varepsilon}}_s \cdot \hat{\boldsymbol{\varepsilon}}_i = 1$ and perpendicular $\hat{\boldsymbol{\varepsilon}}_s \cdot \hat{\boldsymbol{\varepsilon}}_i = 0$ channels, fully determine the polarizability matrix, $\boldsymbol{\alpha}$, of the scatterer. This can be recognized by first noting that 2D vector space is spanned by the orthogonal basis set of Pauli matrices, $\boldsymbol{\sigma_i}$:

$$\boldsymbol{\alpha} = \frac{1}{2}\sum_{i=0}^{3} S_i \boldsymbol{\sigma_i}$$

where

$$\sigma_0 = \begin{bmatrix} 1 & 0 \\ 0 & 1 \end{bmatrix}, \sigma_1 = \begin{bmatrix} 1 & 0 \\ 0 & -1 \end{bmatrix}, \sigma_2 = \begin{bmatrix} 0 & 1 \\ 1 & 0 \end{bmatrix}, \sigma_3 = \begin{bmatrix} 1 & -i \\ i & 1 \end{bmatrix}$$

and S_i are the parameters of the Stokes vector, familiar in the description of coherency that uniquely defines the polarization state of light. For incident field linearly polarized along ϑ, the scattered fields in the parallel and perpendicular channels are given as:

$$E_{\parallel}^{\sigma_i}(\vartheta) = [cos\vartheta \quad sin\vartheta]\boldsymbol{\sigma_i}\begin{bmatrix} cos\vartheta \\ sin\vartheta \end{bmatrix}$$

$$E_{\perp}^{\sigma_i}(\vartheta) = [sin\vartheta \quad cos\vartheta]\boldsymbol{\sigma_i}\begin{bmatrix} cos\vartheta \\ sin\vartheta \end{bmatrix}$$

The joint angular distributions $E^{\sigma_i} \equiv \langle E_{\parallel}^{\sigma_i}(\vartheta), E_{\perp}^{\sigma_i}(\vartheta)|$ and their associated field intensities $I^{\sigma_i} \equiv \langle [E_{\parallel}^{\sigma_i}(\vartheta)]^2, [E_{\perp}^{\sigma_i}(\vartheta)]^2|$ generate an orthogonal representation:

	$\boldsymbol{E^{\sigma_i}}$	$\boldsymbol{I^{\sigma_i}}$
σ_0	$\begin{bmatrix} 1 \\ 2sin\vartheta cos\vartheta \end{bmatrix}$	$\begin{bmatrix} 1 \\ 4sin^2\vartheta cos^2\vartheta \end{bmatrix}$
σ_1	$\begin{bmatrix} cos^2\vartheta - sin^2\vartheta \\ 0 \end{bmatrix}$	$\begin{bmatrix} (cos^2\vartheta - sin^2\vartheta)^2 \\ 0 \end{bmatrix}$
σ_2	$\begin{bmatrix} 2sin\vartheta cos\vartheta \\ 1 \end{bmatrix}$	$\begin{bmatrix} 4sin^2\vartheta cos^2\vartheta \\ 1 \end{bmatrix}$
σ_3	$\begin{bmatrix} 0 \\ cos^2\vartheta - sin^2\vartheta \end{bmatrix}$	$\begin{bmatrix} 0 \\ (cos^2\vartheta - sin^2\vartheta)^2 \end{bmatrix}$

To illustrate the use of the representation, consider a polarizability matrix given by the single element, α_{xx}, therefore $\boldsymbol{\alpha}=(\boldsymbol{\sigma}_0 + \boldsymbol{\sigma}_1)/2$. Then

$$E^{\alpha_{xx}} = (E^{\sigma_0} + E^{\sigma_1})/2 = \frac{1}{2}\begin{bmatrix} 1 + cos^2\vartheta - sin^2\vartheta \\ 2sin\vartheta cos\vartheta \end{bmatrix} = \begin{bmatrix} cos^2\vartheta \\ sin\vartheta cos\vartheta \end{bmatrix}$$

and the observable joint angular distribution is

$$I^{\alpha_{xx}} = \begin{bmatrix} cos^4\vartheta \\ sin^2\vartheta cos^2\vartheta \end{bmatrix}$$

In addition to unique decompositions that can be made by inspection of the joint angular distributions, since the Pauli spin matrices map on the Jones matrices, the decompositions acquire physical functional meaning.

The above applies for strictly local response, where the third order polarization is induced by applied electric fields, $P_i^{(3)} = \chi_{ijkl}^{(3)} E_j E_k E_l$. In first order nonlocal response, if only electric fields are explicitly noted, then $P_i^{(3)} = \Gamma_{ijkl} E_j E_k \delta_i E_m$ which leads to both magnetic and quadrupolar contributions. Explicit accounting of magnetic fields contracts the indices in the susceptibility, $P_i^{(3)} = \Gamma_{ijkl} E_j E_k H_l$ to the four waves, and allows a description of the response in Pauli matrices. The chiral response is then given more naturally:

$$\chi^{(3)} = \chi_{EE} \begin{bmatrix} \chi_{EE} & \chi_{EH} \\ \chi_{HE} & \chi_{HH} \end{bmatrix}$$

Since *E* and *H* are orthogonal, each action of the *H*-field can be accounted for by σ_1 rotation about the z-axis: $\sigma_i(EH) = \sigma_i\sigma_1$, while $\sigma_i(HH) = \sigma_1\sigma_i\sigma_1$. Taking $\varsigma = \mu_m/\mu_e$ as the ratio of electric and magnetic dipoles:

$$\chi^{(3)} = \sigma_i \begin{bmatrix} \sigma_i & \varsigma\sigma_i\sigma_1 \\ \varsigma\sigma_i\sigma_1 & \varsigma^2\sigma_1\sigma_i\sigma_1 \end{bmatrix} = \sigma_i^2 + 2\varsigma\sigma_i^2\sigma_1 + (\varsigma\sigma_i\sigma_1)^2$$

For strictly dipolar response, $\sigma_i = (\sigma_0 + \sigma_1)/2$, the joint polarization distribution, in what we refer to as second order in spatial dispersion, is easily obtained:

$$E^{(2D)}(\vartheta) = \left\{ \begin{bmatrix} cos^4\vartheta \\ sin^2\vartheta cos^2\vartheta \end{bmatrix} + 2\varsigma \begin{bmatrix} cos^3\vartheta sin\vartheta \\ cos\vartheta sin^3\vartheta \end{bmatrix} + \varsigma^2 \begin{bmatrix} sin^2\vartheta cos^2\vartheta \\ sin^4\vartheta \end{bmatrix} \right\}$$

which is the chiral response in expression 5.6 of the text. Clearly, the scattering in nonlocal response can be decomposed by the expanded table of the products, $I^{\sigma_i \sigma_j}$.

5.7 References:

(1) Novotny, L.; van Hulst, N. F. Antennas for Light. *Nat. Photonics* **2011**, *5*, 83–90.

(2) Bharadwaj, P.; Deutsch, B.; Novotny, L. Optical Antennas. *Adv. Opt. Photonics* **2009**, *1*, 438.

(3) Olmon, R. L.; Raschke, M. B. Antenna-Load Interactions at Optical Frequencies: Impedance Matching to Quantum Systems. *Nanotechnology* **2012**, *23*, 444001.

(4) Jeanmaire, D. L.; Duyne, R. P. Van. Surface Enhanced Raman Spectroelectrochemistry. *J. Electroanal. Chem.* **1977**, *84*, 1–20.

(5) *Surface-Enhanced Raman Scattering: Physics and Applications*; Kneipp, K.; Moskovits, M.; Kneipp, H., Eds.; Springer: Heidelberg, 2010; p. 482.

(6) Nie, S.; Emory, S. R. Probing Single Molecules and Single Nanoparticles by Surface-Enhanced Raman Scattering. *Science (80-.).* **1997**, *275*, 1102–1106.

(7) Kneipp, K.; Wang, Y.; Kneipp, H.; Perelman, L.; Itzkan, I.; Dasari, R.; Feld, M. Single Molecule Detection Using Surface-Enhanced Raman Scattering (SERS). *Phys. Rev. Lett.* **1997**, *78*, 1667–1670.

(8) Blackie, E. J.; Le Ru, E. C.; Etchegoin, P. G. Single-Molecule Surface-Enhanced Raman Spectroscopy of Nonresonant Molecules. *J. Am. Chem. Soc.* **2009**, *131*, 14466–14472.

(9) Haran, G. Single-Molecule Raman Spectroscopy: A Probe of Surface Dynamics and Plasmonic Fields. *Acc. Chem. Res.* **2010**, *43*, 1135–1143.

(10) Le Ru, E.; Etchegoin, P. G. Single-Molecule Surface-Enhanced Raman Spectroscopy. *Annu. Rev. Phys. Chem* **2012**, 1–23.

(11) Michaels, A. M.; Nirmal, M.; Brus, L. E. Surface Enhanced Raman Spectroscopy of Individual Rhodamine 6G Molecules on Large Ag Nanocrystals. *J. Am. Chem. Soc.* **1999**, *121*, 9932–9939.

(12) Camden, J. P.; Dieringer, J. a; Wang, Y.; Masiello, D. J.; Marks, L. D.; Schatz, G. C.; Van Duyne, R. P. Probing the Structure of Single-Molecule Surface-Enhanced Raman Scattering Hot Spots. *J. Am. Chem. Soc.* **2008**, *130*, 12616–12617.

(13) Dadosh, T.; Sperling, J.; Bryant, G. W.; Breslow, R.; Shegai, T.; Dyshel, M.; Haran, G.; Bar-Joseph, I. Plasmonic Control of the Shape of the Raman Spectrum of a Single Molecule in a Silver Nanoparticle Dimer. *ACS Nano* **2009**, *3*, 1988–1994.

(14) Camargo, P. H. C.; Rycenga, M.; Au, L.; Xia, Y. Isolating and Probing the Hot Spot Formed between Two Silver Nanocubes. *Angew Chemie Int. ed.* **2009**, *48*, 2180–2184.

(15) Whitmore, D.; El-khoury, P. Z.; Fabris, L.; Chu, P.; Bazan, G. C.; Potma, E. O.; Apkarian, V. A. High Sensitivity Surface-Enhanced Raman Scattering in Solution Using Engineered Silver Nanosphere Dimers. *J. Phys. Chem. C* **2011**, *115*, 15900–15907.

(16) Banik, M.; Nag, A.; El-Khoury, P. Z.; Perez, A. R.; Guarrotxena, N.; Bazan, G. C.; Apkarian, V. A. Surface-Enhanced Raman Scattering of a Single Nanodumbbell : *J. Phys. Chem. C* **2012**, *116*, 10415–10423.

(17) Banik, M.; El-Khoury, P. Z.; Nag, A.; Rodriguez-Perez, A.; Guarrottxena, N.; Bazan, G. C.; Apkarian, V. A. Surface-Enhanced Raman Trajectories on a Nano-Dumbbell: Transition from Field to Charge Transfer Plasmons as the Spheres Fuse. *ACS Nano* **2012**, *6*, 10343–10354.

(18) Kleinman, S. L.; Sharma, B.; Blaber, M. G.; Henry, A.-I.; Valley, N.; Freeman, R. G.; Natan, M. J.; Schatz, G. C.; Van Duyne, R. P. Structure Enhancement Factor Relationships in Single Gold Nanoantennas by Surface-Enhanced Raman Excitation Spectroscopy. *J. Am. Chem. Soc.* **2013**, *135*, 301–308.

(19) Xu, H.; Aizpurua, J.; Kall, M.; Apell, P. Electromagnetic Contributions to Single-Molecule Sensitivity in Surface-Enhanced Raman Scattering. *Phys. Rev. E* **2000**, *62*, 4318–4324.

(20) Blanco, L.; García-Vidal, F. Spontaneous Light Emission in Complex Nanostructures. *Phys. Rev. B* **2004**, *69*, 1–12.

(21) Nordlander, P.; Oubre, C.; Prodan, E.; Li, K.; Stockman, M. I. Plasmon Hybridization in Nanoparticle Dimers. *Nano Lett.* **2004**, *4*, 899–903.

(22) Litz, J. P.; Camden, J. P.; Masiello, D. J. Spatial, Spectral and Coherence Maping of Single-Molecule Sers Active Hot Spots via the Discrete-Dipole Approximation. *J. Phys. Chem. Lett.* **2011**, *2*, 1695–1700.

(23) Hallock, A.; Redmond, P. L.; Brus, L. E. Optical Forces between Metallic Particles. *Proc. Natl. Acad. Sci.* **2005**, *102*, 1280–1284.

(24) Kelly, K. L.; Coronado, E.; Zhao, L. L.; Schatz, G. C. The Optical Properties of Metal Nanoparticles: The Influence of Size, Shape, and Dielectric Environment. *J. Phys. Chem. B* **2003**, *107*, 668–677.

(25) Chu, P.; Mills, D. Laser-Induced Forces in Metallic Nanosystems: The Role of Plasmon Resonances. *Phys. Rev. Lett.* **2007**, *99*, 1–4.

(26) Chu, P.; Mills, D. Electromagnetic Response of Nanosphere Pairs: Collective Plasmon Resonances, Enhanced Fields, and Laser-Induced Forces. *Phys. Rev. B* **2008**, *77*, 1–10.

(27) Xu, H.; Kall, M. Surface-Plasmon-Enhanced Optical Forces in Silver Nanoaggregates. *Phys. Rev. Lett.* **2002**, *89*, 1–4.

(28) Hao, E.; Schatz, G. C. Electromagnetic Fields around Silver Nanoparticles and Dimers. *J. Chem. Phys.* **2004**, *120*, 357–366.

(29) Wustholz, K. L.; Henry, A.-I.; McMahon, J. M.; Freeman, R. G.; Valley, N.; Piotti, M. E.; Natan, M. J.; Schatz, G. C.; Van Duyne, R. P. Structure-Activity Relationships in Gold Nanoparticle Dimers and Trimers for Surface-Enhanced Raman Spectroscopy. *J. Am. Chem. Soc.* **2010**, *132*, 10903–10910.

(30) Song, P.; Nordlander, P.; Gao, S. Quantum Mechanical Study of the Coupling of Plasmon Excitations to Atomic-Scale Electron Transport. *J. Chem. Phys.* **2011**, *134*, 074701.

(31) Savage, K. J.; Hawkeye, M. M.; Esteban, R.; Borisov, A. G.; Aizpurua, J.; Baumberg, J. J. Revealing the Quantum Regime in Tunnelling Plasmonics. *Nature* **2012**, *491*, 574–577.

(32) Scholl, J. a; García-Etxarri, A.; Koh, A. L.; Dionne, J. a. Observation of Quantum Tunneling between Two Plasmonic Nanoparticles. *Nano Lett.* **2013**, *13*, 564–569.

(33) Marinica, D. C.; Kazansky, a K.; Nordlander, P.; Aizpurua, J.; Borisov, a G. Quantum Plasmonics: Nonlinear Effects in the Field Enhancement of a Plasmonic Nanoparticle Dimer. *Nano Lett.* **2012**, *12*, 1333–1339.

(34) Zhang, P.; Feist, J.; Rubio, A. Ab-Initio Nanoplasmonics: Atoms Matter. *arXiv:1403.8016 [physics.optics]* **2014**, 1–5.

(35) Ward, D. R.; Hüser, F.; Pauly, F.; Cuevas, J. C.; Natelson, D. Optical Rectification and Field Enhancement in a Plasmonic Nanogap. *Nat. Nanotechnol.* **2010**, *5*, 732–736.

(36) Ma, Z.; Vandenbosch, G. a. E. Optimal Solar Energy Harvesting Efficiency of Nano-Rectenna Systems. *Sol. Energy* **2013**, *88*, 163–174.

(37) Berland, B. Photovoltaic Technologies Beyond the Horizon : Optical Rectenna Solar Cell Final Report Photovoltaic Technologies Beyond the Horizon : Optical Rectenna Solar Cell Final Report. *Natl. Renew. Energy Lab., Golden, CO, NREL Rep. SR-520-33263, Final Rep.* **2003**.

(38) Marr, J. M.; Schultz, Z. D. Imaging Electric Fields in SERS and TERS Using the Vibrational Stark Effect. *J. Phys. Chem. Lett.* **2013**, *4*.

(39) El-Khoury, P. Z.; Hu, D.; Apkarian, V. A.; Hess, W. P. Raman Scattering at Plasmonic Junctions Shorted by Conductive Molecular Bridges. *Nano Lett.* **2013**, *13*, 1858–1861.

(40) Banik, M.; Apkarian, V. A.; Park, T.-H.; Galperin, M. Raman Staircase in Charge Transfer SERS at the Junction of Fusing Nanospheres. *J. Phys. Chem. Lett.* **2013**, *4*, 88–92.

(41) Galperin, M.; Tretiak, S. Linear Optical Response of Current-Carrying Molecular Junction: A Nonequilibrium Green's Function-Time-Dependent Density Functional Theory Approach. *J. Chem. Phys.* **2008**, *128*, 124705.

(42) Oren, M.; Galperin, M.; Nitzan, A. Raman Scattering from Molecular Conduction Junctions: Charge Transfer Mechanism. *Phys. Rev. B* **2012**, *85*, 115435.

(43) Stolz, A.; Berthelot, J.; Mennemanteuil, M.-M.; Colas des Francs, G.; Markey, L.; Meunier, V.; Bouhelier, A. Nonlinear Photon-Assisted Tunneling Transport in Optical Gap Antennas. *Nano Lett.* **2014**, *14*, 2330–2338.

(44) Ayars, E. J.; Hallen, H. D.; Jahncke, C. L. Electric Field Gradient Effects in Raman Spectroscopy. *Phys. Rev. Lett.* **2000**, *85*, 4180–4183.

(45) Zhang, Z.; Sun, M.; Ruan, P.; Zheng, H.; Xu, H. Electric Field Gradient Quadrupole Raman Modes Observed in Plasmon-Driven Catalytic Reactions Revealed by HV-TERS. *Nanoscale* **2013**, *5*, 4151–4155.

(46) Kneipp, H.; Kneipp, J.; Kneipp, K. Surface-Enhanced Raman Optical Activity on Adenine in Silver Colloidal Solution. *Anal. Chem.* **2006**, *78*, 1363–1366.

(47) Acevedo, R.; Lombardini, R.; Halas, N. J.; Johnson, B. R. Plasmonic Enhancement of Raman Optical Activity in Molecules near Metal Nanoshells. *J. Phys. Chem. A* **2009**, *113*, 13173–13183.

(48) Jensen, L. Surface-Enhanced Vibrational Raman Optical Activity: A Time-Dependent Density Functional Theory Approach. *J. Phys. Chem. A* **2009**, *113*, 4437–4444.

(49) Nafie, L. A. *Vibrational Optical Activity: Principles and Applications*; 2011.

(50) Chen, G.; Wang, Y.; Yang, M.; Xu, J.; Goh, S. J.; Pan, M.; Chen, H. Measuring Ensemble-Averaged Surface-Enhanced Raman Scattering in the Hotspots of Colloidal Nanoparticle Dimers and Trimers. *J. Am. Chem. Soc.* **2010**, *132*, 3644–3645.

(51) Frontiera, R. R.; Henry, A.-I.; Gruenke, N. L.; Van Duyne, R. P. Surface-Enhanced Femtosecond Stimulated Raman Spectroscopy. *J. Phys. Chem. Lett.* **2011**, *2*, 1199–1203.

(52) Yampolsky, S.; Fishman, D. a.; Dey, S.; Hulkko, E.; Banik, M.; Potma, E. O.; Apkarian, V. A. Seeing a Single Molecule Vibrate through Time-Resolved Coherent Anti-Stokes Raman Scattering. *Nat. Photonics* **2014**, 1–7.

(53) Link, S.; El-sayed, M. A. Shape and Size Dependence of Radiative , Non-Radiative and Photothermal Properties of Gold Nanocrystals. *Int. Rev. Phys. Chem.* **2000**, *19*, 409–453.

(54) Kreibig, U. Interface-Induced Dephasing of Mie Plasmon Polaritons. *Appl. Phys. B* **2008**, *93*, 79–89.

(55) Jiang, J.; Bosnick, K.; Maillard, M.; Brus, L. E. Single Molecule Raman Spectroscopy at the Junctions of Large Ag Nanocrystals. *J. Phys. Chem. B* **2003**, *107*, 9964–9972.

(56) Moore, A. a; Jacobson, M. L.; Belabas, N.; Rowlen, K. L.; Jonas, D. M. 2D Correlation Analysis of the Continuum in Single Molecule Surface Enhanced Raman Spectroscopy. *J. Am. Chem. Soc.* **2005**, *127*, 7292–7293.

(57) Galperin, M.; Nitzan, A. Raman Scattering from Biased Molecular Conduction Junctions: The Electronic Background and Its Temperature. *Phys Rev B* **2011**, *84*, 195325.

(58) Itoh, T.; Yoshida, K.; Biju, V.; Kikkawa, Y.; Ishikawa, M.; Ozaki, Y. Second Enhancement in Surface-Enhanced Resonance Raman Scattering Revealed by an Analysis of Anti-Stokes and Stokes Raman Spectra. *Phys. Rev. B* **2007**, *76*, 085405.

(59) Itoh, T.; Biju, V.; Ishikawa, M.; Kikkawa, Y.; Hashimoto, K.; Ikehata, A.; Ozaki, Y. Surface-Enhanced Resonance Raman Scattering and Background Light Emission Coupled with Plasmon of Single Ag Nanoaggregates. *J. Chem. Phys.* **2006**, *124*, 134708.

(60) Otto, A.; Akemann, W.; Pucci, A. Normal Bands in Surface-Enhanced Raman Scattering (SERS) and Their Relation to the Electron-Hole Pair Excitation Background in SERS. *Isr. J. Chem.* **2006**, *46*, 307–315.

(61) Lombardi, J. R.; Birke, R. L. Excitation Profiles and the Continuum in SERS: Identification of Fano Line Shapes. *J. Phys. Chem. C* **2010**, *114*, 7812–7815.

(62) Chulhai, D. V.; Jensen, L. Determining Molecular Orientation With Surface-Enhanced Raman Scattering Using Inhomogenous Electric Fields. *J. Phys. Chem. C* **2013**, *117*, 130911133503005.

(63) El-Khoury, P. Z.; Hess, W. P. Vibronic Raman Scattering at the Quantum Limit of Plasmons. *Nano Lett.* **2014**, *14*, 4114–4118.

(64) Mukamel, S. *Principles of Nonlinear Optical Spectroscopy*; Oxford University Press, 1995; p. 268.

(65) Lassiter, J. B.; Aizpurua, J.; Hernandez, L. I.; Brandl, D. W.; Romero, I.; Lal, S.; Hafner, J. H.; Nordlander, P.; Halas, N. J. Close Encounters between Two Nanoshells. *Nano Lett.* **2008**, *8*, 1212–1218.

(66) Esteban, R.; Borisov, A. G.; Nordlander, P.; Aizpurua, J. Bridging Quantum and Classical Plasmonics with a Quantum-Corrected Model. *Nat. Commun.* **2012**, *3*, 1–9.

(67) Singh, R.; Plum, E.; Zhang, W.; Zheludev, N. I. Highly Tunable Optical Activity in Planar Achiral Terahertz Metamaterials. *Opt. Express* **2010**, *18*, 13425–13430.

(68) Frisch, M. J. et. al. *GAUSSIAN 09,Revision A.01*; Gaussian Inc.: Wallingford, CT, 2009.

(69) Yang, W.; Hulteen, J.; Schatz, G. C.; Duyne, R. P. Van. A Surface-Enhanced Hyper-Raman and Surface-Enhanced Raman Scattering Study of Trans-1 , 2-Bis (4-Pyridyl) Ethylene Adsorbed onto Silver Film over Nanosphere Electrodes. Vibrational Assignments: Experiment and Theory. *J. Chem. Phys.* **1996**, *104*, 4313–4323.

(70) Plum, E.; Fedotov, V. a; Zheludev, N. I. Extrinsic Electromagnetic Chirality in Metamaterials. *J. Opt. A Pure Appl Opt.* **2009**, *11*, 074009.

(71) Pendry, J. B. A Chiral Route to Negative Refraction. *Science* **2004**, *306*, 1353–1355.

(72) Kuhn, H. A Quantum-Mechanical Theory of Light Absorption of Organic Dyes and Similar Compounds. *J. Chem. Phys.* **1949**, *17*, 1198.

(73) Novotny, L. Effective Wavelength Scaling for Optical Antennas. *Phys. Rev. Lett.* **2007**, *98*.

(74) Lombardi, J. R.; Birke, R. L. Time-Dependent Picture of the Charge-Transfer Contributions to Surface Enhanced Raman Spectroscopy. *J. Chem. Phys.* **2007**, *126*, 244709.

(75) Morton, S. M.; Jensen, L. Understanding the Molecule-Surface Chemical Coupling in SERS. *J. Am. Chem. Soc.* **2009**, *131*, 4090–4098.

(76) Lee, J.; Perdue, S. M.; Rodriguez Perez, A.; Apkarian, V. A. Vibronic Motion with Joint Angstrom-Femtosecond Resolution Observed through Fano Progressions Recorded within One Molecule. *ACS Nano* **2014**, *8*, 54–63.